**“FEDERICO II” UNIVERSITY OF NAPLES**


Ph.D. in Chemical Sciences - XXVII Cycle

# ARTIFICIAL HEME-ENZYMES FOR CATALYTIC AND DIAGNOSTIC APPLICATIONS

Ph.D. candidate: Corinne Cerrone

**ADVISORS:** Prof. Angela Lombardi
Prof. Vincenzo Pavone

**EXAMINER:** Prof. Marco D’Ischia

**COORDINATOR:** Prof. Luigi Paduano

# Table of contents

# Table of contents

# Table of contents

# Abstract

Metals are commonly found as natural constituents of proteins. Nature has selected particular metals over an evolutionary period of 2–3 billion years to form metalloproteins, which perform a wide range of fundamental biological functions.

Metalloproteins consists of protein scaffolds and prosthetic groups, which contain one or more metal ions linked to the polypeptide chain by different types of interaction, either covalent or non-covalent.

A mutual relation between metal cofactors and polypeptide chains is established, since (*i*) metal ions can impart particular three-dimensional folding to the protein, thus influencing its function/s, and (*ii*) the protein matrix is able to modulate the chemical reactivity of metal ions, thus selecting one reaction as the only or predominant one. Understanding how Nature finely tunes the properties of metalloproteins, imparting them such different chemistries, is of crucial interest both in the fields of basic and applied sciences.

In this respect, this Ph.D. project was focused on the development of new artificial heme-protein mimetics, belonging to the Mimochrome family. Mimochromes[1–8] are heme-peptide models, made up by two peptide chains, covalently linked to the deuteroporphyrin IX. Their global folding can be viewed as a sandwich, in which the peptide chains are in α-helical conformation and cover both planes of the heme, resulting in a helix-heme-helix sandwich.

# Abstract

Through an iterative process of design, synthesis, characterization and re-design, a *penta*-coordinated model was developed, $Fe^{III}$-Mimochrome VI,[7] which exhibits peroxidase-like activity.

In a next stage of design, a generation of Mimochrome VI analogues was developed, by individually replacing Glu2 and Arg10 on both peptide chains with a Leu residue.[8] The four new analogues were screened for their peroxidase-like activity. The detailed structural and functional analysis of the best analogue, $Fe^{III}$-Glu2Leu(*TD*)-MC6, indicates that an arginine residue in proximity to the heme-distal site, now free from the ion pair interaction, could assist the catalysis by favouring the formation of the "Compound I", similarly to the conserved distal arginine (Arg38) in Horseradish Peroxidase (HRP).[9–11]

The main drawback of Mimochrome VI and its analogues relies in the lack of three-dimensional structures. The analysis of the NMR spectrum of the diamagnetic $Co^{III}$-Mimochrome VI complex revealed the presence of multiple species in solution.

In order to improve the structural properties and the catalytic performance of $Fe^{III}$-Mimochrome VI and its analogues, a re-design was performed.

Starting from $Fe^{III}$-Glu2Leu(*TD*)-MC6, whose model is lacking of an *inter*-chain ion pair interaction with respect to Mimochrome VI model, some structural constrains were inserted. Therefore, Aib residues were introduced at 3 and 7 positions of the decapeptide chain, obtaining a molecule, named Mimochrome VI*a*.

In the next stage of design, a systematic evaluation of the linker length between the porphyrin and the decapeptide chain was carried out. In particular, to further stabilize the sandwich structure, the linker length was progressively decreased. Therefore, Lys at position 9 on the decapeptide chain was substituted with Orn and with Dab, whose side chains contain, respectively, one and two methylenic group less than lysine side chain. In this way, two new analogues were obtained, named, respectively, Lys9Orn(*D*)-Mimochrome VI*a* and Lys9Dab(*D*)-Mimochrome VI*a*.

The Aib introduction allowed to separate two regioisomers for each compound, due to the coupling of the decapeptide to the propionic group at 2 position and of the tetradecapeptide at 18 position of the deuteroporphyrin, and vice versa. These two regioisomers, named isomer 1 and 2, were isolated and the metal was individually inserted into these two species.

The new developed enzymes were screened for their peroxidase-like activity. Thus, the oxidation of the reducing substrate ABTS (2,2'-azino-bis(3-ethylbenzthiazoline-6-sulphonic acid), by activating $H_2O_2$, was explored. The functional screening highlighted that:

- introducing Aib residues increases the stability toward bleaching, as shown by the higher turnover number;
- decreasing the decapeptide-porphyrin linker length increases the catalytic activity.

$Fe^{III}$-Lys9Dab(*D*)-Mimochrome VI*a* isomer 1 and 2 have been selected as the best enzymes, in terms of catalytic

activities and turnover number. While being more than tenfold smaller in terms of molecular weight, $Fe^{III}$-Lys9Dab(*D*)-Mimochrome VI*a* isomer 1 and 2 display improved enzyme-like properties, that in turn approach HRP.

UV-Vis, CD, EPR and Mössbauer spectroscopies were used in combination to gain insight into the molecular basis of the catalytic improvement, correlating the primary, secondary and tertiary structures of the new mini-enzymes with the spin state of the metal ion and the nature of the axial ligands. It was demonstrated that the iron(III) coordination environment is similar to that of HRP, the natural parent enzyme, confirming the correctness of the design.

The NMR spectrum of the cobalt complex of Lys9Dab(*D*)-Mimochrome VI*a* isomer 2 displays a unique species, in contrast with the NMR spectrum the prototype, $Co^{III}$-Mimochrome VI, which displays a more complex spectrum indicative of the presence of multiple species in solution. This result highlights that the improvement in the catalytic properties is accompanied by an improvement in the structural properties. The complete structural determination by NMR of $Co^{III}$-Lys9Dab(*D*)-Mimochrome VI*a* isomer 2 is in progress, in order to obtain information for useful structure-function relationship studies.

## References


(1) Nastri, F.; Lombardi, A.; Morelli, G.; Maglio, O.; D'Auria, G.; Pedone, C.; Pavone, V. *Chem. - Eur. J.* **1997**, *3* (3), 340–349.

(2) D'Auria, G.; Maglio, O.; Nastri, F.; Lombardi, A.; Mazzeo, M.; Morelli, G.; Paolillo, L.; Pedone, C.; Pavone, V. *Chem. - Eur. J.* **1997**, *3* (3), 350–362.

(3) Lombardi, A.; Nastri, F.; Pavone, V. *Chem. Rev.* **2001**, *101* (10), 3165–3189.

(4) Geremia, S.; Di Costanzo, L.; Randaccio, L.; Lombardi, A.; Pavone, V.; Campagnolo, M. *Acta Cryst* **2002**, *58*, C277.

(5) Costanzo, L.; Geremia, S.; Randaccio, L.; Nastri, F.; Maglio, O.; Lombardi, A.; Pavone, V. *JBIC J. Biol. Inorg. Chem.* **2004**, *9* (8), 1017–1027.

(6) Lombardi, A.; Nastri, F.; Marasco, D.; Maglio, O.; De Sanctis, G.; Sinibaldi, F.; Santucci, R.; Coletta, M.; Pavone, V. *Chem. - Eur. J.* **2003**, *9* (22), 5643–5654.

(7) Nastri, F.; Lista, L.; Ringhieri, P.; Vitale, R.; Faiella, M.; Andreozzi, C.; Travascio, P.; Maglio, O.; Lombardi, A.; Pavone, V. *Chem. - Eur. J.* **2011**, *17* (16), 4444–4453.

(8) Vitale, R.; Lista, L.; Cerrone, C.; Caserta, G.; Chino, M.; Maglio, O.; Nastri, F.; Pavone, V.; Lombardi, A. *Org Biomol Chem* **2015**. DOI:10.1039/c5ob00257e

(9) Rodriguez-Lopez, J. N.; Smith, A. T.; Thorneley, R. N. *J. Biol. Chem.* **1996**, *271* (8), 4023–4030.

(10) Azevedo, A. M.; Martins, V. C.; Prazeres, D. M. F.; Vojinović, V.; Cabral, J. M. S.; Fonseca, L. P. In *Biotechnology Annual Review*; Elsevier, 2003; Vol. 9, pp 199–247.

(11) Savenkova, M. I.; Kuo, J. M.; Ortiz de Montellano, P. R. *Biochemistry (Mosc.)* **1998**, *37* (30), 10828–10836.

# Chapter I
# Introduction

## 1.1 Metalloproteins in nature

Metals are commonly found as natural constituents of proteins. It has been estimated that over 50% of all proteins will turn out to be metalloproteins.[1] Nature has selected particular metals over an evolutionary period of 2–3 billion years on the basis of their unique physicochemical properties and bioavailability. In proteins, metals perform a wide range of fundamental biological functions, spanning from structure stabilization to catalysis, respiration, metabolism, nitrogen fixation, signal transduction, protection against toxic and mutagenic agents and photosynthesis.[2]

Metalloproteins are proteins that contain a metal ion cofactor;[3] among metalloproteins, those that perform a catalytic function are called metalloenzymes. Many metalloproteins contain transition metals. They possess energetically accessible *d* orbitals, which number, shape, and symmetry properties contribute to the rich variety of spectroscopic, magnetic, and catalytic properties exhibited by transition metal complexes. Transition metal ions may form with ligands different types of bonds, from highly covalent to highly electrostatic.

In general, ligands are atoms or groups of atoms bonded to the metal ion. They are electron pair donors (Lewis base) and are classified as monodentate (or polydentate) if one (or more) electron pair is donated to the metal ion. The ligands in metalloproteins are often derived by the polypeptide chain, and are therefore named

endogenous ligands. Most metal-binding sites include only a small number of coordinating amino acids, in a specific spatial arrangement. The most commonly found coordinating amino acid are histidine (His), cysteine (Cys), aspartic (Asp), and glutamic acid (Glu). On the contrary, tyrosine (Tyr), methionine (Met), serine (Ser), lysine (Lys), glutamine (Gln), asparagine (Asn), threonine (Thr), and glycine (Gly) less commonly coordinate the metal ion. With the exception of glycine, which coordinates a metal ion through the backbone carbonyl oxygen, the other amino acids participate in coordination almost exclusively through their side chains containing sulphur, oxygen or nitrogen as donor atoms.

Metal ion preferences for a certain amino acid side chain follow the general rules of coordination chemistry and often can be interpreted using the theory of hard and soft acids and bases (HSAB theory). Furthermore, metal ion can also be coordinated by exogenous cofactor groups (ligands not derived from the polypeptide chain); they comprise small inorganic entities, such as oxide, hydroxide, water, as well as organic macrocyclic ligands, such as porphyrins, corrins, and chlorins.[4]

Basically, a protein-bound metal site consists of one or more metal ions, all protein side chain and exogenous bridging and terminal ligands, that together define the first coordination sphere of each metal ion. Such sites, named prosthetic groups, can be classified into five basic types depending on their function:

(i) *structural* - configuration (in part) of protein tertiary and/or quaternary structure;
(ii) *storage* - uptake, binding, and release of metals in soluble form;
(iii) *electron transfer* - uptake, release, and storage of electrons;
(iv) *dioxygen binding* - metal-$O_2$ coordination and decoordination;
(v) *catalytic* - substrate binding, activation, and turnover.

The coordination is often conceived in terms of concentric spheres: the inner sphere containing those atoms interacting with the metal ion, the second sphere containing those atoms interacting with the inner sphere ligand atoms.[2] The number of atoms in these spheres depends on the size of the metal ion and the sizes of the ligand atoms. There is a large distribution of coordination numbers and geometries among the metal ions; however, the most frequent coordination numbers are four and six.

Coordination and geometry are strictly related to the metalloprotein function. For example, the charge distribution in the active site of an enzyme is designed to stabilize the transition state of the catalyzed reaction relative to that of the substrate. In enzyme-catalyzed reactions it is essential that the reactants be brought together with the correct spatial orientation, otherwise the chance of the reaction taking place is diminished and the reaction rate will be too low. The electrostatic environment in the active site is a major factor that serves to guide the substrate to the binding site in the correct orientation.

Metal ions can assist in this process, often binding groups in a stereochemically rigid manner, thereby helping to control the action of the enzyme. Thus, an enzyme will bind its substrate in such a manner that immobilization and alignment, ready formation of the transition state of the reaction to be catalyzed, and then easy release of the product will result; metal ions often help in accomplishing this process.[5]

## 1.1.1 Heme-proteins

### 1.1.1*a Heme structure*

Heme-proteins are a class of extremely important macromolecules, ubiquitous in biological systems, characterized by a common prosthetic group: the "heme". The heme chemically refers to iron ion, usually in the +2 or +3 oxidation states, enclosed in the center of the porphyrin, a large heterocyclic organic ring, in which four pyrrolic groups are linked together by methine bridges (Figure 1).

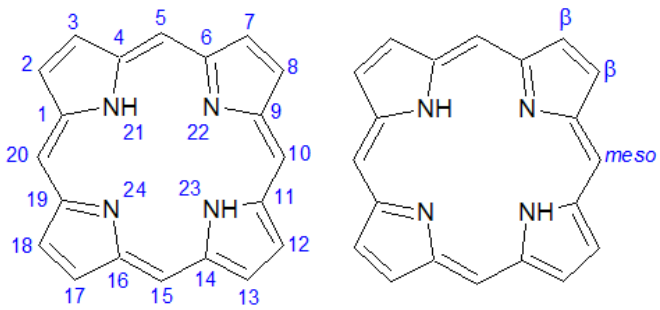


**Figure 1** Chemical structure and numbering scheme, according to IUPAC nomenclature of the porphyrin macrocycle. The 2, 3, 7, 8, 12, 13,

17 and 18 positions have commonly been referred to as *beta* positions, whereas those at 5, 10, 15 and 20 are referred to as *meso* positions.

Hemoproteins can perform a wide variety of different functions, spanning from electron transfer,[6,7] to catalysis,[6] dioxygen transport and storage,[6] ligand sensing,[8] steroid biosynthesis,[9] aerobic respiration,[10] photo-synthesis,[11] gene expression regulation[12] and even programmed cell death.[13]

The tetrapyrrole macrocycle is the chromophore in each type of natural heme-protein; its peripheral β-pyrrolic substituents define the type of heme, as shown in Figure 2.

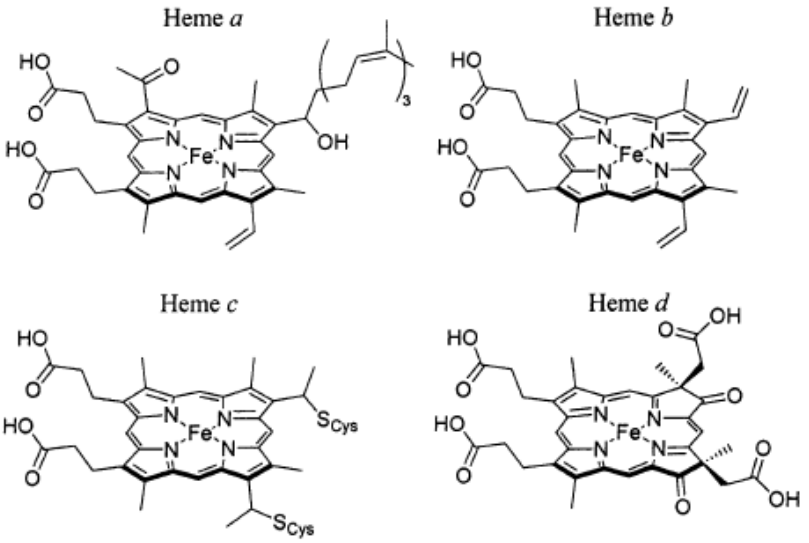


**Figure 2** Chemical structures of commonly occurring natural hemes *a*, *b*, *c* and *d*. Reproduced from reference 14.

The most common heme tetrapyrrole macrocycle is iron(II) protoporphyrin IX, known as heme *b* or "protoheme". The term "heme" specifically refers to the ferrous complex of protoporphyrin IX. Its structure has

methyl groups at positions 3, 7, 12 and 17, vinyl groups at positions 8 and 13, and propionates at positions 2 and 18 on the macrocycle. It is found in *b*-type cytochromes, globins, cytochromes P-450 and hemesensor proteins.
Generally, protein scaffolds bind hemes *via* the combination of the axial coordination positions available on the iron, hydrophobic interactions with the heme macrocycle, and polar interactions with the propionic acids.[14]

Heme *c* is structurally similar to heme *b* except that thioether bonds are formed between cysteine residues and the heme vinyl groups, thus covalently linking the heme macrocycle to the protein scaffold. Cytochromes *c* and cytochrome *f*, in which the heme *c* is found, typically contain a CXXCH sequence motif, in which the two cysteine residues link to the porphyrin macrocycle and the histidine binds to the encapsulated iron. The presence of a covalently linked heme designates it as a *c*-type.[14,15]

Heme *a* is biosynthesized from heme *b* by conversion of the vinyl group at position 8 into a hydroxyethylfarnesyl group, followed by subsequent oxidation of the methyl at position 3 to a formyl group. Therefore, heme *a* is both more hydrophobic and more electron-withdrawing respect to its precursor. Heme *a* is found only in terminal oxidases, such as mammalian cytochrome *c* oxidase.[14,16]

Other less common heme architectures include heme *d*,[17] heme P-460,[18] siroheme,[19] and chlorocruoroheme.[20]

### 1.1.1*b Protein matrix in heme-proteins*

The protein matrix plays a crucial role in determining the reactivity of the heme. In fact, there is a plethora of different functions performed by proteins containing the common prosthetic heme group. The protein composition and structural organization of the peptide fine-tune the environment of the heme cofactor, selecting one reaction as the only or predominant one.

The amino acid composition and the structural organization of the peptide chain dictate the properties of the primary (metal coordination geometry, number, type and donor properties of the axial ligands) and secondary (local dielectric constant, hydrophobicity, hydrogen bonding interactions near the active site) coordination shells. Moreover, the protein directs long-range interactions. All these factors modulate heme-protein features, such as redox potentials, electronic structure, spin states, and catalytic properties.[21]

Recently, the characteristics of the heme binding sites have been investigated in detail through bioinformatics.[22] Different amino acids are able to serve as axial or proximal ligands to heme. In a data set of nonhomologous heme-proteins, histidine predominates as an axial ligand (61 occurrences in the data set), especially in multiheme proteins. Other residues with side chains acting as axial ligands are methionine, cysteine, and tyrosine (8, 6, and 3 occurrences in the data set, respectively).[22] In two cases a change in axial ligand is observed on reduction: in CO-sensing protein the axial

ligand Cys75 is replaced by His77 in the reduced state,[23] while in cytochrome cd1 nitrite reductase one of the axial ligands (a tyrosine residue) exits from the coordination sphere on reduction, leaving a vacant site.[24]

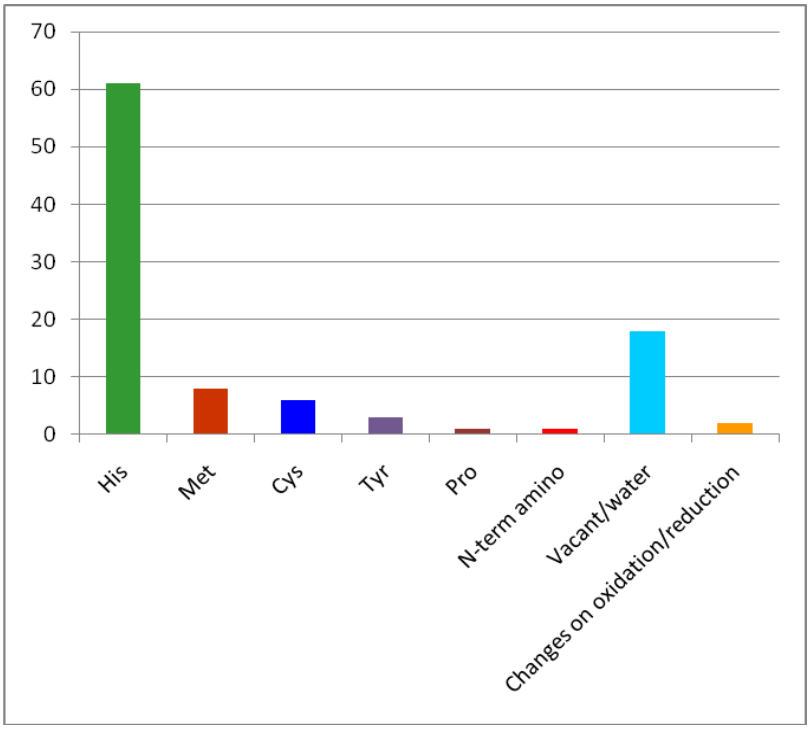


**Figure 3** Occurrence of axial ligands to the heme iron ion in a data set of nonhomologous heme-proteins. Data from reference 22.

The most frequently found coordination number is five; therefore, the most common coordination motif is five-coordinate *mono*-histidine, as found for globins and peroxidases, in which the protein matrix provides only one axial ligand, leaving the sixth coordination position empty to accommodate exogenous molecules. The second most common coordination motif (one-third as often as *mono*-

histidine) is six-coordinate *bis*-histidine, found in electron carriers proteins.

As shown in Figure 3, rather frequently methionine and cysteine act as axial ligands to the heme. In fact, typical ligation motif for six-coordinate heme-proteins are histidine and methionine (cytochrome c)[25] or *bis*-methionine (bacterioferritin),[26] whereas cysteine ligation is mainly observed in five-coordinate heme-proteins, such as cytochrome P-450.[27] Beyond methionine and cysteine, few other amino acid ligands are found in six-coordinated heme-proteins in combination with histidine (Tyr in cytochrome cd1 nitrite reductase).[24] In very few structures, some residues coordinate the heme iron through their neutral N-terminal amino group, such as a tyrosine in cytochrome f[15] and a proline in CO-sensing protein.[23]

Li *et al*. pointed out that heme binding pockets are enriched in aromatic and non-polar amino acids.[28] Through bioinformatic tools, they analyzed the occurrence of amino acid residues in a non-redundant data set of 125 heme-proteins.

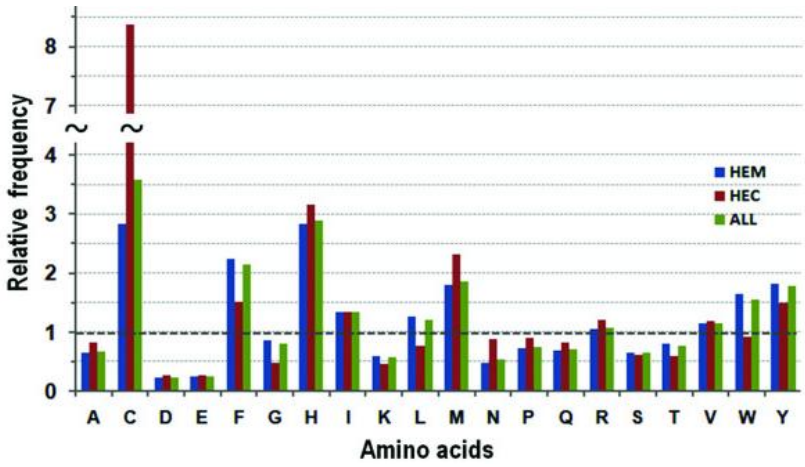


**Figure 4** Relative frequency of the residues in heme *b* (HEM), heme *c* (HEC), and heme *b* and *c* (ALL). Reproduced from reference 28.

The top five residues with highest relative frequencies are cysteine (C), histidine (H), phenylalanine (F), methionine (M), and tyrosine (Y). Four of the top five (C, H, M, and Y) are able to bind iron ion as axial ligands; removing axial ligands from the dataset, the occurrence of histidine decreases to the background level, proving that the occurrence of histidine is mainly due to its role as heme ligand. The other four residues, on the other hand, have almost the same relative frequencies with or without ligand residues (Figure 5).

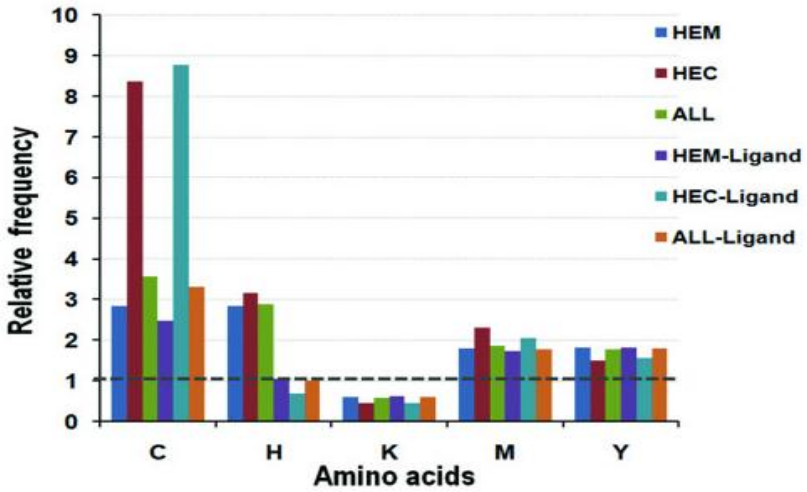


**Figure 5** Relative frequency of the 5 residues with or without them as axial heme ligands. Reproduced from reference 28.

In heme *c* proteins, the occurrence of cysteines is extremely high, due to the large presence of the classic CXXCH binding motif, as mentioned above.[29]

The aromatic residues (F, Y, W) play important roles in protein-heme interactions through stacking interactions with the porphyrin. Aliphatic residues (L, I, V) are slightly increased over the background frequencies: they make hydrophobic interactions with the heme macrocycle. The residues with the fewest occurrences (D, E, K), are charged residues, suggesting the heme binding pocket is mainly a hydrophobic environment.

Moving to the analysis of the heme-protein secondary structures, it has been observed the clear dominance of α-helical structures (77%), although heme-proteins mainly composed of β-sheets or mixed α/β structures are not uncommon (13% and 10%, respectively). This analysis has been performed using the

CATH database, which hierarchically categorizes protein structure by Class, Architecture, Topology and Homologous superfamily.[14]

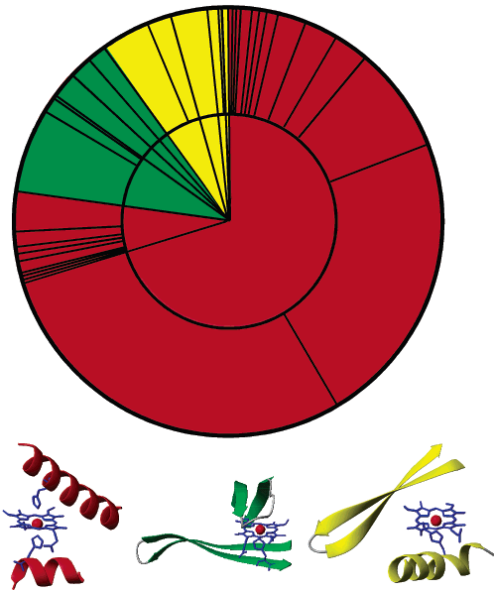

**Figure 6** A CATH wheel representation of natural heme-protein secondary structures: α-helical in red, $\beta$-sheet in green, mixed $\alpha/\beta$ in yellow. At the bottom, an example for each type: myoglobin in red, nitrophorin in green, and FixL in yellow. Reproduced from reference 14.

## 1.1.2 Peroxidases

Peroxidases are a large family of ubiquitous enzymes which catalyze the oxidation of a large array of organic and inorganic substrates, such as phenols, aromatic amine, thioanisoles and iodide, using hydrogen peroxide ($H_2O_2$) as electron acceptor.

Although they are among the first enzymes to have been discovered, with references dating back to 1845, when Schönbein observed the oxidation of guaiacol in presence of hydrogen peroxide by certain plant tissues, peroxidases continue to be widely studied, proving their prominent position in chemistry, biotechnology and associated research areas (enzymology, biochemistry, medicine, genetics).

Peroxidases are widely distributed among bacteria, fungi, plants, and animals; on the basis of their amino acid sequence similarities as well as functional and structural properties, peroxidases have been divided into three different superfamilies: plant peroxidases, animal peroxidases and catalases.

The plant superfamily consists of peroxidases of prokaryotes, fungi, and plants. They can be divided into three major classes: class I contains intracellular peroxidases of bacteria, archaeans, mitochondrial cytochrome c peroxidases, and ascorbate peroxidases; classes II and III include, respectively, the secretory fungal peroxidases and the secretory plant peroxidases.[30] This classification was based originally on comparisons of amino acid sequence, but it is well-supported by more recent three-dimensional structural data obtained for enzymes from each of the classes.

While plant peroxidases are monomeric proteins with a non-covalently bound heme, animal peroxidases are usually dimeric with a covalently attached prosthetic group.

The remaining peroxidases are catalases, which are heme tetrameric enzymes that catalyse the dismutation of $H_2O_2$.

All the peroxidases contain ferriprotoporphyrin IX as a prosthetic group, with the exception of myeloperoxidase,[31] which contains a chlorine. The iron ion, in the resting state of the enzyme, is invariantly *penta*-coordinated: the equatorial positions are occupied by the four pyrrole nitrogens of the heme, whereas in the axial position there is a nitrogen of an histidine (the so-called proximal histidine), except for chloroperoxidase which contains a thiolate ligand.[32] The sixth coordination position is free, thus determining a high spin S=5/2 state for the iron ion.

### 1.1.2*a Horseradish Peroxidase*

The Horseradish Peroxidase (HRP) is the most widely studied of all peroxidases. As all the peroxidases, HRP occurs as a large family of different molecular forms of the same enzyme, named isoenzymes, which catalyse the same reaction but have distinct physical, chemical and kinetic properties, arising from small differences in their amino acid sequence.

Although the term horseradish peroxidase is used somewhat generically, the root of the plant (*Armoracia rusticana*) contains a number of different peroxidase isoenzymes among which the C isoenzyme (HRP C) is the most abundant. This isoenzyme has been the subject of

much of the published work on horseradish peroxidase, which comprises many thousands of papers in literature.

HRP C comprises a single polypeptide chain of 308 amino acid residues,[33] with the N-terminal blocked by pyroglutamate and an heterogeneous C-terminus, with some molecules lacking the terminal residue (Ser308). Nine potential N-glycosylation sites can be recognised in the primary sequence from the motif Asn-X-Ser/Thr and of these, eight are occupied.

The total carbohydrate content of HRP C depends on the source of the enzyme; generally values between 18 and 22% are typical. The carbohydrate profile is heterogeneous and it is mainly constituted by branched *hepta*-saccharides, many minor glycans, N-acetylglucosamines (two of them invariably conserved at the termini) and several mannose residues.[34] If the carbohydrate moiety constitutes 20%, then the total molecular weight is around 42 kDa (this calculation does not account for bound water and counter ions).

HRP C contains two different types of metal centre, iron(III) protoporphyrin IX and two calcium atoms; both are essential for the structural and functional integrity of the enzyme.

The heme group is attached to the enzyme by a coordinate bond with the $N_\varepsilon$ of His170 (the proximal histidine). The second axial coordination position, on the distal side of the heme plane, is unoccupied in the resting state of the enzyme, but available to hydrogen peroxide binding during the enzyme turnover. Several other small molecules, such

as carbon monoxide, cyanide, fluoride and azide, are able to bind to the heme iron atom at this distal site.
The two calcium ions are located at the heme distal and proximal positions and they are both *hepta*-coordinated, with oxygen-donor ligands provided by a combination of amino acids side chains (Asp carboxylates, Ser and Thr hydroxyl groups), backbone carbonyls and a structural water molecule.[35]

HRP polypeptide chain folds into 13 α-helices and three β-sheets.[36] The proper protein conformation is stabilized by four disulfide bonds (Cys11–Cys91, Cys44–Cys49, Cys97–Cys301, and Cys177–Cys209). The protein consists of two domains, distal and proximal, between which the heme group is located.

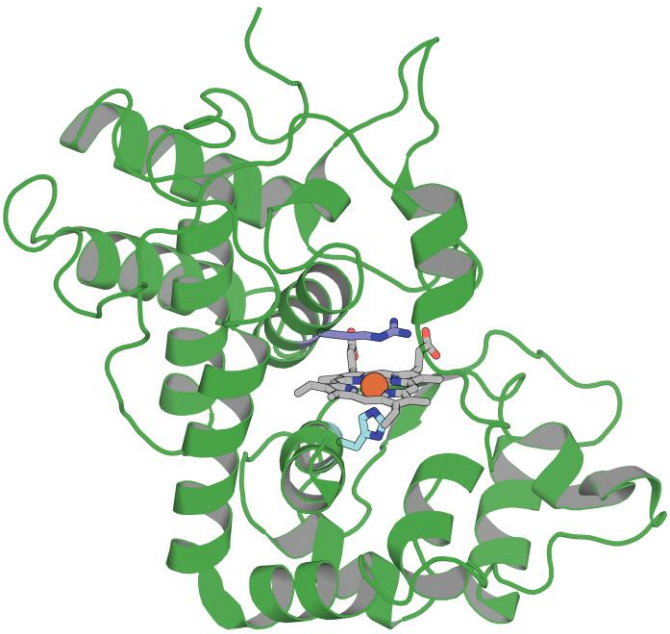

**Figure 7** Three-dimensional representation of the X-ray crystal structure of horseradish peroxidase isoenzyme C (PDB entry ID: 1H57).

Most reactions catalysed by HRP C and other horseradish peroxidase isoenzymes can be expressed by the following equation:

$$H_2O_2 + 2AH \xrightarrow{\text{HRP C}} 2H_2O + 2A^{\cdot}$$

in which AH and $A^{\cdot}$ represent a reducing substrate (such as aromatic phenols, phenolic acids, indoles, amines, sulfonates) and its radical product, respectively.

The catalysis occurs as a three-step cyclic process, in which the enzyme is first oxidized by $H_2O_2$ and then reduced back to the native form in two sequential steps, involving the formation of two enzyme intermediates, Compounds I and II (Figure 8).[36–38]

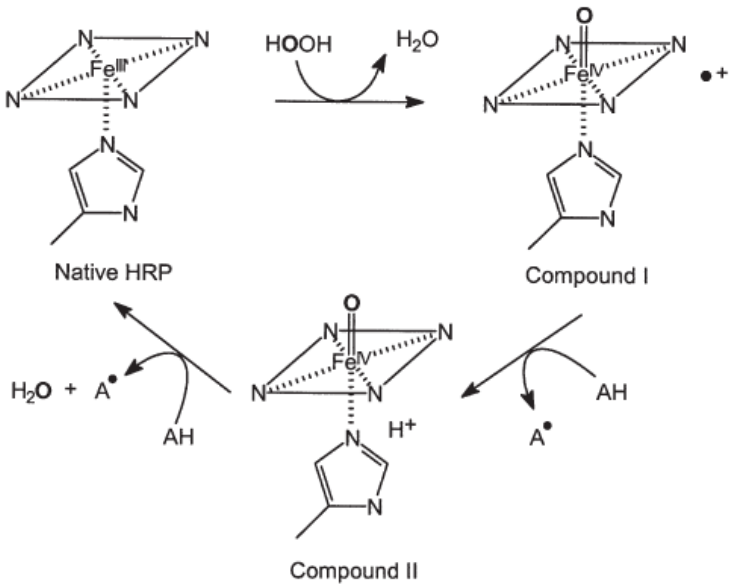


**Figure 8** Reaction cycle of HRP, showing the enzyme intermediates, Compounds I and II.

The first step consists in the cleavage of the $H_2O_2$ molecule, with the concomitant production of water and incorporation of an oxygen atom into Compound I, which contains an oxoferryl group, with the iron in the +4 oxidation state, and a porphyrin π-cation radical.
Compound I is capable of oxidizing a wide range of reducing substrate molecules (AH) by a mechanism involving a single-electron transfer, in which the π-cation radical is first reduced, leading to the formation of the second enzyme intermediate, called Compound II. Compound II, which also contains an oxoferryl group, is further reduced by a second substrate molecule (AH) to the native ferric enzyme ($Fe^{III}$). During this one-electron reduction, the oxygen accepts two protons to form a water molecule and is released from the heme.
Everse has proposed that the bond between the iron and oxygen in both Compounds I and II is not a conventional double bond. In fact, except for its length, all experimental observations indicate that the oxoferryl bond may be a bi-radical, three-centre four electron π-bond.[39]

One of the key factors in the modulation of the redox potential of the *penta*-coordinated complex is the presence of a strong hydrogen bond between the $N_\delta$ atom of the proximal histidine and an aspartate side chain (Asp247): this increases the basicity of the coordinating histidine His170, thus stabilizing high oxidation state intermediates, such as the high valent oxoferryl center, by a charge relay system.[2]

The binding of $H_2O_2$ occurs in the distal site, which is characterized by two completely invariant amino acids in

all plant peroxidases: the distal histidine and the distal arginine (Figure 9). These two residues play a major role in the formation and stabilization of Compound I. The distal histidine (His42) mainly acts as a general acid–base catalyst, facilitating the peroxide anion binding to the heme and assisting the subsequent heterolytic cleavage of the O–O bond during the Compound I formation.[40] The conserved distal arginine (Arg38) is involved in the charge stabilization, mediated by its positively charged guanidinium group, of the developing $OH^-$ leaving group of hydrogen peroxide. Further, once the O–O bond is cleaved, Arg contributes to stabilize the oxoferryl species via hydrogen bond formation.

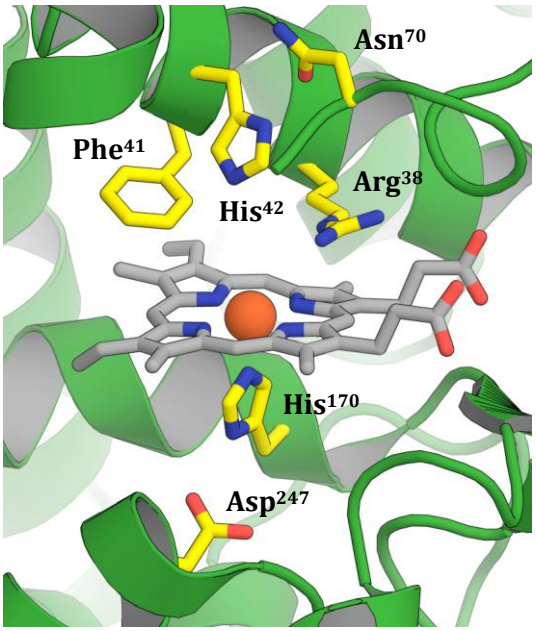


**Figure 9** Detail of the proximal and distal sites of HRP (PDB entry ID: 1H57).

The key role of these highly conserved residues has been proved, since their replacement causes a drastic reduction of Compound I rate formation, and therefore of HRP catalytic activity.[41–43]

Reaction of excess hydrogen peroxide with resting state enzyme gives Compound III, whose structure is best described as a resonance hybrid of $Fe^{2+}$-$O_2$ and the isoelectronic $Fe^{3+}$-$O_2^{-\cdot}$ form. Recently, Berglund and co-workers succeeded in obtaining a three-dimensional movie of the X-ray-driven catalytic conversion of the bound dioxygen species to two molecules of water in the active site.[44] The mechanism involves four successive, one-electron, reductions with the concomitant uptake of a proton, from Compound III to the ferrous HRP, via the intermediate forms of Compound I, Compound II and ferric HRP. The high-resolution crystal structure of Compound III shows dioxygen bound to heme iron in a bent conformation.[44]

## 1.2 From natural to artificial metalloproteins

As highlighted above, almost half of all known proteins contain metal cofactor(s) that are able to serve numerous roles, either structural or functional, such as respiration, water oxidation, molecular oxygen reduction and nitrogen fixation. It is remarkable that, despite the variety of functions in which metalloproteins are involved, the number of utilized metal–based prosthetic groups is relatively small. In fact, such different chemistries are determined by the protein matrix, which influences the environment of the metal cofactor, regulating its catalytic activity and stability.[2] Understanding at a molecular level the mechanism by which the protein part acts, is of fundamental importance in both basic and applied science, to shed light on the detailed mechanisms of fundamental biological processes, and to allow researchers to construct new metalloproteins with desired properties and functions.

Most fundamental aspects of metal cofactor assembly and metalloproteins functions have already been clarified, mainly through structural–functional studies on natural metalloproteins and related mutants. For example, it has been shown that modification of a single amino acid residue can profoundly affect the activity of the enzyme.[45] Despite these progresses, several questions are still open. While the control of the functional specificity by the primary coordination sphere is almost well understood, the contribution of medium and long range interactions

remains to be determined. Thus, it is not surprising that many efforts are being devoted to the development of metalloprotein mimics aimed to:

- ✓ provide further insights for structure-activity relationships;
- ✓ understand the minimal requirements for function;
- ✓ reproduce the properties of the parent natural proteins in smaller molecules, with improved properties, such as higher stability and greater efficiency;
- ✓ construct new, tailor-made molecules useful for biomedical, pharmaceutical, biological, and environmental applications.

Metalloprotein design is more challenging than the design of non-metalloproteins, since it requires a properly folded protein scaffold, which has to include the correct number and type of ligands to determine the appropriate geometry for metal center reactivity. On the other hand, most metal-binding sites are highly chromatic and display distinctive magnetic properties, allowing easier characterization by means of spectroscopic techniques rather than X-ray crystallography or nuclear magnetic resonance (NMR), thus shortening design cycles.[46]

The protein design process can be divided into two steps: the design of the overall scaffold and the design of active sites. Although the design of the overall scaffold and active sites are linked, it is helpful to distinguish these two steps because our knowledge about each step is still not complete.[47]

There are several design approaches: *de novo* design, design or re-design of new metal-binding sites into native scaffolds, and minimalist approach.

*De novo* design or design "from scratch" of a metalloprotein involves constructing a polypeptide sequence that is not directly related to any natural protein and that folds precisely into a defined three-dimensional structure that binds a metal ion.[2] Numerous papers in this area have been published, focused on introducing metal-binding sites into *de novo* designed α-helical bundles, which are one of the most common scaffolds in nature. In stark contrast to the design of α-helical proteins, few successful examples of other *de novo* designed scaffolds have been reported.[46]

Another equally attractive design strategy is the design of active sites into native scaffolds.[47] In fact, evaluating numerous structures in the Protein Data Bank, it emerges that there are many more natural than *de novo* designed protein scaffolds: moreover, several natural protein scaffolds maintain the same fold and similar stability upon mutation. Therefore, metalloprotein design using native instead of *de novo* protein scaffolds may provide more scaffold choices, assuming that they are tolerant to mutations, required for the construction of the metal-binding sites.[46]

The redesign of an existing metal-binding site to introduce new function or metal specificity is amenable to empirical approaches, and relies on the structural differences between template and target proteins. Despite

its simplicity, this approach is still powerful in elucidating structural features important for the change in, or gain of, function by redesign.[46] It is known that biochemical techniques, such as site-directed mutagenesis, have been used extensively to study structure-function relationship in metalloproteins; for example, the loss of activity accompanied by a mutation of highly conserved residues allows the identification of residues essential for function. Although serving a different purpose, the same mutagenesis techniques can be used in metalloprotein design to impart a new function into a protein scaffold by introducing residues that bind metal ions.

Another powerful approach involves a miniaturization process, suitable to build the minimal peptide sequence, which contains sufficient information for proper folding and for an accurate reconstruction of the active site structure.[2] This approach holds the advantage that the designed systems are generally simple enough, and therefore they can be easily synthesized and characterized, and simultaneously the polypeptide sequences are of sufficient size and chemical diversity to accommodate the metal binding site. The miniaturization process can be rationally organized once a structural knowledge of the parent natural system to be miniaturized is available. It is necessary to define: (1) the type and number of constituents to be assembled, (2) the structure to be reconstructed, and (3) the function to be reproduced. These aspects are strictly related. Metalloproteins are well suited to be miniaturized. As illustrated in Figure 10, the metal center represents a pivot point where spheres of variable

diameters that circumscribe part of the protein are centered.[48,49] The larger the diameter of the sphere, the larger the number of constituents included in the model. For a sphere of a given diameter around the metal center, the constituents therein circumscribed are, in general, unconnected parts. Several strategies can be conceived to obtain a miniaturized model. Two or more parts could spontaneously associate to give folded non-covalent self-assembled oligomers, or two or more parts could be covalently connected to give folded monomers.

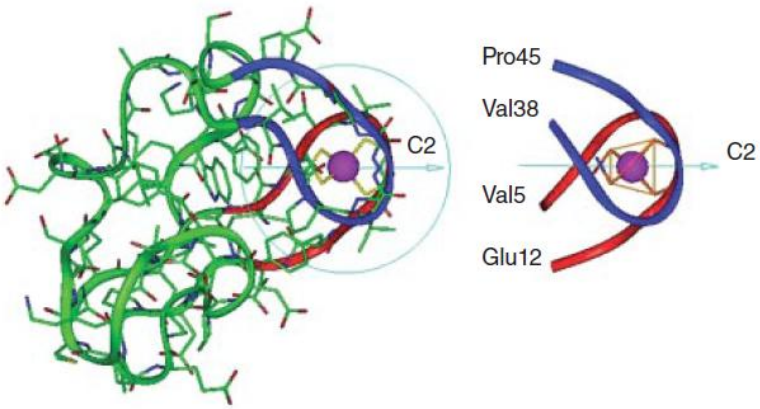


**Figure 10** The full structure of rubredoxin (left) (PDB code: 8RXN), whose active site can be dissected in two symmetry-related idealized β-hairpins, residues 5–12, and 38–45 (right). Reproduced from reference 2.

Design is often aided by empirical approaches based on prior knowledge and experience, the use of computer programs (rational design) or combinatorial selections. Although approaches based on empirical knowledge and rational design using computer programs have been quite successful in designing metalloproteins, it is still difficult to design certain metalloproteins, especially

functional ones, owing to the large number of potential interactions within the active site of a metalloenzyme. In this case, combinatorial design and directed evolution of new metalloenzymes is another powerful method.[46]

An invaluable tool in providing support for design is spectroscopy, although more concrete evidence from three-dimensional structural characterization is essential. In addition, to confirming the initial design, it provides detailed information on what has not been designed correctly, thus providing insights for the next step of design. Furthermore, design of the primary coordination sphere is often not enough to confer structure and/or function; consideration of the environment surrounding the primary coordination sphere is critical to successful design. As a result, the rational engineering of metallo-proteins is an iterative process of design, synthesis and rigorous characterization, until the desired characteristics are obtained. The complexity of protein structures, where a copious number of molecular interactions contributes to the stabilization of the folding and to the fine adjustment of the properties of metal cofactor, makes necessary several redesign cycles, often following a trial and error process. Nevertheless, metalloprotein design will remain an exciting and challenging field in which researchers will continue to spend their efforts in designing metalloproteins with novel functions or improved properties.

### 1.2.1 Heme-peptide models

Peptide-based models have been fundamental in assisting our understanding of the factors governing the heme properties. Standing at the crossroads of small molecule models and large proteins, they seem to be the best candidates to mimic both the structural characteristics and reactivity of the natural systems. Their structures are simpler than their natural counterparts, but they simultaneously have sufficient size and chemical diversity to allow substrate recognition and to reproduce the efficient chemio-, regio-, and stereoselectivity of natural heme-proteins.

The development of peptide-based models takes advantage of recent progress in both the design and synthesis of peptides and proteins. It is now possible to construct recognition and catalytic sites in a scaffold and to systematically vary the amino acid composition, thus allowing one to (1) optimize the structural and functional properties of the initial target, in terms of stability, catalytic activity and selectivity, (2) test how small changes in the sequence can affect the heme properties and functions and (3) investigate not only the effect of variation in the first coordination sphere but also the influence on the activity of medium- and long-range interactions.[21]

It is possible to distinguish two main types of peptide-based heme-protein models: covalent and non-covalent. Here only the models in which peptide chains are covalently linked to the heme will be examined.

Over the years, heme protein models have been developed using quite different strategies. They differ in molecular structures, ranging from simple *meso*-substituted *tetra*-arylmetalloporphyrins to more complex peptide-porphyrin conjugates.[50] The chemical structures of porphyrins usually employed in this model systems are reported in Figure 11.

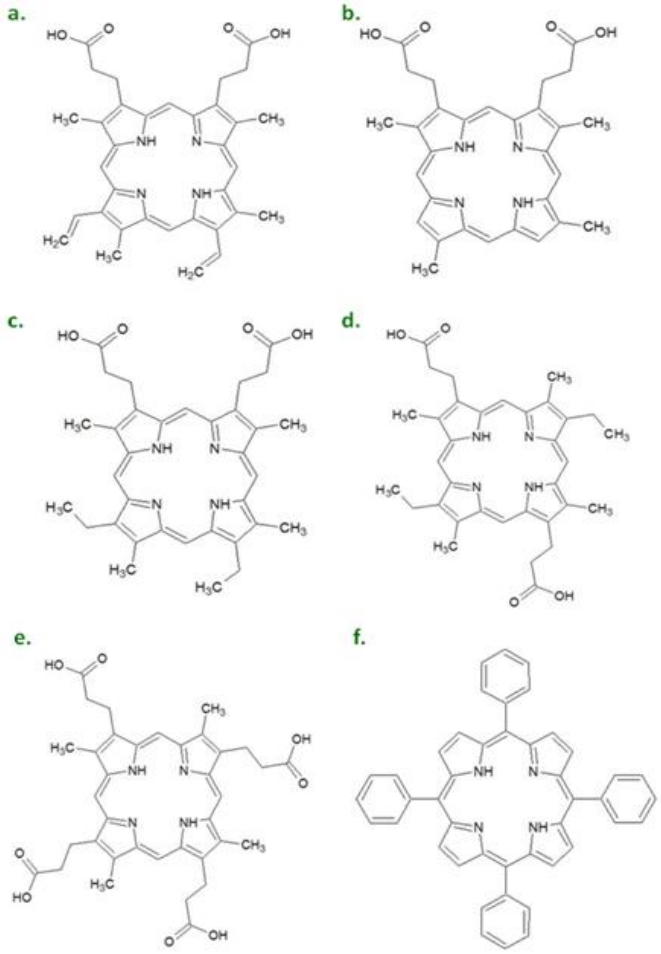


**Figure 11** Chemical structures of porphyrin rings: a) protoporphyrin IX; b) deuteroporphyrin IX; c) mesoporphyrin IX; d) mesoporphyrin II; e) coproporphyrin; f) *meso*-tetraphenylporphyrin.

A common feature in the compounds so far developed is the assembly, around the porphyrin ring, of several different chemical components, which are intended to fulfill the features of the protein matrix and make the heme able to accomplish specific functions.

For example, to obtain oxygen carrier models, two main requirements are needed: (1) stabilization of a *penta*-coordinated complex provided by an imidazole proximal ligand and (2) prevention from further oxidation of the iron-dioxygen complex.[51] In the natural systems these mandatory conditions for efficient reversible oxygen binding are accomplished by the presence of the steric bulkiness of the protein moiety, which prevents the formation of a $\mu$-oxo bridge between two heme complexes and brings the axial ligand in the appropriate position.

An artificial model for the dioxygen activation should embody the following features: (1) an axial thiolate ligand, which contributes to the heterolytic cleavage of O-O bond and modulates the intrinsic reactivity of the high valent iron-oxo species; (2) a steric protection of the porphyrin ring to prevent the rapid bleaching of the catalyst by the oxidizing species produced during the reaction; (3) a chiral environment around the heme, able to selectively recognize a defined substrate, and to control the chemio-, regio- and stereoselectivity in oxygenation reactions.[52–54]

The first low molecular weight heme-protein models date back to the early 1970s. All these systems show *penta*-coordination, obtained both by using hindered ligands and by covalently attaching the axial ligand to the porphyrin ring. A bulky moiety is needed to cover one face

of the porphyrin ring, preventing the formation of an *hexa*-coordinated specie. The bulky moiety could also represent a cavity in which dioxygen can be accommodated.[51]

The pioneering works of Traylor,[55,56] Collman,[54] Momenteau,[57] and Reed[58,59] can be considered fundamental for the development of dioxygen binding molecules; they combined more than one of the above mentioned strategies. Some representative examples are constituted by the picnic-basket,[60] picket-fence[54] and capped[56] porphyrin systems, where the coordination state of the iron(II) is achieved by using hindered substituents on the *meso* or the pyrrole positions of a 5, 10, 15, 20-tetraphenylporphyrin (Figure 12).

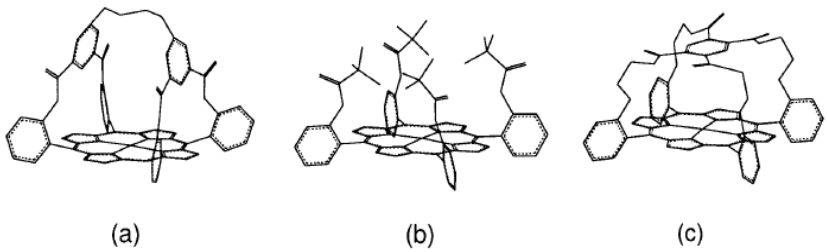


**Figure 12** Dioxygen binding model compounds: (a) picnic-basket, (b) picket-fence and (c) capped porphyrin. Reproduced from reference 50.

These systems can be considered fundamental for the development of dioxygen binding molecules and have contributed to a better understanding, at a molecular level, of the properties of the natural heme-proteins. Even though they display enhanced and interesting activity, their practical application is limited to the use in organic solvent.

In more recent years, the field of heme-protein mimetics broadens to include more elaborate peptide-

based models. The works on chelated hemes, which are characterized by a imidazole or pyridine ligand covalently bound to the propionic group of pyrro-, proto-, meso- and deuteroheme,[55,61] represent milestones to demonstrate the importance of covalently derivatized porphyrin rings and to set the stage for the development of more sophisticated models.

Peptide-based models seem to be better candidates to mimic both the structural characteristics and reactivity of the natural systems. Peptide architecture around the heme can serve for substrate recognition and to reproduce the efficient chemio-, regio-, and stereoselectivity of natural heme-proteins. Peptide models stand at the crossroads of small molecule models and large proteins. Their structures are simple and hence more easily understood than their natural counterparts. They simultaneously have sufficient size and chemical diversity to allow the construction of functional binding and catalytic sites.[62–65]

Quite different strategies were used for developing covalent peptide-porphyrin systems. The development of peptide-based models takes advantage of recent progress in both the design and synthesis of peptides and proteins. It is now possible to construct rigid scaffolds able to accommodate substantial changes in their sequence without loosing their three-dimensional structure because the principles governing folding and stability of peptides and proteins are better understood and advanced tools for their design are available.[65–72] Hence, it is possible to build recognition and catalytic sites in a scaffold and to systematically vary the amino acid composition, thus

allowing one to: (1) optimize the structural and functional properties of the initial target, in terms of stability, catalytic activity and selectivity, (2) test how small changes in the sequence affect the properties of the heme and whether they are able to switch the heme function from one to another, and (3) investigate not only the effect of variation in the first coordination sphere but also the influence on the activity of medium- and long-range interactions.

Peptide models offer the additional advantage of solubilizing the high hydrophobic heme in aqueous solution by simply accommodating the heme group in a hydrophobic pocket of an amphiphilic structure. Finally, the functional parameters can be improved with an iterative process of redesign and synthesis.

Microperoxidases (MPs) are natural covalent heme-peptide fragments, which can be obtained by the proteolytic digestion of cytochromes c.[73,74] Their peptide moiety is covalently linked to the heme *c* through thioether bounds, since contains the Cys-$(Xaa)_2$-Cys motif. Being provided with the proximal histidine of the parent cytochrome c, microperoxidases are characterized by a *mono*-histidine coordination. To date no crystal structure of any microperoxidase has been reported. It has been suggested that the peptide retains a conformation very similar to that of the amino acid residues of the parent protein. In horse heart cytochrome *c* the *N*-terminal residues up to Cys14 are part of an a-helix that terminates with a type III β turn between Cys14 and Cys17.[75] Molecular dynamics simulation of MP8 and MP11 suggests that the peptide is confined to shielding the proximal face

of the porphyrin and the distal face is completely open to solvent. MP8 in aqueous solution has its amino acids largely arranged as a torus in a plane parallel to the porphyrin.[76]

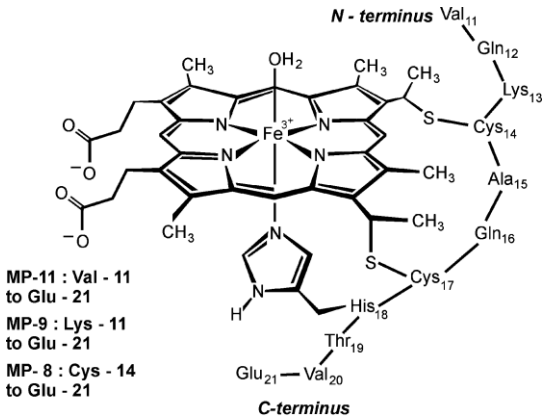


**Figure 13** Three of the most commonly studied microperoxidases (MPs): MP11, MP9 and MP8. The amino acid residue numbering is that of the parent cytochrome *c* from horse heart. Reproduced from reference 76.

MP8, MP11 and their derivatives were proved to be effective catalysts in oxidation and oxygenation reactions. However, the applications of microperoxidases as mini-enzymes are significantly limited by their tendency to aggregate in aqueous solutions and their low stability under catalytic conditions. Accessibility of the distal side causes degradation of the porphyrin ring during catalysis, either by the direct action of $H_2O_2$ or by reactions with another active iron-oxo species. Nevertheless, the peptide moiety plays an important protective role toward the bleaching of the catalyst, if one consider that the nude protoporphyrin is less stable than Microperoxidases.[21]

Casella and co-workers first reported synthetic deuteroheme-peptide conjugates in an attempt to study how peptide sequences influence the heme reactivity.[77–82] The molecular models of these deuteroheme complexes, developed as both *mono*-peptide and *bis*-peptide adducts, are shown in Figure 14.

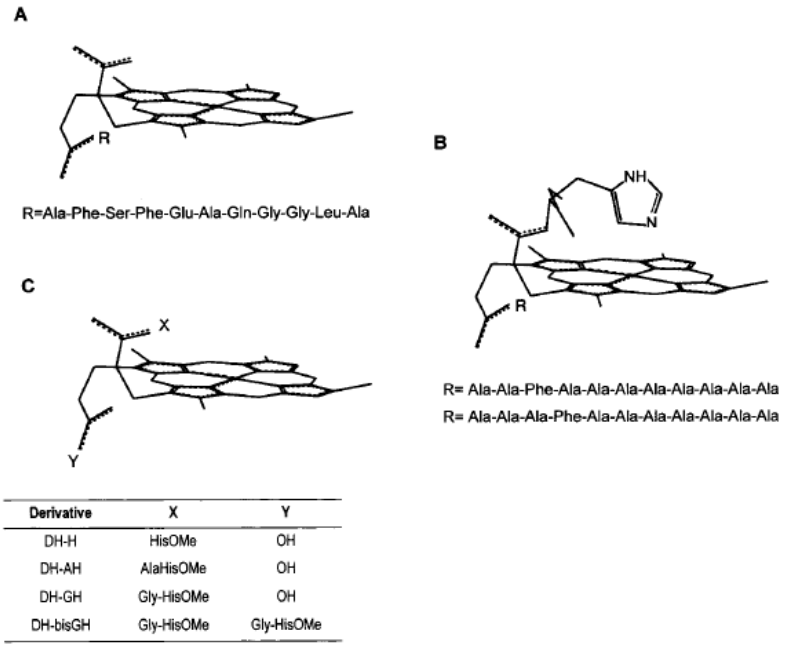


| Derivative | X | Y |
|---|---|---|
| DH-H | HisOMe | OH |
| DH-AH | AlaHisOMe | OH |
| DH-GH | Gly-HisOMe | OH |
| DH-bisGH | Gly-HisOMe | Gly-HisOMe |

**Figure 14** Molecular structures of chelated deuteroheme complexes: (A) deuteroheme undecapeptide; (B) chelated deuteroheme undecapeptide; (C) chelated deuteroheme. Reproduced from reference 21.

The covalent modification of deuteroheme with different peptides was simply achieved by employing the solution methods of peptide synthesis.[77,78] The synthesis of the chelated deuteroheme *mono*-peptide complexes usually afforded a mixture of two products containing the peptide linked at either position 2 or 18 of deuteroheme. Only in a

few cases were these structural isomers separated; otherwise the isomer mixture was studied.

In the first molecule developed, an undecapeptide was covalently N-terminally linked to the propionic group of deuteroheme (Figure 14A).[77] This medium sized peptide contains polar and acidic residues, which should confer solubility to deuteroheme in a protic medium. The presence of the peptide chain strongly influences the binding and catalytic properties of deuteroheme. First, titration of deuteroheme undecapeptide with imidazole, followed by visible spectroscopy, showed that the complex binds up to two imidazoles. The binding equilibrium occurred in two steps: the first imidazole binds with high affinity, while the affinity for the second imidazole is markedly lower. The authors hypothesized that the folding of the peptide chain in the *mono*-imidazole adduct greatly limits the accessibility to the sixth iron coordination position. The catalytic properties of the deuteroheme-undecapeptide complex in peroxidase- and catalase-like reactions were investigated by using thioanisole or tyrosine as substrates and hydrogen peroxide as oxidant. In the catalytic oxidation of D- and L-tyrosine, the complex exhibited some stereoselectivity ascribed to specific interactions between the substrate and the peptide chain.

In subsequent works, the same investigators developed chelated deuteroheme complexes in an effort to study the effects of the axial ligand on the catalytic properties of deuteroheme.[78] In these new systems, a histidine methylester or a histidine containing dipeptide, covalently linked to one of the two propionic groups, constituted the

chelating arm (Figure 14B). A different peptide chain was linked to the second propionic group, rationally chosen with the aim of evaluating the effect of specific amino acids in inducing stereoselective oxidation.
Two complexes, each containing a different phenylalanyl-polyalanine sequence, were studied (Figure 14B).[78] The kinetic parameters for the catalytic oxidation of D- and L-tyrosine, using *tert*-butyl hydroperoxide, revealed a marked difference in the chiral discrimination ability of the two complexes, suggesting that the Phe residue position influences the chiral discrimination.
The analysis of the axial-ligand distortion effects on the catalytic and binding properties of deuteroheme was investigated by examining the behavior of complexes bearing short chelating arms: DH-His, DH-Ala-His, and DH-Gly-His (Figure 14C).[79,80] Molecular mechanics calculation revealed the length of the chelating arm critically affects the coordination. The presence of two amino acid residues in the chelating arm causes less strain in the axial coordinative bond with respect to the DH-His complex. The strain energy influences the catalytic and binding properties of the metal center, as a consequence of an altered electron distribution in the strained complex.

Benson and co-workers developed a series of peptide-sandwiched mesoheme complexes, indicated as PSMs.[83–86] In PSMs the mesoheme II or IX is covalently linked to one or two peptide chains via an amide linkage between the propionate heme function and the $N_\varepsilon$ of lysine residues. A His residue in each peptide coordinates the heme iron, thus allowing the peptide chains to fold above

and below the porphyrin ring, giving rise to a sandwich structure.[83]

One of the main features of PSM molecules is that a random coil-helix transition of the peptides occurs upon histidine to iron binding. The first derivatives of the PSMs series are characterized by the presence of a 13-residue peptide covalently linked to the mesoheme propionic groups. The peptide was designed to have high helical propensity and to convey water solubility to the structure. A polyalanine sequence, containing Glu residues in the solvent-exposed position, was created. Lys and His were placed into the sequence to achieve the covalent linkage to the porphyrin and the iron coordination, respectively.

To rationalize the factors that impart stability to the PSMs molecules, new derivatives were developed.[84] By changing the Lys-His separation, the chelate effect and the resulting strain in the Fe-His axial bond were evaluated. In addition, in some derivatives, the position of Lys was changed from N- to C-terminus, i.e., reversed peptide sequences were synthesized.

The UV-Vis, CD, and EPR analysis of both *mono*- and *bis*-peptide adducts revealed that stability of PSMs is controlled by several factors. In all derivatives His is able to coordinate the iron, giving rise to pentacoordinated high-spin species in the *mono*-adducts and low-spin hexacoordinated species in the *bis*-adducts. It was demonstrated that an important factor that modulates the stability of PSMs is the length of the chelating arm, i.e., the distance between Lys and His residues.

A series of α-helical peptides covalently linked to

heme were also studied by Mihara and co-workers.[87,88] They developed two three-helix bundle proteins, 3α-H9 and 3α-H12, covalently bound to meso-heme IX as models of peroxidases.[88] The distal His ligand was placed in different positions within the two systems to regulate six- or five-coordination of the heme iron.

The two molecules showed different activities toward the oxidation of *o*-methoxyphenol to *tetra*-guaiacol using hydrogen peroxide as oxidant. In particular, a good correlation was found between the coordination states of the heme and the catalytic efficiency of the systems, i.e., the molecule containing a higher content of five-coordination showed the best activity. However, the accessibility of hydrogen peroxide and its destructive effect toward the heme should be carefully balanced in order to enhance the activity.

More recently, a new artificial heme-enzyme, MP3, has been designed, by combining the excellent structural properties of four-helix bundle protein scaffolds with the activity of natural peroxidases.[89] It houses two peptide chains of different composition covalently linked the deuteroporphyrin IX through the side chain of two lysine residues, to obtain an asymmetric helix–loop–helix/heme/helix–loop–helix sandwich arrangement. MP3 is a *penta*-coordinated complex, characterized by: a histidine residue on one chain as axial ligand to the heme iron; an empty distal site able to accommodate exogenous ligands or substrates; an arginine residue in the distal site that should assist in hydrogen peroxide activation, mimicking Arg38 in HRP.

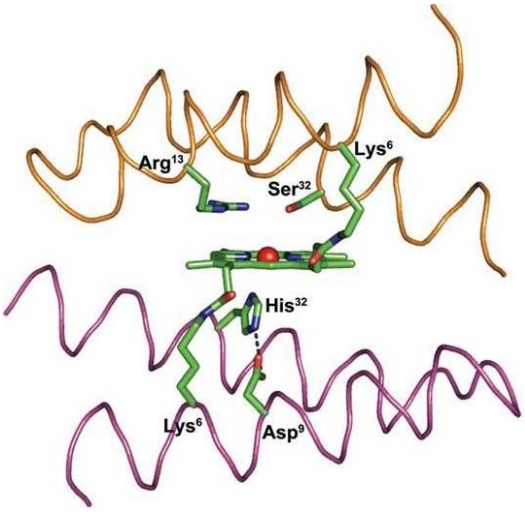


**Figure 15** Computer model of MP3. A trace representation of the helices with key residues depicted as sticks. Reproduced from reference 89.

MP3 has been synthesized and characterized as its iron complex. CD spectroscopy suggests that MP3 scaffold possesses a high intrinsic helical propensity in water, even if complete folding of the helices occurs only in the presence of the helix-inducing solvent TFE (2,2,2-trifluoroethanol); UV/Vis, MCD and EPR spectroscopies give insight into the coordination geometry and spin state of the metal, confirming *mono*-His coordination above pH 4. MP3 shows a high catalytic turnover and efficiency in the oxidation ABTS (2,2'-azino-bis(3-ethylbenzthiazoline-6-sulphonic acid)) by $H_2O_2$, with a $k_{cat}$ value only eight-fold lower than that of HRP under the experimental conditions for maximal activity for each enzyme, but ten-fold higher than that of HRP at neutral pH.

### 1.2.2 Mimochromes

The *Artificial Metallo-Enzyme Group* in Naples, where this work has been carried out, has approached the challenge of constructing heme-protein models using a miniaturization process. Thanks to this strategy, a class of artificial heme-proteins has been developed, named Mimochromes.

Mimochromes are peptide-sandwiched deutero-heme systems, obtained by miniaturizing natural heme-proteins, in order to partially reproduce their structural and functional properties in smaller compounds. Analyzing natural heme-protein structures, it emerges that the prosthetic group is almost completely embedded between two relatively small α-helical peptide fragments.

The natural motif helix/heme/helix was used as a template to engineer the family prototype, Mimochrome I.[90–92] To design a mini-heme protein, the copious interactions of the peptide moiety with the heme commonly found in natural proteins were replaced by a few strong local constraints. The smallest sequence required for a complete coating of one face of the heme, was identified in a nine-residue peptide, based on the F helix of hemoglobin β-chain (Figure 16).

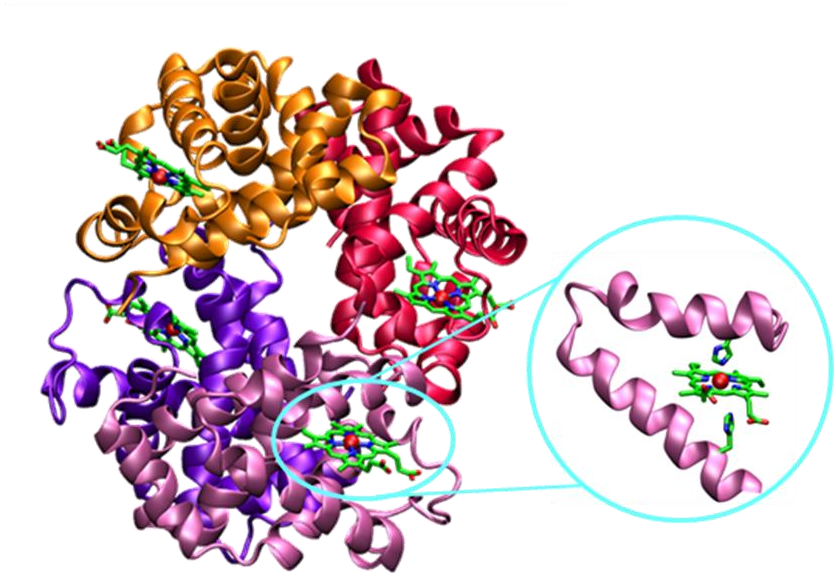

**Figure 16** Three-dimensional representation of the X-ray crystal structure of human deoxyhemoglobin. Insert: E and F helixes in the β-chain; the F helix was used to design Mimochrome I peptide sequence.

Mimochrome I peptide sequence contains: a central His residue to coordinate the heme iron; Leu residues at positions i-4 and i+4 relative to the His to hydrophobically interact with the heme macrocycle; a lysine residue to anchor the heme group; two alanine residues (that substitute Ser89 and Cys93), chosen for their high α-helical propensity; a glutamine and an asparagines residues (that substitute Glu90 and Asp94), to remove charge residues that could destabilize the target conformation (Figure 17).

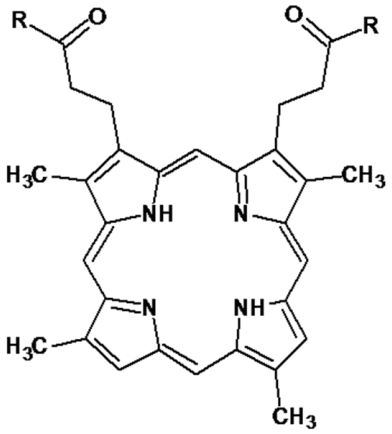


| | | |
|---|---|---|
| Mimochrome I | R= | Ac-L-A-Q-L-H-A-N-K-L-$NH_2$ |
| Hemoglobin | $Leu^{88}$-$Leu^{96}$ | L-S-E-L-H-C-D-K-L |

**Figure 17** Schematic structure of Mimochrome I and comparison between its peptide sequence and L88-L96 fragment of the F helix in the β-chain of hemoglobin.

Deuteroporphyrin IX was preferred to the more common protoporphyrin IX to avoid the possibility of degradation of the sensitive vinyl substituents during the synthesis. Two identical copies of the peptide were covalently linked to the porphyrin propionic groups through the ε-amino function of Lys, obtaining a *pseudo-$C_2$*-symmetric dimer (Figure 18).[90]

**Figure 18** Molecular model of $Fe^{III}$-Mimochrome I. Reproduced from reference 90.

Interestingly, the insertion of cobalt ion into the porphyrin ring gave two diastereomers. In fact, the flexibility of the linker between the peptide and the deuteroporphyrin ring allows each peptide chain to be positioned either above or below the porphyrin plane, producing enantiomeric configurations around the metal center. The presence of the substituents on the porphyrin ring and the chirality of the peptide chain make the Δ and Λ isomers of Co(III)-Mimochrome I diastereomeric forms. This finding was confirmed by structural NMR characterization of the two previously separated Co(III) complexes.[92]

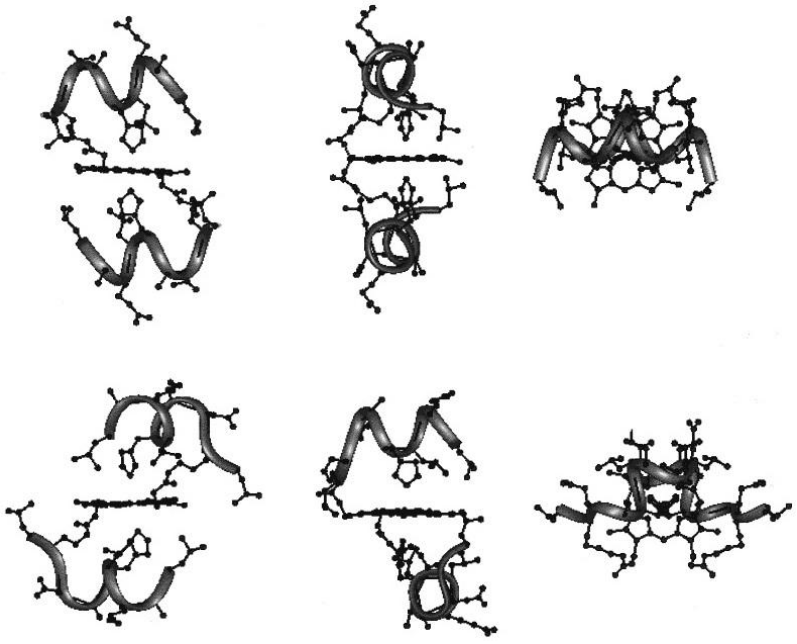

**Figure 19** Front, side and top views of the average molecular structures obtained from NMR data and RMD calculations for Δ isomer (top) and Λ isomer (bottom) of Co(III)-Mimochrome I. Reproduced from reference 21.

The information derived from Mimochrome I was applied for improving the design. Over the years, other models have been developed, with the same or different peptide chains linked to the deuteroporphyrin ring (Table 1).

| Mimochrome | | $R_1$, $R_2$ |
|---|---|---|
| I | $R_1$=$R_2$ | Ac-L-A-Q-L-H-A-N-K-$NH_2$ |
| II | $R_1$=$R_2$ | Ac-D-L-S-D-L-H-S-K-K-L-K-I-T-L-$NH_2$ |
| IV | $R_1$=$R_2$ | Ac-E-S-Q-L-H-S-N-K-R-$NH_2$ |
| III, V | $R_1$ | Ac-D-E-H-K-L-H-S-K-K-R-K-I-T-L-$NH_2$ |
| | $R_2$ | Ac-D-E-H-K-L-Y-S-K-K-R-K-I-T-L-$NH_2$ |
| VI | $R_1$ | Ac-D-E-Q-Q-L-H-S-Q-K-R-K-I-T-L-$NH_2$ |
| | $R_2$ | Ac-D-E-Q-Q-L-S-S-Q-K-R-$NH_2$ |

H= Histidine coordinating the metal center; Y= Gly or Ser
K= Lysine bound to the deuteroporphyrin

**Table 1** Peptide sequences of the developed Mimochromes.

Mimochrome II[93] presents two identical and elongated peptide chains, modeled in an extended conformation, whose residues carefully chosen in order to improve water solubility and to stabilize a unique diastereomer.

Later on, another complex with identical peptide chains was designed: Mimochrome IV.[94–96] This model considers *intra*-molecular *inter*-helical interactions,

provided by an ion pair between the carboxylate side chain of a Glu residue at position 1 of one peptide chain and the guanidine group of an Arg residue at position 9 of the other peptide chain (both side chains being modelled in an appropriate extended conformation). Moreover, the helix is further stabilized by a positively charged residue (Arg) at the C-terminus, and a negatively charged residue (Glu) at the N-terminus, which reduce the intensity of the helix dipole.

Mimochrome IV was the first molecule with a unique topology of the Mimochrome family. Its Co(III) complex was extensively characterized both in solution and solid state, confirming the presence of the Λ topology (Figure 20). The structural characterization evidenced that in the solid state crystal packing interactions strongly affects the molecular folding, with *intra*-chain Glu1–Arg9 ion pairs that are preferred over the designed, and experimentally found in solution, *inter*-chain interactions.

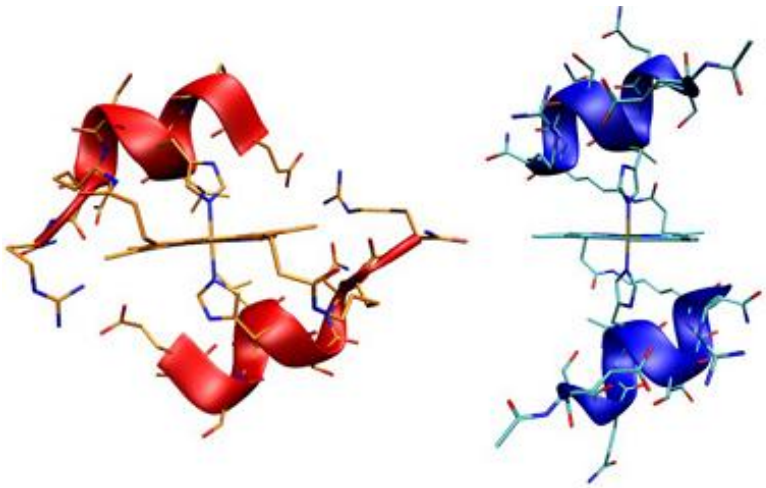

**Figure 20** NMR (on the left) and X-ray (on the right) structures of Co(III)-Mimochrome IV.

### 1.2.2*a Mimochrome VI and its analogues*

Since Mimochrome IV, despite its small size, adopts a unique well-defined secondary and tertiary structure, the next goal was to introduce peroxidase-like activity into Mimochrome's architecture.

Peroxidases are very appealing for oxidation reactions, because they have high activity towards a wide range of substrates; despite this, their high production costs and bleaching during catalysis limit their potential applications. Therefore, it would be better use simpler artificial metalloenzymes with improved stability and efficiency.

Among the Mimochrome family, Mimochrome VI was the first model showing catalytic functionality.[97] It is made up by a 14-residue peptide with a His residue at position 6, as axial ligand to the heme (proximal site) and a 10-residue peptide lacking a heme-coordinating residue, to create a cavity around the metal ion (distal site). This unsymmetrical *penta*-coordinated *mono*-His model was designed starting from the NMR solution structures of both the symmetric *bis*-His Mimochrome II and Mimochrome IV.

The tetradecapeptide was designed to adopt a short helical conformation (residues 1-9), a loop $\gamma\beta_D$ (residues 10 and 11) and a short β-strand (residues 12-14) that folds back to interact with the helical part; the decapeptide also was designed to adopt a helical conformation (residues 1-8). Stabilization of the secondary structure is also contributed by the positively charged Arg10 and the negatively charged Glu2 at the C-terminal

and N-terminal ends, respectively, with the opposite sign relative to the helix dipole.

The tertiary structure can be viewed as a sandwich, characteristic of the Mimochrome family, in which the two peptide chains embrace the metalloporphyrin; the helixes of the peptide chains are antiparallel to each other and the helix axes are about parallel to the porphyrin plane. Stabilization of the tertiary structure is enhanced by *inter*-chain ion pairs between the carboxylate side chains of a glutamate residue (Glu2) on one helix and the guanidine group of an arginine residue (Arg10) on the other helix. Finally, several glutamines (Gln3, 4 and 8) and a serine (Ser7) were introduced in the solvent exposed positions to promote water solubility.

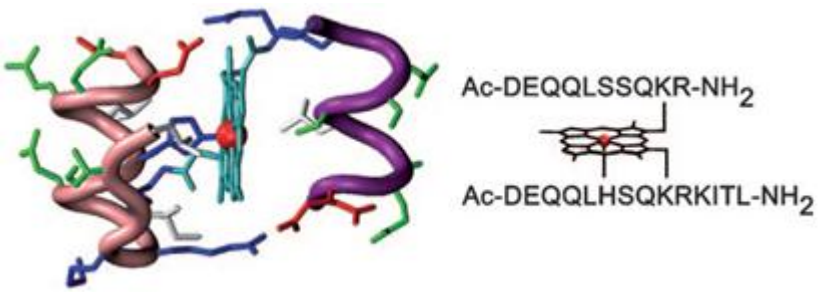


**Figure 21** Molecular model and amino acid sequence of $Fe^{III}$-Mimochrome VI. Reproduced from reference 97.

Catalysis experiments showed that $Fe^{III}$-Mimochrome VI behaves like a very promising artificial peroxidase, as it catalyses oxidation reactions by the activation of $H_2O_2$.

In the oxidation of ABTS, none of the synthetic models developed so far has $k_{cat}$ as high as that of HRP ($k_{cat}$ = 4100

$s^{-1}$, pH 4.6). $Fe^{III}$–Mimochrome VI approaches the catalytic performance of the natural enzyme, since it has a $k_{cat}$ value only 11-fold lower than that of HRP, in the experimental conditions for maximal activity for each enzyme, and a $k_{cat}$ value of $Fe^{III}$–Mimochrome VI almost 7-fold higher than that of HRP at neutral pH.

| Enzyme | $k_{cat}\cdot10^{-2}$ ($s^{-1}$) | $K_m^{H_2O_2}$ (mM) | $K_m^{AH_2}\cdot10^2$ (mM) | $k_{cat}/K_m^{H_2O_2}$ ($mM^{-1}\ s^{-1}$) | $k_{cat}/K_m^{AH_2}\cdot10^{-3}$ ($mM^{-1}\ s^{-1}$) |
|---|---|---|---|---|---|
| **Mimochrome VI** | 3.7 ± 0.1 | 44 ± 2 | 8.4 ± 0.2 | 8.4 ± 0.5 | 4.4 ± 0.2 |
| **HRP** | 62 ± 1 | 0.85 ± 0.01 | 107 ± 1 | (7.3±0.2)·10³ | 5.8 ± 0.1 |

**Table 2** Catalytic parameters for the oxidation of ABTS ($AH_2$) by $H_2O_2$ activation for Mimochrome VI and HRP in the experimental conditions for maximal activity for each enzyme.

The specific activity of $Fe^{III}$-Mimochrome VI is comparable with that of highly purified HRPs ($1.0\cdot10^2$ mmol $g^{-1}$ $s^{-1}$ and $1.4\cdot10^2$ mmol $g^{-1}$ $s^{-1}$, respectively, for ABTS oxidation); this highlights both its high catalytic efficiency and small molecular mass, compared to natural peroxidases. Moreover, it exhibits multiple turnover kinetics: more than 4000 turnovers within 10 min in the ABTS oxidation.

$Fe^{III}$-Mimochrome VI also catalyzes: the oxidation of guaiacol, with a $k_{cat}$ value 50-fold lower than that of HRP; the conversion of phenols to 4- and 2-nitrophenol in presence of $NO_2$ and $H_2O_2$ in high yields; the tyrosine coupling.

Recently, the ability of $Fe^{III}$-Mimochrome VI adsorbed on mesoporous ITO (indium tin oxide) electrodes

to perform the electrochemical reduction of molecular dioxygen has been proved.[98] This encouraging results will lead to a more detailed study of the mechanism of this reaction, in order to open the way of Mimochrome VI's applications in electrochemical biosensor development.

Finally, $Fe^{III}$-Mimochrome VI was used in combination with antibodies aimed to develop more sensitive immunochemical detection assays, offering high performance and economic benefits. In fact, thanks to its low molecular weight (3.5 kDa), it is possible to increase the conjugation ratio enzyme/antibody, which results in a signal amplification. To date, it was possible to obtain antibodies (polyclonal human IgG) functionalized with about 13 molecules of this mini-enzyme: this enzyme/ antibody ratio is significantly higher respect to the commercial immunoglobulins, which are usually linked to 3 or 4 HRP molecules. These conjugates retain the catalytic activity, and immunoreactivity assays are in progress.[99]

All these features indicate $Fe^{III}$–Mimochrome VI as an attractive low-molecular-weight enzyme, and encouraged to further design, in order to improve the catalytic properties and to gain insight into the structure-activity relationship.

In the next stage of design, the attention was focused on Glu2 and Arg10, in both deca and tetradeca chains, since both peptides are involved in finely tune the reactivity. In Mimochrome VI design, these residues were placed at the N- and C- termini, respectively, to contribute to stabilize both secondary and tertiary structures. By

individually replacing Glu2 and Arg10 on both peptide chains with a Leu residue, four analogues were obtained, which were screened for peroxidase-like activity.[100]

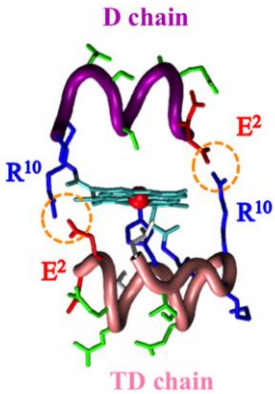


| | | |
|---|---|---|
| MC6 | Ac-D-E-Q-Q-L-H-S-Q-K-R-K-I-T-L-NH$_2$ | (*TD*) chain |
| | Ac-D-E-Q-Q-L-S-S-Q-K-R-NH$_2$ | (*D*) chain |
| E$^2$L(*TD*)-MC6 | Ac-D-L-Q-Q-L-H-S-Q-K-R-K-I-T-L-NH$_2$ | (*TD*) chain |
| | Ac-D-E-Q-Q-L-S-S-Q-K-R-NH$_2$ | (*D*) chain |
| R$^{10}$L(*TD*)-MC6 | Ac-D-E-Q-Q-L-H-S-Q-K-L-K-I-T-L-NH$_2$ | (*TD*) chain |
| | Ac-D-E-Q-Q-L-S-S-Q-K-R-NH$_2$ | (*D*) chain |
| E$^2$L(*D*)-MC6 | Ac-D-E-Q-Q-L-H-S-Q-K-R-K-I-T-L-NH$_2$ | (*TD*) chain |
| | Ac-D-L-Q-Q-L-S-S-Q-K-R-NH$_2$ | (*D*) chain |
| R$^{10}$L(*D*)-MC6 | Ac-D-E-Q-Q-L-H-S-Q-K-R-K-I-T-L-NH$_2$ | (*TD*) chain |
| | Ac-D-E-Q-Q-L-S-S-Q-K-L-NH$_2$ | (*D*) chain |

**Figure 22** On the left, Fe$^{III}$-Mimochrome VI molecular model, highlighting the R$^{10}$-E$^2$ ion pair interactions. On the right, peptide sequences of Fe$^{III}$-Mimochrome VI (MC6) and its analogues: acid, basic and non-polar residues in position 2 and 10 are indicated in red, blue and green, respectively. Reproduced from reference 100.

The peroxidase activity towards ABTS was evaluated in the same condition used for Fe$^{III}$-Mimochrome VI (MC6): 50 mM phosphate buffer pH 6.5, 50% TFE (v/v), T=25 °C. The apparent catalytic constant of the analogues substituted on the tetradeca chain are about 2-fold higher with respect to MC6. The best performances were obtained for E2L(*TD*)-MC6, which displays improvement in the apparent catalytic constant ($k_{cat}$ = 7.8·10$^2$ s$^{-1}$), and catalytic efficiency for both $H_2O_2$ and ABTS ($k_{cat}/K_m$ = 25 mM$^{-1}$ s$^{-1}$, and 16·10$^3$ mM$^{-1}$ s$^{-1}$, respectively). In contrast, the analogues with the altered deca chain showed an almost

unmodified reactivity compared with MC6, and the worst one among them is E2L(*D*)-MC6 analogue.
All MC6 analogues were able to perform several thousands of turnovers, without bleaching. The turnover numbers (T.O.N.) reflects the trend of the catalytic efficiency, being higher in E2L(*TD*)-MC6 and lower in R10L(*TD*)-MC6.

| Enzyme | pH | $H_2O_2$ | ABTS | | $H_2O_2$ | ABTS | |
|---|---|---|---|---|---|---|---|
| | | $K_m$ (mM) | $K_m$ $10^2$ (mM) | $k_{cat}$ $10^{-2}$ ($s^{-1}$) | $k_{cat}/K_m$ (mM $s^{-1}$) | $k_{cat}/K_m$ $10^{-3}$ (mM $s^{-1}$) | T.O.N. $10^{-3}$ |
| MC6 | 6.5 | 44 ± 2 | 8.4 ± 0.2 | 3.7 ± 0.1 | 8.4 ± 0.6 | 4.4 ± 0.2 | 4.0 |
| $E^2$L(*TD*)-MC6 | 6.5 | 31 ± 2 | 5.0 ± 0.4 | 7.8 ± 0.6 | 25 ± 3 | 16 ± 2 | 5.9 |
| $R^{10}$L(*TD*)-MC6 | 6.5 | 54 ± 2 | 3.8 ± 0.1 | 6.8 ± 0.3 | 13 ± 1 | 18 ± 1 | 5.6 |
| $E^2$L(*D*)-MC6 | 6.5 | 96 ± 7 | 11 ± 1 | 3.8 ± 0.3 | 4.0 ± 0.6 | 3.4 ± 0.6 | 3.6 |
| $R^{10}$L(*D*)-MC6 | 6.5 | 18 ± 1 | 3.0 ± 0.2 | 1.7 ± 0.1 | 9 ± 1 | 5.7 ± 0.7 | 3.3 |

**Table 3** Steady-state kinetic parameters for $Fe^{III}$-Mimochrome VI (MC6) and its analogues, in the same experimental conditions (50 mM phosphate buffer pH 6.5, 50 % TFE (v/v), T=25 °C). Reproduced from reference 100.

A detail spectroscopic characterization allowed to hypothesize a catalytic role of Arg10 on the decapeptide chain, whose side chain may approach the heme, contributing to stabilize Compound I and helping ligand binding, similarly to the conserved distal arginine (Arg38) in HRP. In fact, there is experimental evidence that the E2L(*TD*)-MC6 catalytic cycle occurs with a peroxidase-like mechanism, through the formation of Compound I, proving its similarity with natural peroxidases, whose reactivity is influenced by the proximal and distal heme environments.[100]

The main drawback of Mimochrome VI and its analogues relies in the lack of three-dimensional structures.

The analysis of the NMR spectrum of the diamagnetic $Co^{III}$-Mimochrome VI complex revealed the presence of different species in solution. The availability of a three-dimensional structure would allow us to:

- verify the correctness of the design;
- obtain a more detailed structure-activity relationship for the next step of design.

## 1.3 Aim of the project

This PhD project has been focused on the development of new low molecular weight, stable and cost-effective artificial heme-enzymes, which couple high activity with a well-defined structure for biosensing and diagnostic applications.

In particular, the two main objectives which this project aims to, are:

- ✓ improving the catalytic performance of $Fe^{III}$-Mimochrome VI and its analogues;
- ✓ overcoming the presence of multiple species in solution, which made the attempts to solve the structure of Mimochrome VI unsuccessful.

These two objectives are strictly related, since the availability of a unique and well-defined three-dimensional structure will allow an accurate structure-activity relationship analysis that will help in redesigning the enzyme with improved catalytic performance.

References

(1) Thomson, A. J.; Gray, H. B. *Curr. Opin. Chem. Biol.* **1998**, *2* (2), 155–158.
(2) Maglio, O.; Nastri, F.; Lombardi, A. In *Ionic Interactions in Natural and Synthetic Macromolecules*; Ciferri, A., Perico, A., Eds.; John Wiley & Sons, Inc.: Hoboken, NJ, USA, 2012; pp 361–450.
(3) Atkins, P. *Shriver and Atkins' inorganic chemistry*; Oxford University Press, 2010.

(4) Holm, R. H.; Kennepohl, P.; Solomon, E. I. *Chem. Rev.* **1996**, *96* (7), 2239–2314.
(5) Bertini, I.; Gray, H. B.; Lippard, S. J.; Valentine, J. S. *Bioinorganic chemistry*; University Science Books, 1994.
(6) Dolphin, D. *The porphyrins Vol. 7, Biochemistry, Part B.*; Academic Press: New York [etc.], 1979.
(7) Gray, H. B.; Winkler, J. R. *Annu. Rev. Biochem.* **1996**, *65* (1), 537–561.
(8) Chan, M. K. *J. Porphyr. Phthalocyanines JPP* **2000**, *04* (04), 358–361.
(9) Privalle, C. T. *Proc. Natl. Acad. Sci.* **1983**, *80* (3), 702–706.
(10) Yoshikawa, S. In *Advances in Protein Chemistry*; Joan Selverstone Valentine, E. B. G., Ed.; Copper-Containing Proteins; Academic Press, 2002; Vol. 60, pp 341–395.
(11) Schäfer, G.; Purschke, W.; Schmidt, C. L. *FEMS Microbiol. Rev.* **1996**, *18* (2-3), 173–188.
(12) Goldberg, M.; Dunning, S.; Bunn, H. *Science* **1988**, *242* (4884), 1412–1415.
(13) Narula, J.; Pandey, P.; Arbustini, E.; Haider, N.; Narula, N.; Kolodgie, F. D.; Dal Bello, B.; Semigran, M. J.; Bielsa-Masdeu, A.; Dec, G. W.; Israels, S.; Ballester, M.; Virmani, R.; Saxena, S.; Kharbanda, S. *Proc. Natl. Acad. Sci.* **1999**, *96* (14), 8144–8149.
(14) Reedy, C. J.; Gibney, B. R. *Chem. Rev.* **2004**, *104* (2), 617–650.
(15) Martinez, S. E.; Huang, D.; Ponomarev, M.; Cramer, W. A.; Smith, J. L. *Protein Sci.* **1996**, *5* (6), 1081–1092.
(16) Mogi, T.; Saiki, K.; Anraku, Y. *Mol. Microbiol.* **1994**, *14* (3), 391–398.
(17) Vainshtein, B. K.; Melik-Adamyan, W. R.; Barynin, V. V.; Vagin, A. A.; Grebenko, A. I.; Borisov, V. V.; Bartels, K. S.; Fita, I.; Rossmann, M. G. *J. Mol. Biol.* **1986**, *188* (1), 49–61.
(18) Igarashi, N.; Moriyama, H.; Fujiwara, T.; Fukumori, Y.; Tanaka, N. *Nat. Struct. Mol. Biol.* **1997**, *4* (4), 276–284.
(19) Crane, B. R.; Siegel, L. M.; Getzoff, E. D. *Science* **1995**, *270* (5233), 59–67.
(20) Lemberg, R.; Falk, J. E. *Biochem. J.* **1951**, *49* (5), 674–683.
(21) Lombardi, A.; Nastri, F.; Pavone, V. *Chem. Rev.* **2001**, *101* (10), 3165–3189.
(22) Smith, L. J.; Kahraman, A.; Thornton, J. M. *Proteins Struct. Funct. Bioinforma.* **2010**, *78* (10), 2349–2368.
(23) Lanzilotta, W. N.; Schuller, D. J.; Thorsteinsson, M. V.; Kerby, R. L.; Roberts, G. P.; Poulos, T. L. *Nat. Struct. Mol. Biol.* **2000**, *7* (10), 876–880.
(24) Fülöp, V.; Moir, J. W. B.; Ferguson, S. J.; Hajdu, J. *Cell* **1995**, *81* (3), 369–377.

(25) Dickerson, R. E.; Takano, T.; Eisenberg, D.; Kallai, O. B.; Samson, L.; Cooper, A.; Margoliash, E. *J. Biol. Chem.* **1971**, *246* (5), 1511–1535.
(26) Willies, S. C.; Isupov, M. N.; Garman, E. F.; Littlechild, J. A. *JBIC J. Biol. Inorg. Chem.* **2009**, *14* (2), 201–207.
(27) Poulos, T. L.; Finzel, B. C.; Howard, A. J. *Biochemistry (Mosc.)* **1986**, *25* (18), 5314–5322.
(28) Li, T.; Bonkovsky, H. L.; Guo, J. *BMC Struct. Biol.* **2011**, *11*, 13.
(29) Bowman, S. E.; Bren, K. L. *Nat. Prod. Rep.* **2008**, *25* (6), 1118–1130.
(30) Welinder, K. G. *Curr. Opin. Struct. Biol.* **1992**, *2* (3), 388–393.
(31) Sibbett, S. S.; Hurst, J. K. *Biochemistry (Mosc.)* **1984**, *23* (13), 3007–3013.
(32) Cramer, S. P.; Dawson, J. H.; Hodgson, K. O.; Hager, L. P. *J. Am. Chem. Soc.* **1978**, *100* (23), 7282–7290.
(33) Welinder, K. G. *FEBS Lett.* **1976**, *72* (1), 19–23.
(34) Veitch, N. C. *Phytochemistry* **2004**, *65* (3), 249–259.
(35) Gajhede, M.; Schuller, D. J.; Henriksen, A.; Smith, A. T.; Poulos, T. L. *Nat. Struct. Biol.* **1997**, *4* (12), 1032–1038.
(36) Poulos, T. L.; Kraut, J. *J. Biol. Chem.* **1980**, *255* (17), 8199–8205.
(37) Dunford, H. B.; others. *Peroxidases Chem. Biol.* **1991**, *2*, 1–24.
(38) Veitch, N. C.; Smith, A. T. In *Advances in Inorganic Chemistry*; Elsevier, 2000; Vol. 51, pp 107–162.
(39) Everse, J. *Free Radic. Biol. Med.* **1998**, *24* (7), 1338–1346.
(40) Finzel, B. C.; Poulos, T. L.; Kraut, J. *J. Biol. Chem.* **1984**, *259* (21), 13027–13036.
(41) Rodriguez-Lopez, J. N.; Smith, A. T.; Thorneley, R. N. *J. Biol. Chem.* **1996**, *271* (8), 4023–4030.
(42) Howes, B. D.; Rodriguez-Lopez, J. N.; Smith, A. T.; Smulevich, G. *Biochemistry (Mosc.)* **1997**, *36* (6), 1532–1543.
(43) Savenkova, M. I.; Kuo, J. M.; Ortiz de Montellano, P. R. *Biochemistry (Mosc.)* **1998**, *37* (30), 10828–10836.
(44) Berglund, G. I.; Carlsson, G. H.; Smith, A. T.; Szöke, H.; Henriksen, A.; Hajdu, J. *Nature* **2002**, *417* (6887), 463–468.
(45) Penning, T. M.; Jez, J. M. *Chem Rev* **2001**, *101* (10), 3027–3046.
(46) Lu, Y.; Yeung, N.; Sieracki, N.; Marshall, N. M. *Nature* **2009**, *460* (7257), 855–862.
(47) Lu, Y.; Berry, S. M.; Pfister, T. D. *Chem. Rev.* **2001**, *101* (10), 3047–3080.
(48) Lombardi, A.; Marasco, D.; Maglio, O.; Di Costanzo, L.; Nastri, F.; Pavone, V. *Proc. Natl. Acad. Sci.* **2000**, *97* (22), 11922–11927.
(49) Dauter, Z.; Sieker, L. C.; Wilson, K. S. *Acta Crystallogr. B* **1992**, *48 ( Pt 1)*, 42–59.

(50) Nastri, F.; Lombardi, A.; D'Andrea, L. D.; Sanseverino, M.; Maglio, O.; Pavone, V. *Biopolymers* **1998**, *47* (1), 5–22.
(51) Momenteau, M.; Reed, C. A. *Chem. Rev.* **1994**, *94* (3), 659–698.
(52) Mansuy, D. *Coord. Chem. Rev.* **1993**, *125* (1-2), 129–141.
(53) Meunier, B. *Chem. Rev.* **1992**, *92* (6), 1411–1456.
(54) Collman, J. P.; Gagne, R. R.; Reed, C.; Halbert, T. R.; Lang, G.; Robinson, W. T. *J. Am. Chem. Soc.* **1975**, *97* (6), 1427–1439.
(55) Traylor, T. G.; Chang, C. K.; Geibel, J.; Berzinis, A.; Mincey, T.; Cannon, J. *J. Am. Chem. Soc.* **1979**, *101* (22), 6716–6731.
(56) David, S.; James, B. R.; Dolphin, D.; Traylor, T. G.; Lopez, M. A. *J. Am. Chem. Soc.* **1994**, *116* (1), 6–14.
(57) Tetreau, C.; Lavalette, D.; Momenteau, M.; Fischer, J.; Weiss, R. *J. Am. Chem. Soc.* **1994**, *116* (26), 11840–11848.
(58) Mashiko, T.; Reed, C. A.; Haller, K. J.; Kastner, M. E.; Scheidt, W. R. *J. Am. Chem. Soc.* **1981**, *103* (19), 5758–5767.
(59) Wuenschell, G. E.; Tetreau, C.; Lavalette, D.; Reed, C. A. *J. Am. Chem. Soc.* **1992**, *114* (9), 3346–3355.
(60) Collman, J. P.; Brauman, J. I.; Fitzgerald, J. P.; Hampton, P. D.; Naruta, Y.; Sparapany, J. W.; Ibers, J. A. *J. Am. Chem. Soc.* **1988**, *110* (11), 3477–3486.
(61) Traylor, T. G. *Acc. Chem. Res.* **1981**, *14* (4), 102–109.
(62) DeGrado, W. F.; Summa, C. M.; Pavone, V.; Nastri, F.; Lombardi, A. *Annu. Rev. Biochem.* **1999**, *68* (1), 779–819.
(63) Regan, L. *Trends Biochem. Sci.* **1995**, *20* (7), 280–285.
(64) Lu, Y.; Valentine, J. S. *Curr. Opin. Struct. Biol.* **1997**, *7* (4), 495–500.
(65) Baltzer, L. In *Implementation and Redesign of Catalytic Function in Biopolymers*; Schmidtchen, P. D. F. P., Baltzer, L., Chamberlin, A. R., McDonnell, K. A., Famulok, M., Gilmore, M. A., Imperiali, B., Jenne, A., Shogren-Knaak, M., Steward, L. E., Eds.; Springer Berlin Heidelberg, 1999; pp 39–76.
(66) Richardson, J. S.; Richardson, D. C.; Tweedy, N. B.; Gernert, K. M.; Quinn, T. P.; Hecht, M. H.; Erickson, B. W.; Yan, Y.; McClain, R. D.; Donlan, M. E. *Biophys. J.* **1992**, *63* (5), 1185–1209.
(67) Bryson, J. W.; Betz, S. F.; Lu, H. S.; Suich, D. J.; Zhou, H. X.; O'Neil, K. T.; DeGrado, W. F. *Science* **1995**, *270* (5238), 935–941.
(68) Betz, S. F.; Raleigh, D. P.; DeGrado, W. F. *Curr. Opin. Struct. Biol.* **1993**, *3* (4), 601–610.
(69) Tuchscherer, G.; Scheibler, L.; Dumy, P.; Mutter, M. *Biopolymers* **1998**, *47* (1), 63–73.
(70) Street, A. G.; Mayo, S. L. *Structure* **1999**, *7* (5), R105–R109.
(71) Desjarlais, J. R.; Handel, T. M. *Protein Sci.* **1995**, *4* (10), 2006–2018.

(72) Desjarlais, J. R.; Clarke, N. D. *Curr. Opin. Struct. Biol.* **1998**, *8* (4), 471–475.
(73) Tuppy, H.; Paléus, S.; Tuppy, H.; Virtanen, A. I. *Acta Chem. Scand.* **1955**, *9*, 353–364.
(74) Paléus, S.; Ehrenberg, A.; Tuppy, H.; Virtanen, A. I. *Acta Chem. Scand.* **1955**, *9*, 365–374.
(75) Bushnell, G. W.; Louie, G. V.; Brayer, G. D. *J. Mol. Biol.* **1990**, *214* (2), 585–595.
(76) Marques, H. M. *Dalton Trans.* **2007**, No. 39, 4371.
(77) Casella, L.; Gullotti, M.; De Gioia, L.; Monzani, E.; Chillemi, F. *J. Chem. Soc. Dalton Trans.* **1991**, No. 11, 2945.
(78) Casella, L.; Gullotti, M.; De Gioia, L.; Bartesaghi, R.; Chillemi, F. *J. Chem. Soc. Dalton Trans.* **1993**, No. 14, 2233.
(79) Casella, L.; Monzani, E.; Fantucci, P.; Gullotti, M.; De Gioia, L.; Strini, A.; Chillemi, F. *Inorg. Chem.* **1996**, *35* (2), 439–444.
(80) Monzani, E.; Linati, L.; Casella, L.; De Gioia, L.; Favretto, M.; Gullotti, M.; Chillemi, F. *Inorganica Chim. Acta* **1998**, *273* (1), 339–345.
(81) Franceschi, F.; Gullotti, M.; Monzani, E.; Casella, L.; Papaefthymiou, V. *Chem. Commun.* **1996**, No. 14, 1645–1646.
(82) Monzani, E.; Casella, L.; Gullotti, M.; Panigada, N.; Franceschi, F.; Papaefthymiou, V. In *Journal of molecular catalysis. A, Chemical*; Elsevier, 1997; Vol. 117, pp 199–204.
(83) Benson, D. R.; Hart, B. R.; Zhu, X.; Doughty, M. B. *J. Am. Chem. Soc.* **1995**, *117* (33), 8502–8510.
(84) Arnold, P. A.; Benson, D. R.; Brink, D. J.; Hendrich, M. P.; Jas, G. S.; Kennedy, M. L.; Petasis, D. T.; Wang, M. *Inorg. Chem.* **1997**, *36* (23), 5306–5315.
(85) Williamson, D. A.; Benson, D. R. *Chem. Commun.* **1998**, No. 9, 961–962.
(86) Liu, D.; Williamson, D. A.; Kennedy, M. L.; Williams, T. D.; Morton, M. M.; Benson, D. R. *J. Am. Chem. Soc.* **1999**, *121* (50), 11798–11812.
(87) Mihara, H.; Haruta, Y.; Sakamoto, S.; Nishino, N.; Aoyagi, H. *Chem. Lett.* **1996**, No. 1, 1–2.
(88) Obataya, I.; Kotaki, T.; Sakamoto, S.; Ueno, A.; Mihara, H. *Bioorg. Med. Chem. Lett.* **2000**, *10* (24), 2719–2722.
(89) Faiella, M.; Maglio, O.; Nastri, F.; Lombardi, A.; Lista, L.; Hagen, W. R.; Pavone, V. *Chem.- Eur. J.* **2012**, *18* (50), 15960–15971.
(90) Nastri, F.; Lombardi, A.; Morelli, G.; Maglio, O.; D'Auria, G.; Pedone, C.; Pavone, V. *Chem. - Eur. J.* **1997**, *3* (3), 340–349.
(91) Nastri, F.; Lombardi, A.; Morelli, G.; Pedone, C.; Pavone, V.; Chottard, G.; Battioni, P.; Mansuy, D. *J. Biol. Inorg. Chem.* **1998**, *3* (6), 671–681.

(92) D'Auria, G.; Maglio, O.; Nastri, F.; Lombardi, A.; Mazzeo, M.; Morelli, G.; Paolillo, L.; Pedone, C.; Pavone, V. *Chem. - Eur. J.* **1997**, *3* (3), 350–362.
(93) Lombardi, A.; Nastri, F.; Sanseverino, M.; Maglio, O.; Pedone, C.; Pavone, V. *Inorganica Chim. Acta* **1998**, *275-276*, 301–313.
(94) Lombardi, A.; Nastri, F.; Marasco, D.; Maglio, O.; De Sanctis, G.; Sinibaldi, F.; Santucci, R.; Coletta, M.; Pavone, V. *Chem. - Eur. J.* **2003**, *9* (22), 5643–5654.
(95) Geremia, S.; Di Costanzo, L.; Randaccio, L.; Lombardi, A.; Pavone, V.; Campagnolo, M. *Acta Cryst* **2002**, *58*, C277.
(96) Costanzo, L.; Geremia, S.; Randaccio, L.; Nastri, F.; Maglio, O.; Lombardi, A.; Pavone, V. *JBIC J. Biol. Inorg. Chem.* **2004**, *9* (8), 1017–1027.
(97) Nastri, F.; Lista, L.; Ringhieri, P.; Vitale, R.; Faiella, M.; Andreozzi, C.; Travascio, P.; Maglio, O.; Lombardi, A.; Pavone, V. *Chem. - Eur. J.* **2011**, *17* (16), 4444–4453.
(98) Vitale, R.; Lista, L.; Lau-Truong, S.; Tucker, R. T.; Brett, M. J.; Limoges, B.; Pavone, V.; Lombardi, A.; Balland, V. *Chem. Commun.* **2014**, *50* (15), 1894–1896.
(99) Vitale, R. **2013**. Ph.D. Thesis
(100) Vitale, R.; Lista, L.; Cerrone, C.; Caserta, G.; Chino, M.; Maglio, O.; Nastri, F.; Pavone, V.; Lombardi, A. *Org Biomol Chem* **2015**. DOI:10.1039/c5ob00257e

# Chapter II
# Results and discussion

## 2.1 The new Mimochrome VI*a* generation: design and synthesis

The new developed Mimochromes generation has been designed with the aim of introducing some structural constraints that should stabilize the three-dimensional sandwich structure, typical of Mimochromes, while preserving or enhancing functionality.

As described above, recently the role of the *inter*-chain ion pairs in Mimochrome VI model has been explored, designing a new family of analogues containing point amino acid substitutions. In particular, by individually replacing Glu2 and Arg10 on both peptide chains with a Leu residue, four analogues were obtained, which have been screened for their peroxidase-like activity.[1] The best catalytic performances were obtain for Glu2Leu(*TD*)-Mimochrome VI, allowing us to hypothesize a catalytic role of Arg10 on the decapeptide chain, whose side chain may approach the heme, contributing to stabilize Compound I and helping ligand binding, similarly to the conserved distal arginine (Arg38) in the Horseradish Peroxidase (HRP).

Starting form this point, we chose to conserve the Glu2Leu substitution on the tetradecapeptide chain, interrupting an *inter*-chain ion pair interaction in Mimochrome VI model (Glu2(*TD*)-Arg10(*D*)). To compensate for the destabilization caused by this

substitution, some structural constrains were introduced. Specifically, substitutions were introduced on the decapeptide chain, since it most likely experiences higher conformational freedom, respect to the tetradecapeptide chain, due to the lack of the coordinating histidine, that firmly anchors the tetradecapeptide chain on the heme. The α-aminoisobutyric acid (Aib, single letter code: U), was introduced in 3 and 7 positions of the decapeptide chain, obtaining Gln3,Ser7Aib(*D*)Glu2Leu(*TD*)-Mimochrome VI, named Mimochrome VI*a*.

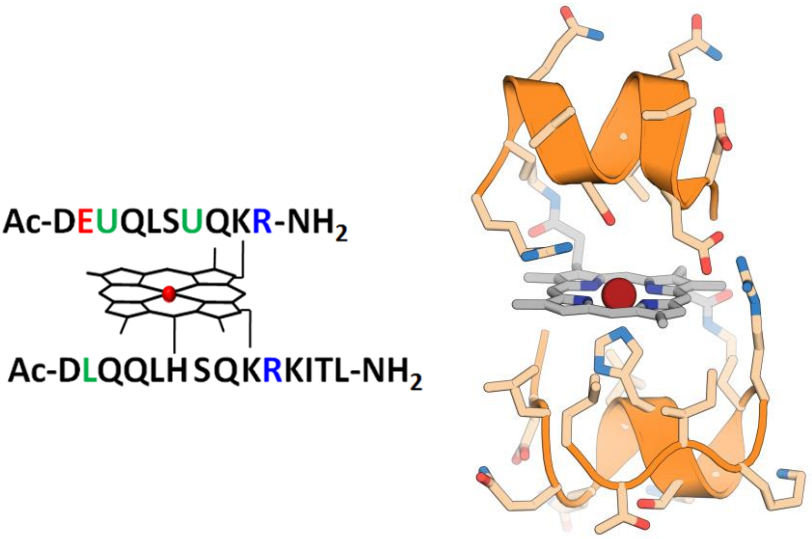


**Figure 23** Primary sequence and molecular model of $Fe^{III}$-Mimochrome VI*a*. Amino acid substitutions with respect to $Fe^{III}$-Mimochrome VI are in green, negatively charged residues are in red and positively charged residues are in blue.

The α-aminoisobutyric acid, or 2-amino-2-methylpropanoic acid, is a natural, non-coded amino acid, with a very high helical propensity, commonly found in peptides produced by microbes.[2] The replacement of the

hydrogen atoms with methyl groups at the Cα of the glycine produces sever restrictions on its conformational freedom: for Aib-containing peptides it is strongly favored the formation of α-, $3_{10}$- or mixed α-/$3_{10}$-helix secondary structures (Figure 24). Moreover, it has been shown that the equilibrium between the α- and $3_{10}$-helix in Aib-containing peptides is strongly influenced by changes in several parameters, mainly including the peptide length and the Aib content.[3] Several studies have shown that Aib oligomers form exclusively $3_{10}$-helices. On the contrary, if the Aib content does not exceed 50%, the $3_{10}$-helix is preferred for shorter peptides (number of residues, n, 8 or less), whereas a α-helix is observed for longer peptides (n= 9-20).[4,5]

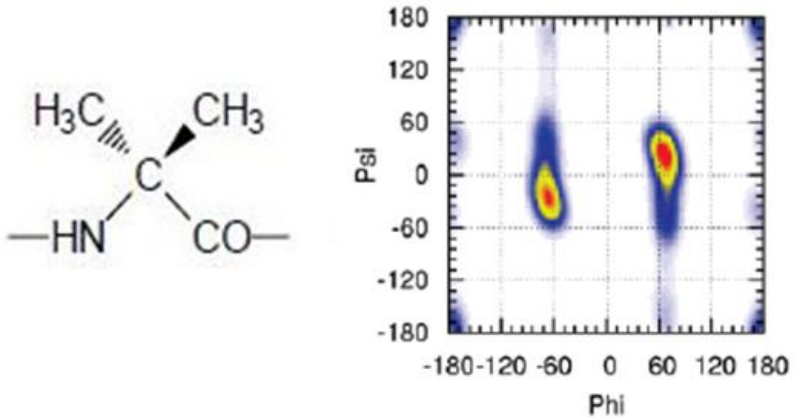


**Figure 24** On the left, molecular structure of the Aib residue. On the right, Ramachandran plot of a Aib containing peptide: red indicates the highest percentage of the population, and white indicates that a region is not populated.

In the next stage of design, a systematic evaluation of the linker length between the porphyrin and the decapeptide chain was carried out. In particular, to further

stabilize the sandwich structure, the linker length was progressively decreased. Therefore, Lys (2,6-Diaminohexanoic acid) at position 9 on the decapeptide chain was substituted with Orn (2,5-Diaminopentanoic acid) and with Dab (2,4-Diaminobutyric acid), whose side chains contain, respectively, one and two methylenic group less than lysine side chain. In this way, Gln3,Ser7AibLys9Orn(*D*)Glu2Leu(*TD*)-Mimochrome VI and Gln3,Ser7AibLys9Dab(*D*)Glu2Leu(*TD*)-Mimochrome VI were obtained, named, respectively, Lys9Orn(*D*)-Mimochrome VI*a* and Lys9Dab(*D*)-Mimochrome VI*a*.

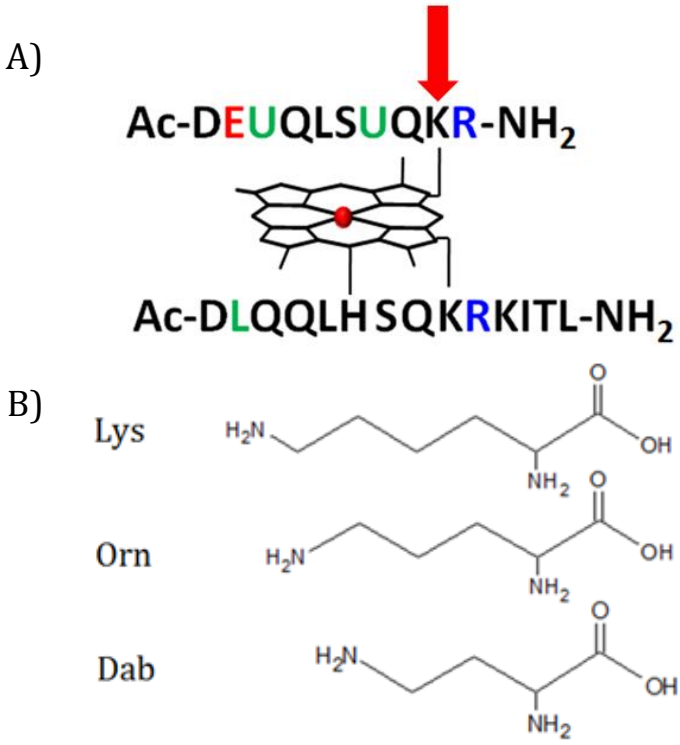


**Figure 25** A) Schematic structure of the new developed analogue, $Fe^{III}$-Mimochrome VI*a*, highlighting Lys9 residue on the decapeptide chain. (B) Molecular structure of Lys, Orn and Dab residues.

Mimochrome VI*a* and its analogues were synthesized using the strategy previously adopted for other Mimochromes,[6] with some differences (for further details see Chapter IV: Materials and methods).

Peptide chains were synthesized in solid phase, by using 9-fluorenylmethoxycarbonyl (Fmoc) protection strategy. A super acid labile resin was used in order to obtain fully protected peptides, apart from Lys9, Orn9 and Dab9 residues on the decapeptide chain and Lys9 on the tetradecapeptide chain. For Lys side chain, the Mmt protecting group was chosen; Orn and Dab were used with Mtt protecting group on their side chain amino functions.

The selective removal of Mmt ((4-methoxyphenyl)diphenylmethyl) protecting group from residues on the two chains, allowed to obtain the fully protected peptides, except from Lys9. Thanks to this strategy, it is possible to selectively couple peptides to the deuteroporphyrin IX (DPIX).

For Lys9Orn(*D*)-Mimochrome VI*a* and Lys9Dab(*D*)-Mimochrome VI*a*, the selective removal of Mtt ((4-methylphenyl)diphenylmethyl) protecting group allowed the coupling of the decapeptide chains to the DPIX.

In order to optimize the mono-substituted porphyrin formation (*D*-DPIX) and minimize the undesired bi-substituted product (*D*-DPIX-*D*), the decapeptide was slowly added to the solution containing an excess of deuteroporphyrin IX.

Interestingly, the new developed Mimochrome mono-substituted derivatives show a chromatogram profile evidencing two peaks of similar intensities, with the same

UV-Vis spectrum. The ESI-MS analysis on the two peaks reveals that they have the same mass spectra, whose values are in agreement with the mass values expected for the mono-substituted compound. The analytical chromatograms, the UV-Vis spectra and the ESI-MS spectra of Dab9Lys(*D*)-Mimochrome VI*a* mono-substituted derivative are reported in Figure 26-28, as an example. Similar behaviors were observed for the other two mono-substituted porphyrin derivatives.

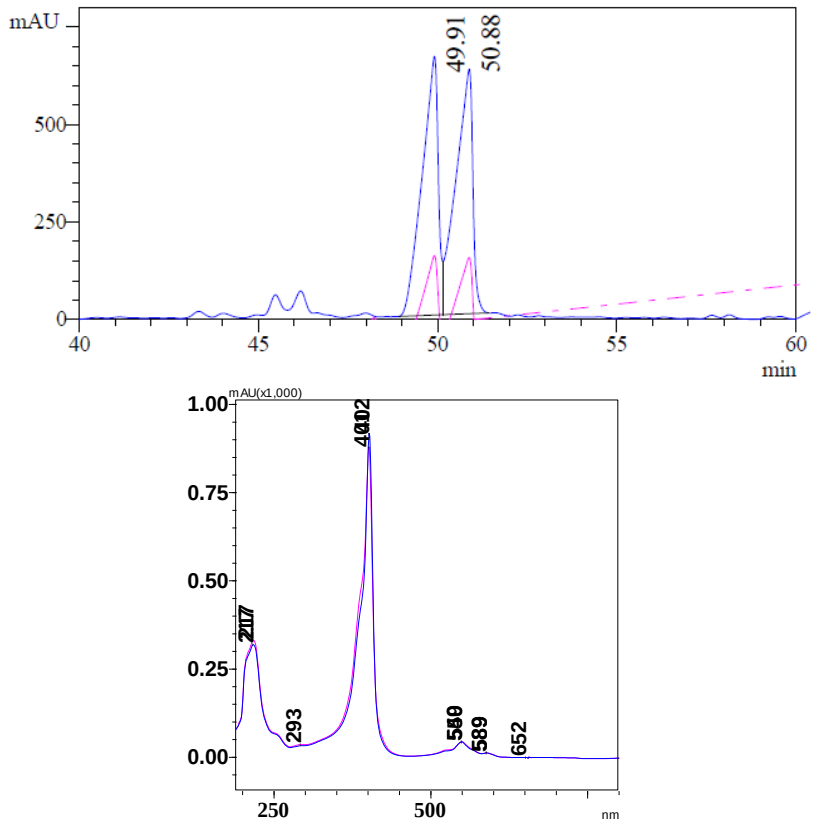


**Figure 26** Top: RP-HPLC profile of Dab9Lys(*D*)-DPIX mono-substituted derivative; the peaks were detected at λ= 210 nm (in magenta), and 400nm (in blue). Bottom: overlap of the UV-Vis spectra of the two peaks.

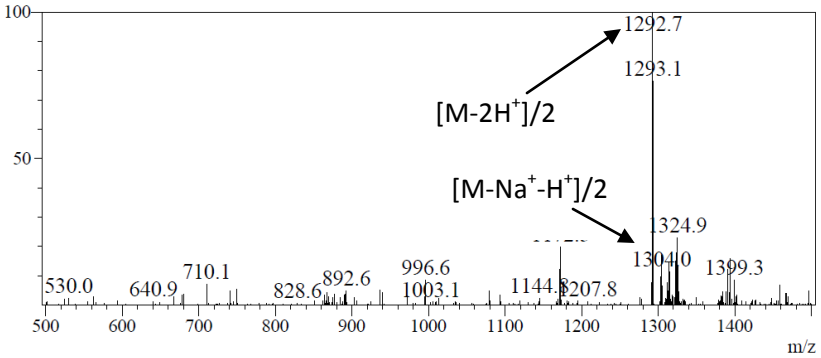


**Figure 27** ESI-MS spectrum of the peak at $R_t$=49.91 min. The spectrum is in agreement with the expected mass (calculated mass: 2584.04 Da; experimental mass: 2583.7 ± 0.5 Da).

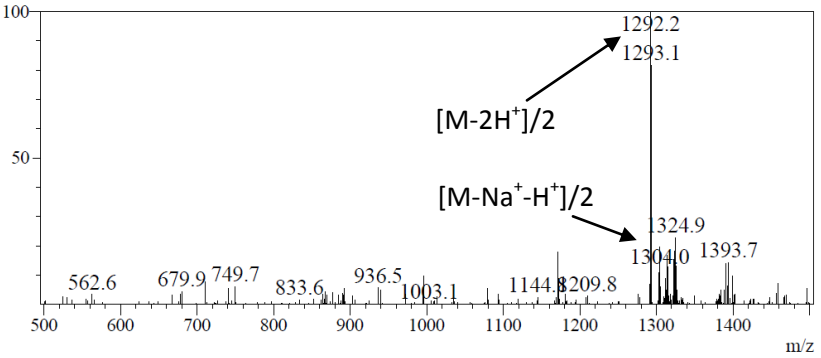


**Figure 28** ESI-MS spectrum of the peak at $R_t$=50.88 min. The spectrum is in agreement with the expected mass (calculated mass: 2584.04 Da; experimental mass: 2583.2 ± 0.9 Da).

The two peaks were separated by HPLC on a small scale, and analyzed by NMR, proving that they correspond to two constitutional isomers (data not shown). In fact, covalent modification of the DPIX at one of the propionic acid groups gives an equimolar mixture of the isomers substituted at 2 or 18 positions of the DPIX ring (Figure 29).

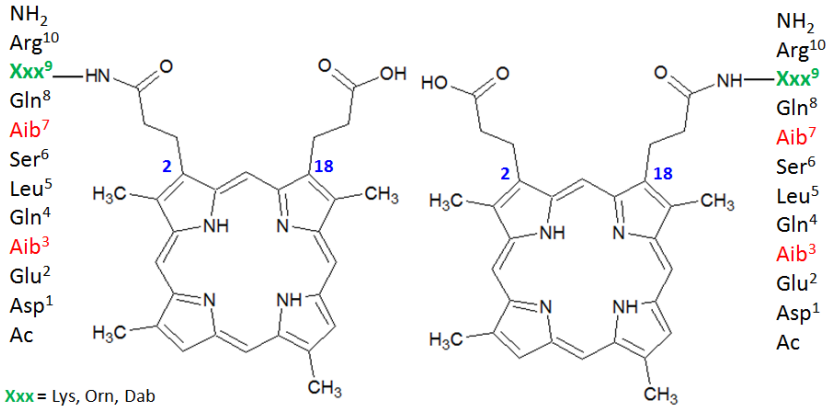


**Figure 29** Molecular structures of the mono-substituted derivative of Mimochrome VI*a* and its analogues.

The presence of two peaks in the HPLC analysis of the mono-substituted derivative was never observed in the previous Mimochromes compounds. Probably, the presence of the two Aib residues allowing the observed separation, imparts different structural properties.

Attempts to separate the two peaks by direct phase flash chromatography were not successful, due to their similar $R_f$. On the other hand, reversed phase chromatography on a preparative scale cannot be performed, due to the acidic elution conditions, which remove the side chain protecting groups.

Therefore, the solution containing both mono-substituted derivatives was then used to perform the coupling with the tetradecapeptide. Once obtained the bi-substituted products, the remaining protecting groups were removed from both peptide chains. Purification by preparative RP-HPLC succeeded in separating the two regioisomers, named isomer 1 and 2.

For each new analogue, iron was individually inserted, following the acetate method, on the two isomers. For a more detailed description of protocols and synthetic results, please refer to Chapter IV: Materials and methods.
The chromatographic and mass data of all the analyzed molecules are reported in Table 4.

| Enzyme | $R_t$ (min) | M.W.$_{calc}$ (Da) | M.W.$_{exp}$ (Da) |
|---|---|---|---|
| Mimochrome VI*a* apo form isomer 1 | 53.74 | 3437.83 | 3437.9 ± 0.6 |
| Mimochrome VI*a* apo form isomer 2 | 54.18 | 3437.83 | 3438.4 ± 0.7 |
| Lys9Orn(*D*)-Mimochrome VI*a* apo form isomer 1 | 53.30 | 3423.81 | 3422.8 ± 1.5 |
| Lys9Orn(*D*)-Mimochrome VI*a* apo form isomer 2 | 53.54 | 3423.81 | 3422.8 ± 1.3 |
| Lys9Dab(*D*)-Mimochrome VI*a* apo form isomer 1 | 53.02 | 3409.78 | 3409.1 ± 0.8 |
| Lys9Dab(*D*)-Mimochrome VI*a* apo form isomer 2 | 53.34 | 3409.78 | 3409.5 ± 0.4 |
| $Fe^{III}$-Mimochrome VI*a* isomer 1 | 50.95 | 3491.66 | 3490.6 ± 1.2 |
| $Fe^{III}$-Mimochrome VI*a* isomer 2 | 52.46 | 3491.66 | 3491.1 ± 1.0 |
| $Fe^{III}$-Lys9Orn(*D*)-Mimochrome VI*a* isomer 1 | 49.52 | 3477.63 | 3477.4 ± 0.4 |
| $Fe^{III}$-Lys9Orn(*D*)-Mimochrome VI*a* isomer 2 | 49.75 | 3477.63 | 3477.0 ± 0.8 |
| $Fe^{III}$-Lys9Dab(*D*)-Mimochrome VI*a* isomer 1 | 49.27 | 3463.61 | 3463.3 ± 0.7 |
| $Fe^{III}$-Lys9Dab(*D*)-Mimochrome VI*a* isomer 2 | 48.73 | 3463.61 | 3463.3 ± 0.7 |

**Table 4** Chromatographic data and mass data of all the synthesized molecules. A Vydac C18 column (4.6 mm·150 mm; 5 μm), was used in the LC-MS analysis, eluted with $H_2O$/0.1% TFA (v/v) (solvent A) and acetonitrile/0.1% TFA (v/v) (solvent B) linear gradient, from 10% to 50% B over 60 min, at 0.5 mL·min$^{-1}$ flow rate.

## 2.2 Catalytic screening of $Fe^{III}$-Mimochrome VI*a* and its analogues

The catalytic properties of the new developed Mimochromes were evaluated to determine the effects of point amino acid substitutions on function.

In particular, the peroxidase-like activity towards the reducing substrate ABTS (2,2'-azino-bis(3-ethylbenzthiazoline-6-sulphonic acid)) was assayed. ABTS is a compound of choice for the assay of peroxidase activity,[7] since it can be efficiently oxidized in a mono cationic radical form ($ABTS^{+\cdot}$), which exhibits a brilliant green color ($\lambda_{max}$ = 660 nm) and therefore its formation can be easily detected by spectrophotometric measurements.

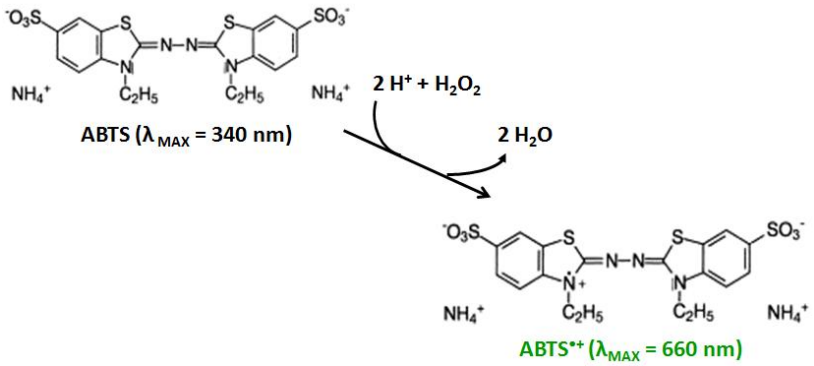


**Figure 30** Oxidation reaction of ABTS by $H_2O_2$.

The kinetic parameters were determined by analysing, at fixed catalyst concentration, the dependence of the reaction rate on the concentration of one substrate (as example, ABTS) at saturating concentration of the other

(as example, $H_2O_2$), and vice versa. The experimental data were fitted with a two substrate Michaelis-Menten kinetic equation:

$$v = \frac{[E]_0}{\frac{1}{k_{cat}} + \frac{K_m^{\ A}}{k_{cat}[A]} + \frac{K_m^{\ B}}{k_{cat}[B]}} \qquad (\alpha)$$

where:

- $[E]_0$ is the enzyme concentration at the initial time ($t_0$), which is supposed to be constant and not inactivated;
- $k_{cat}$ (also called *turnover number*) is the catalytic constant and denotes the maximum number of enzymatic reactions catalysed per second;
- [A] and [B] represent the ABTS and $H_2O_2$ concentrations, respectively;
- $K_m^A$ and $K_m^B$ are the Michaelis-Menten constants for ABTS and $H_2O_2$, respectively. The Michaelis-Menten constant is the substrate concentration at which the reaction rate is half of $v_{max}$ and represents the enzyme apparent affinity for the substrate;

The analysis of the experimental kinetic data by Michaelis-Menten fitting provides the following catalytic parameters:

- $k_{cat}$ (above discussed);
- $K_m^{ABTS}$ and $K_m^{H_2O_2}$ (above discussed);

- $k_{cat}/K_m^{ABTS}$ and $k_{cat}/K_m^{H_2O_2}$, which are measures of the catalytic efficiency.

$Fe^{III}$-Mimochrome VI*a* and its analogues were screened for their peroxidase-like activity, in the same conditions used for $Fe^{III}$-Mimochrome VI and its first generation of analogues (50 mM phosphate buffer pH 6.5, 50% TFE (v/v)). The enzyme concentration was fixed at $2.0 \cdot 10^{-8}$ M. To study the dependence towards the oxidizing substrate, ABTS concentration was fixed ($1.0 \cdot 10^{-4}$ M), whereas $H_2O_2$ concentration was varied in the range of $1.0 \cdot 10^{-4}$-$1.0 \cdot 10^{-1}$ M; on the contrary, to study the dependence towards the reducing substrate, $H_2O_2$ concentration was fixed ($1.0 \cdot 10^{-2}$ M), whereas ABTS concentration was varied in the range $5.0 \cdot 10^{-6}$-$1.0 \cdot 10^{-4}$ M. All the new developed Mimochrome enzymes follow a two substrate Michaelis-Menten kinetic model, as evidenced by inspection of Figure 31-33.
The kinetic parameters obtained by fitting the experimental data with the equation (α) are reported in Table 5. The kinetic parameters of the parent molecule, $Fe^{III}$-Mimochrome VI, of the best catalyst of the previous generation of Mimochromes, $Fe^{III}$-E2L(*TD*)-MC6, and of the natural reference model, HRP, are also reported in the Table for comparison.

In a different experiment, the turnover number (T.O.N.) of $Fe^{III}$-Mimochrome VI*a* and its analogues was determined. The T.O.N. is defined as the number of moles of substrate that a mole of catalyst can convert before becoming inactivated. In order to assess the turnover

number of the new developed molecules, the peroxidase-like activity was studied at fixed ABTS ($1.0 \cdot 10^{-4}$ M) and $H_2O_2$ ($3.0 \cdot 10^{-3}$M) concentrations and at decreasing catalyst concentrations, in the range $2.0 \cdot 10^{-8}$ M – $9.0 \cdot 10^{-9}$ M (Figure 34). The red kinetic curves reported in Figure represent the minimum enzyme concentration at which it is still possible to oxidize all the ABTS molecules present in solution, which can be deduced by the achievement of the *plateau* of the $ABTS^{+\cdot}$ absorbance. These concentration values were used to calculate the TONs of all the new developed analogues, which are reported in Table 5, and compared with those of $Fe^{III}$-Mimochrome VI, $Fe^{III}$-E2L(*TD*)-MC6 and HRP.

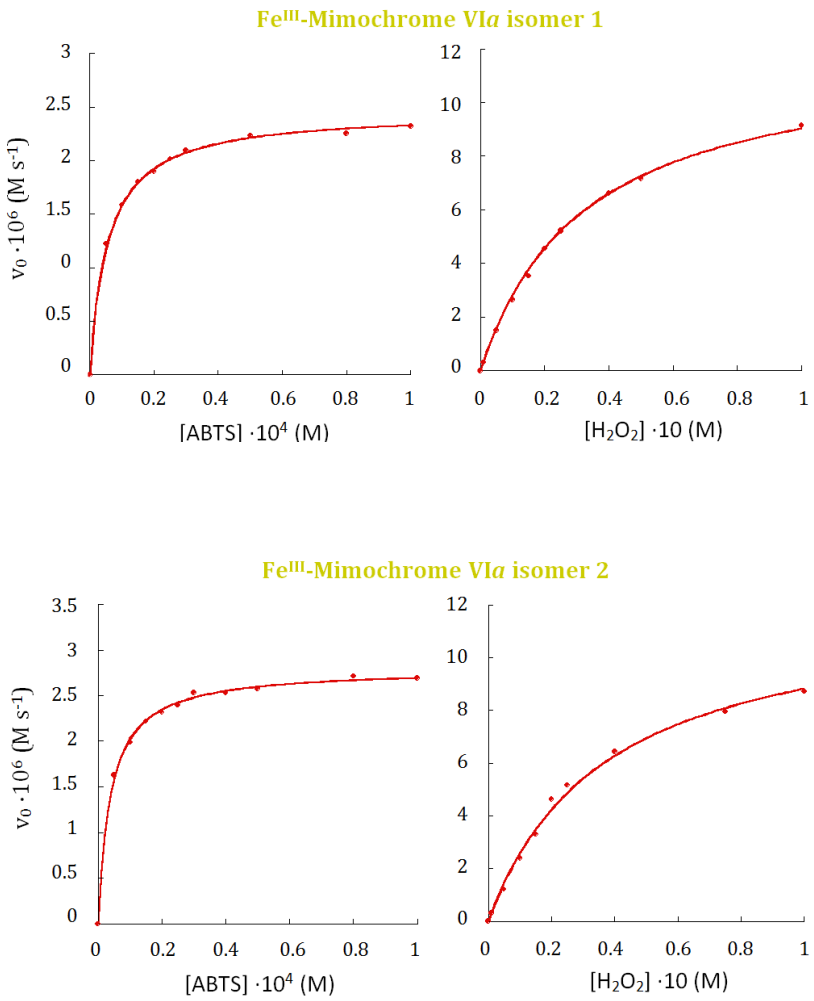


**Figure 31** Peroxidase-like activity of Fe$^{III}$–Mimochrome VI*a* isomer 1 and 2 in 50 mM phosphate buffer pH 6.5, 50% TFE (v/v). On the left, initial rate of ABTS oxidation at various ABTS concentrations (experimental condition: [$H_2O_2$]= $1.0 \cdot 10^{-2}$ M); on the right, initial rate of ABTS oxidation at various $H_2O_2$ concentrations (experimental condition: [ABTS]= $1.0 \cdot 10^{-4}$ M). The enzyme concentration is fixed at $2.0 \cdot 10^{-8}$ M.

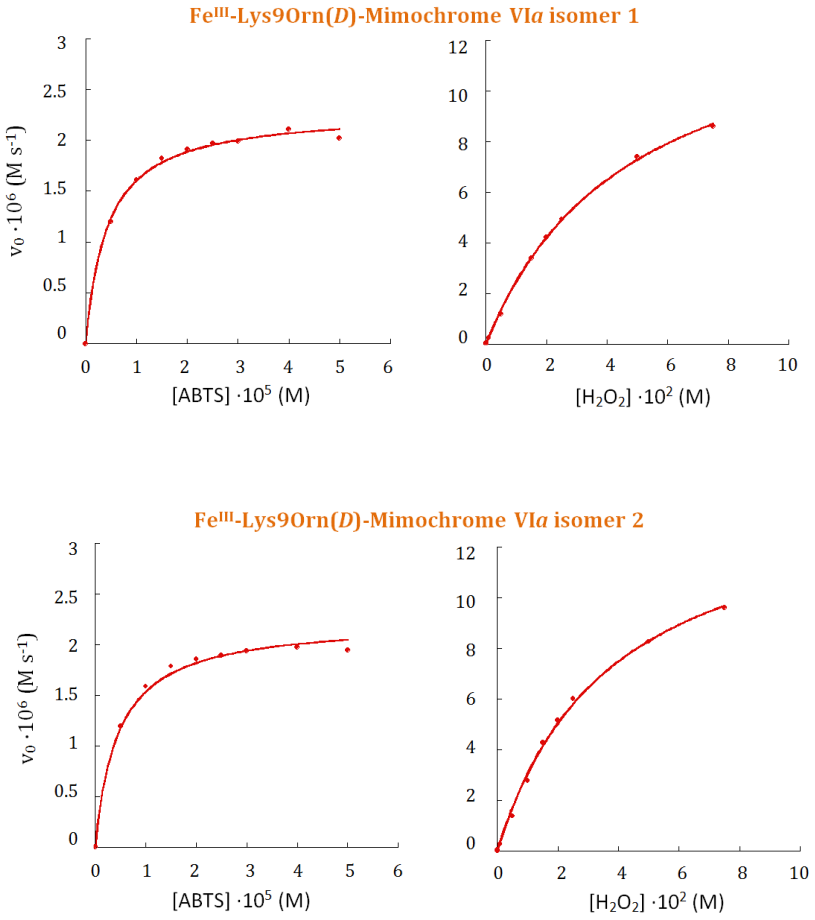


**Figure 32** Peroxidase-like activity of Fe$^{III}$–Lys9Orn(*D*)-Mimochrome VI*a* isomer 1 and 2 in 50 mM phosphate buffer pH 6.5, 50% TFE (v/v). On the left, initial rate of ABTS oxidation at various ABTS concentrations (experimental condition: [$H_2O_2$]= $1.0 \cdot 10^{-2}$ M); on the right, initial rate of ABTS oxidation at various $H_2O_2$ concentrations (experimental condition: [ABTS]= $1.0 \cdot 10^{-4}$ M). The enzyme concentration is fixed at $2.0 \cdot 10^{-8}$ M.

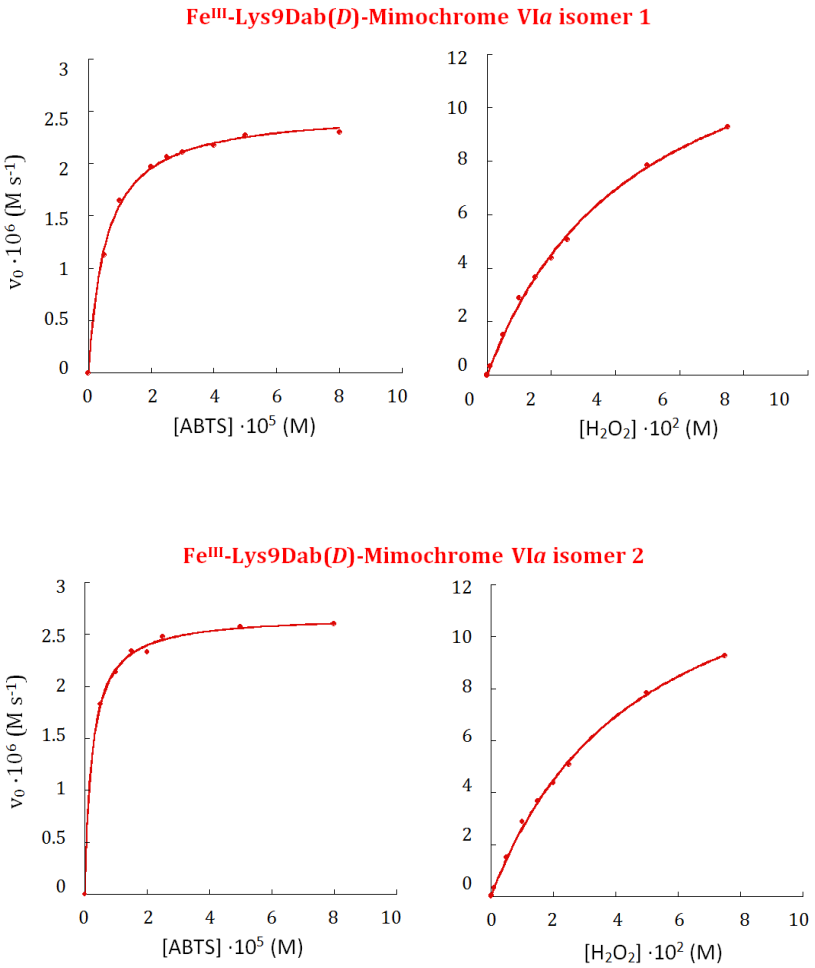


**Figure 33** Peroxidase-like activity of $Fe^{III}$–Lys9Dab(*D*)-Mimochrome VI*a* isomer 1 and 2 in 50 mM phosphate buffer pH 6.5, 50% TFE (v/v). On the left, initial rate of ABTS oxidation at various ABTS concentrations (experimental condition: [$H_2O_2$]= $1.0 \cdot 10^{-2}$ M); on the right, initial rate of ABTS oxidation at various $H_2O_2$ concentrations (experimental condition: [ABTS]= $1.0 \cdot 10^{-4}$ M). The enzyme concentration is fixed at $2.0 \cdot 10^{-8}$ M.

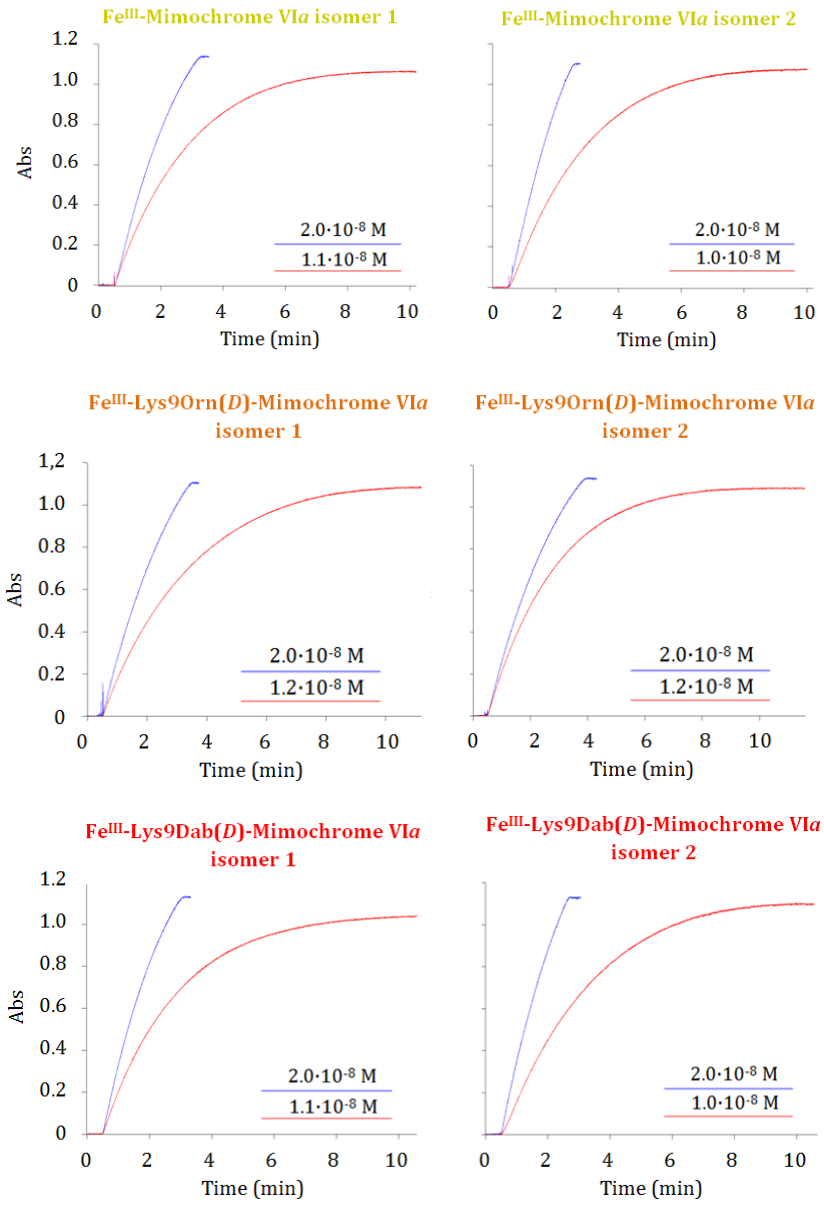


**Figure 34** T.O.N. of all the new developed Mimochromes. Progress curves for ABTS oxidation in the following experimental conditions: [ABTS]= $1.0 \cdot 10^{-4}$ M, [$H_2O_2$]= $3.0 \cdot 10^{-3}$ M at different catalyst concentration, in 50 mM phosphate buffer pH 6.5, 50% TFE (v/v).

| Enzyme | pH | $k_{cat}\cdot10^{-3}$ ($s^{-1}$) | $K_m^{H_2O_2}$ (mM) | $K_m^{ABTS}\cdot10^2$ (mM) | $k_{cat}/K_m^{H_2O_2}$ ($mM^{-1}\,s^{-1}$) | $k_{cat}/K_m^{ABTS}\cdot10^{-3}$ ($mM^{-1}\,s^{-1}$) | T.O.N.$\cdot10^{-3}$ |
|---|---|---|---|---|---|---|---|
| $Fe^{III}$-Mimochrome VI[a] | 6.5 | 0.37 ± 0.01 | 44 ± 2 | 8.4 ± 0.2 | 8.4 ± 0.5 | 4.4 ± 0.2 | 4.0 ± 0.2 |
| $Fe^{III}$-E2L(*TD*)-MC6[b] | 6.5 | 0.78 ± 0.06 | 31 ± 2 | 5.0 ± 0.4 | 25 ± 3 | 16 ± 2 | 5.9 ± 0.4 |
| $Fe^{III}$-Mimochrome VI*a* isomer 1 | 6.5 | 0.72 ± 0.04 | 41 ± 2 | 3.0 ± 0.3 | 17 ± 2 | 17 ± 3 | 9.1 ± 0.9 |
| $Fe^{III}$-Mimochrome VI*a* isomer 2 | 6.5 | 0.78 ± 0.02 | 46 ± 3 | 2.1 ± 0.2 | 17 ± 2 | 36 ± 4 | 10 ± 0.9 |
| $Fe^{III}$-Lys9Orn(*D*)-Mimochrome VI*a* isomer 1 | 6.5 | 0.96 ± 0.08 | 64 ± 7 | 3.5 ± 0.6 | 15 ± 3 | 27 ± 7 | 8.3 ± 0.8 |
| $Fe^{III}$- Lys9Orn(*D*)-Mimochrome VI*a* isomer 2 | 6.5 | 0.97 ± 0.09 | 50 ± 7 | 3.3 ± 0.6 | 19 ± 5 | 29 ± 8 | 8.3 ± 0.8 |
| $Fe^{III}$-Lys9Dab(*D*)-Mimochrome VI*a* isomer 1 | 6.5 | 1.1 ± 0.1 | 68 ± 8 | 4.9± 0.7 | 16 ± 3 | 22 ± 5 | 9.1 ± 0.9 |
| $Fe^{III}$- Lys9Dab(*D*)-Mimochrome VI*a* isomer 2 | 6.5 | 1.0 ± 0.1 | 58 ± 9 | 1.8 ± 0.3 | 17 ± 4 | 55 ± 15 | 10 ± 0.9 |
| HRP[b] | 4.6 | 6.2 ± 0.1 | 0.85 ± 0.01 | 107 ± 1 | (7.3±0.2)·$10^3$ | 5.8 ± 0.1 | 50 ± 3 |
| HRP[c] | 7.0 | (5.25±0.4)·$10^{-2}$ | (1.15±0.11)·$10^{-2}$ | (5.1±1.2)·$10^2$ | (4.6±0.5)·$10^3$ | (1.0 ± 0.3)·$10^{-2}$ | |

**Table 5** Steady-state kinetic parameters of all the new developed Mimochromes, compared with those of: the parent molecule, $Fe^{III}$-Mimochrome VI; the best catalyst of the previous generation of Mimochromes, $Fe^{III}$-E2L(*TD*)-MC6; and the natural reference model, HRP, at different pHs. (a) Data from reference 6. (b) Data from reference 1. (c) Data from reference 9.
8

## 2.2.1 Effect of pH on catalytic activity

First, the role of the pH on the peroxidase-like activity of $Fe^{III}$-Lys9Dab(*D*)-Mimochrome VI*a* isomer 1 and 2 was evaluated. At fixed ABTS, $H_2O_2$ and enzyme concentrations ($1.0 \cdot 10^{-4}$ M, $3.0 \cdot 10^{-3}$M and $2.0 \cdot 10^{-8}$ M, respectively) the initial rate of the oxidation reaction of ABTS was measured in 50 mM phosphate buffer, 50% TFE (v/v) at different pHs.

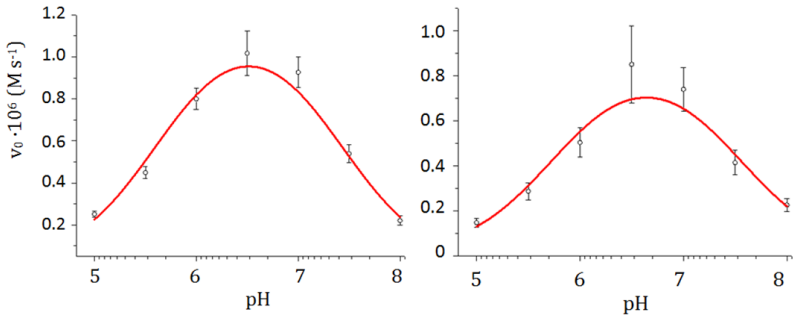


**Figure 35** Initial rates of the ABTS oxidation as a function of pH, for $Fe^{III}$-Lys9Dab(*D*)-Mimochrome VI*a* isomer 1 (left) and 2 (right). Experimental conditions: [ABTS]= $1.0 \cdot 10^{-4}$ M, [$H_2O_2$]= $3.0 \cdot 10^{-3}$ M, [enzyme]= $2.0 \cdot 10^{-8}$ M in 50 mM phosphate buffer, 50% TFE (v/v) at different pHs.

$Fe^{III}$-Lys9Dab(*D*)-Mimochrome VI*a* isomer 1 and 2 display the highest activity at pH 6.5 ± 0.1 and 6.6 ± 0.1, respectively. The parent molecule, $Fe^{III}$-Mimochrome VI, and all the molecules of the first generation of Mimochrome VI analogues exhibit the highest activity at the same pH (within the experimental error). This finding suggests that the amino acid mutation does not affect the pH at which the maximum activity is observed.

## 2.3 Spectroscopic characterization of $Fe^{III}$-Lys9Dab(*D*)-Mimochrome VI*a* isomer 1 and 2

$Fe^{III}$-Lys9Dab(*D*)-Mimochrome VI*a* isomer 1 and 2 were selected for a detailed spectroscopic characterization in order to gain insight into their structures. These molecules have been chosen on the basis of their highest $k_{cat}$ and T.O.N. values, which makes them the most promising catalysts of the new generation of Aib-containing Mimochromes.

### 2.3.1 Exploring the coordination properties: UV-Vis characterization

To explore the coordination properties, an UV-Vis pH titration was performed in the range 2.0-9.0, in $H_2O$/TFE 50/50 (v/v) (Figure 36-37).

The titration was performed by using concentrated solutions of trifluoroacetic acid (TFA) and sodium hydroxide (NaOH), in a 1.0 cm path length cuvette. Data points were fitted to an equation describing the protonation state of the species involved in the pH-dependent equilibria.[1]

For $Fe^{III}$-Lys9Dab(*D*)-Mimochrome VI*a* isomer 1, one well-resolved transition with midpoint at pH 6.9 ± 0.1 was observed. It was not possible to determine the $pK_a$ in the pH range 2.0-5.0, because at pH 2.0 the *plateau* is still not reached (see Figure 36 b). The spectrum at this pH value can be attributed to a mixture of mainly high-spin *bis*-$H_2O$ and His-$H_2O$ ferric complexes.

At pH 5.0, the Soret bands is at 388 nm, the Q bands at 493 and 530 nm, and the charge-tranfer (CT) band at 618 nm: these observations are consistent with a His/$H_2O$ ferric ion axial coordination, predominantly in high spin state.[6,9] At pH around 8.0, the Soret band shifts to 389 nm, the Q band is observed as a shoulder at 514 nm; the main bands at 487 and 600 nm are attributed to the CT bands of the mainly high-spin ferric hydroxide complex.[10,11] These spectroscopic features suggest that the transition with midpoint at pH 6.93 corresponds to a ligand exchange from $H_2O$ to $OH^-$.

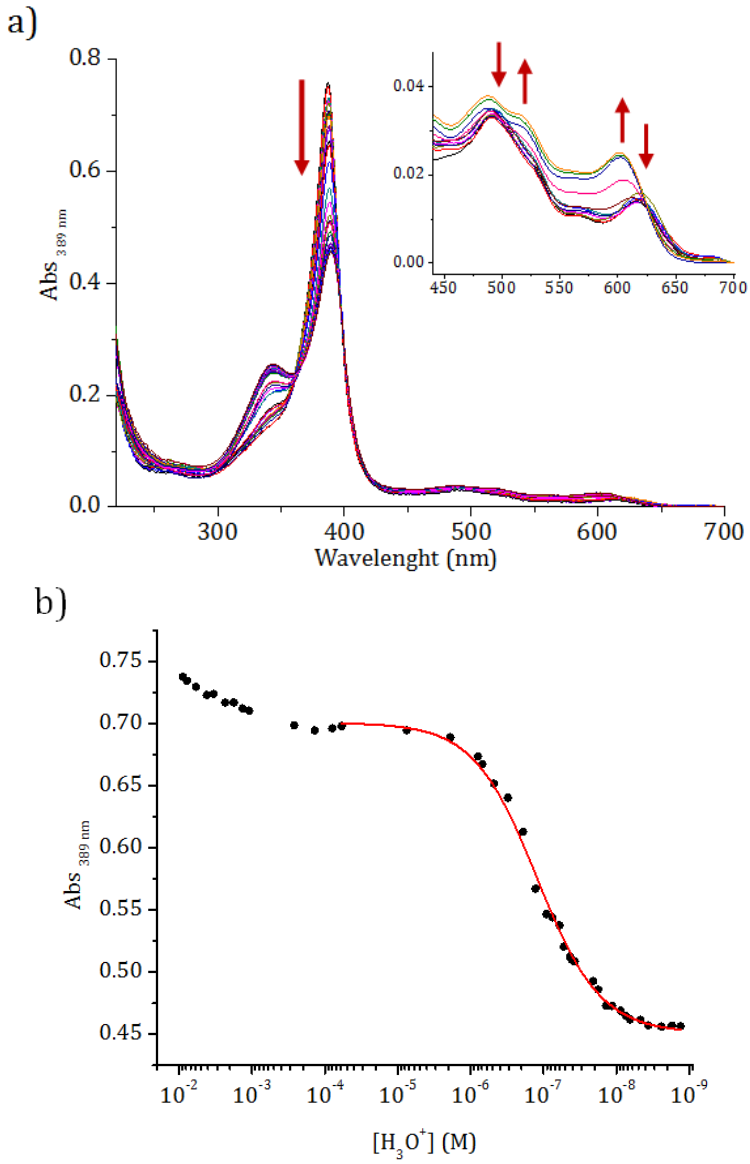


**Figure 36** a) UV-Vis spectra of $Fe^{III}$-Lys9Dab(*D*)-Mimochrome VI*a* isomer 1 ($5.0 \cdot 10^{-6}$ M) in $H_2O$/TFE, 50/50 (v/v) at various pHs (2.0–9.0). The arrows indicate the observed intensity changes of the Soret, Q and CT bands at increasing pHs. b) Plot of the absorbance at 389 nm as function of pH. The black dots are the experimental data, which were fitted with a one transition model (red line).

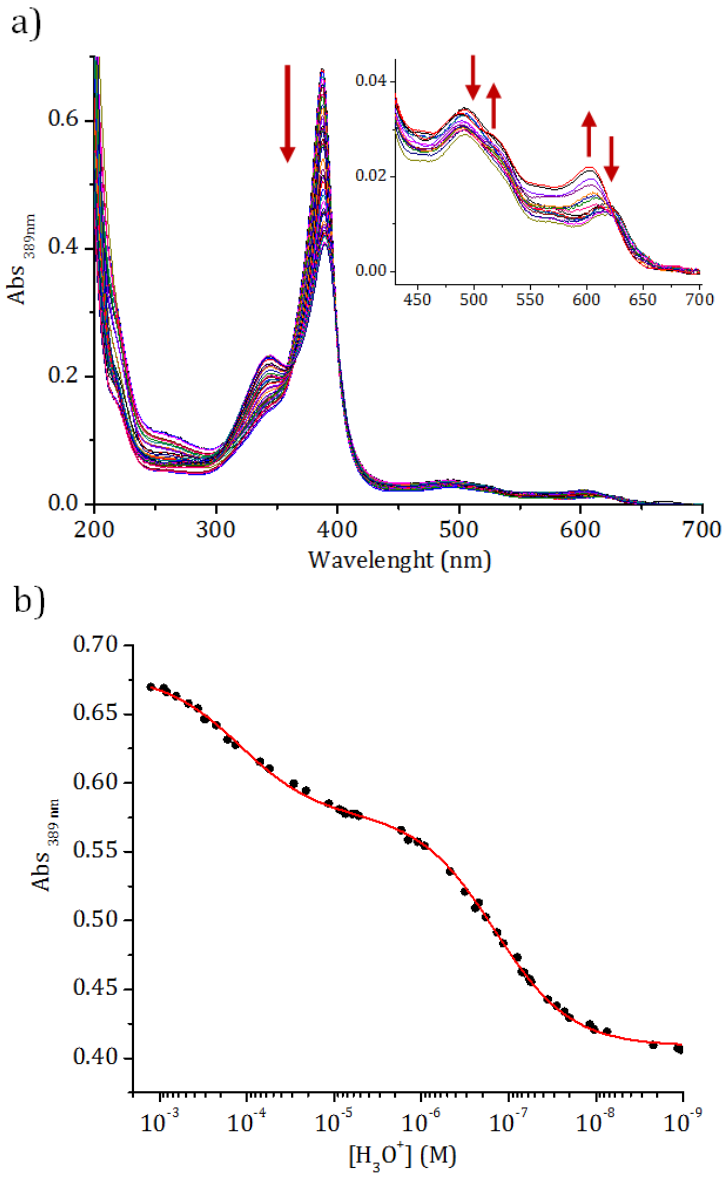


**Figure 37** a) UV-Vis spectra of $Fe^{III}$-Lys9Dab(*D*)-Mimochrome VI*a* isomer 2 ($6.0 \cdot 10^{-6}$ M) in $H_2O$/TFE, 50/50 (v/v) at various pHs (2.5–9.0). The arrows indicate the observed intensity changes of the Soret, Q and CT bands at increasing pHs. b) Plot of the absorbance at 389 nm as function of pH. The black dots are the experimental data, which were fitted with a two transitions model (red line).

For $Fe^{III}$-Lys9Dab(*D*)-Mimochrome VI*a* isomer 2, two well-resolved transitions were observed, with midpoint at pH 3.9 ± 0.1 and 6.8 ± 0.1 (Figure 37 b).
At pH around 3.0, the spectrum is typical of a predominantly high spin ferric porphyrin, with the Soret band at 387 nm, the Q bands at 491 and 528 nm, and the CT band at 614 nm. An increase in the pH from 3.0 to 5.3 causes a decrease in intensity and a slight red shift of the Soret (388 nm) and CT bands (615 nm): these observations are consistent with the change in the ferric ion axial coordination from $H_2O/H_2O$ to $His/H_2O$.[6,9] At pH around 8.0, the Soret band shifts to 390 nm, the Q band appears as a shoulder at 524 nm; the band at 488 and 602 nm can be attributed to the CT band of the ferric complex with the hydroxide ion mainly in the high spin state.[10,11] Therefore, also for $Fe^{III}$-Lys9Dab(*D*)-Mimochrome VI*a* isomer 2, the second transition corresponds to a ligand exchange in the ferric ion axial coordination from $H_2O$ to $OH^-$.

Finally, for both isomers at increasing pHs, the band at 345 nm broadens and the relative intensity of this band to the Soret band changes from 0.2 (at pH 2.5) to 0.57 (at pH 9). Even though the presence of a broad band at around 350 nm has been sometimes attributed to intermolecular heme–heme association,[12] experimental evidence suggests that this is not the case for $Fe^{III}$–Lys9Dab(*D*)-Mimochrome VI*a* isomer 1 and 2. In fact, a linear correlation, in aqueous neutral solutions, between absorbance and concentration in the range $10^{-7}$–$10^{-5}$ M, indicates a negligible association phenomena (data not shown).

## 2.3.2 Analysis of the secondary structure: CD spectroscopy in the far-UV region

The secondary structure of $Fe^{III}$-Lys9Dab(*D*)-Mimochrome VI*a* isomer 1 and 2 and its dependence on TFE content was investigated by circular dichroism (CD) in the far-UV region (190-260 nm).

On the basis of the UV-Vis titration, the spectra were acquired at pH 5.0 and 9.0, at which one predominant species is present in solution (His/$H_2O$ and His/$OH^-$, respectively, relative to the ferric ion axial coordination). Moreover, the spectra were acquired at the pH of highest activity (6.5).

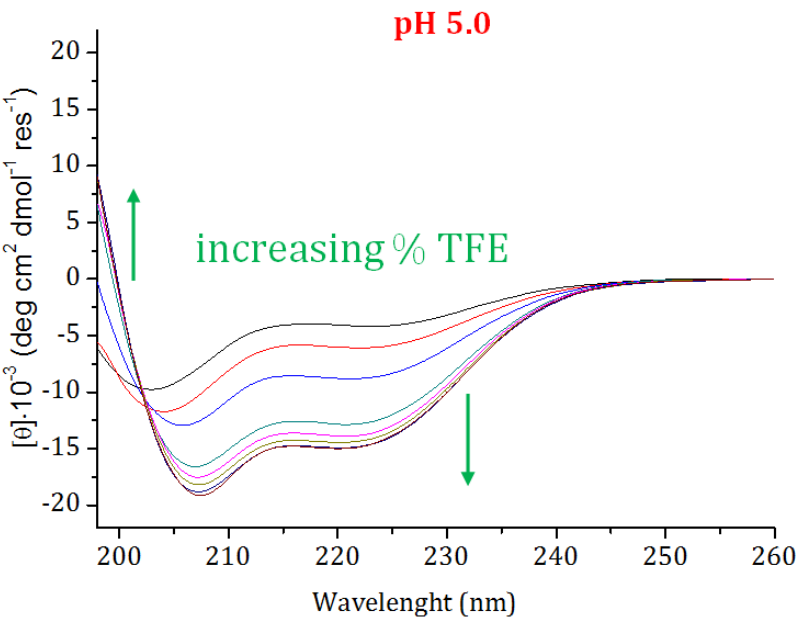


**Figure 38** Far-UV CD spectra of $Fe^{III}$-Lys9Dab(*D*)-Mimochrome VI*a* isomer 1 ($5.0 \cdot 10^{-6}$ M) in phosphate buffer 20 mM pH 5.0 at various TFE percentages (v/v), acquired in a 1.0 cm path length cuvette.

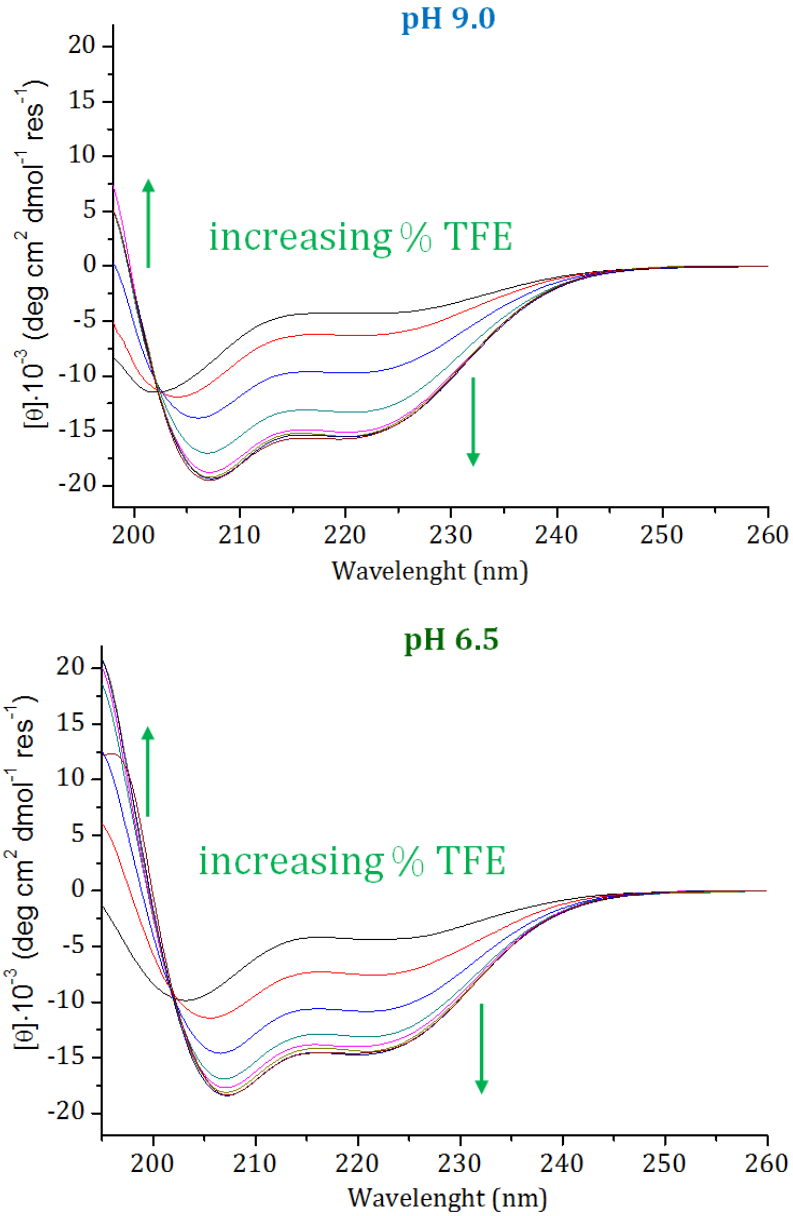


**Figure 39** Far-UV CD spectra of $Fe^{III}$-Lys9Dab(*D*)-Mimochrome VI*a* isomer 1 ($5.0 \cdot 10^{-6}$ M) in phosphate buffer 20 mM pH 9.0 (top) and 6.5 (bottom) at various TFE percentages (v/v), acquired in a 1.0 cm path length cuvette.

The TFE is a co-solvent known for its capability to stabilize helical structure in peptides.[13–15] The spectra at higher TFE content are characterized by a negative band around 222 nm (amide transition n-π*), a negative band between 203-207 nm (amide transition π-π*) and a positive band around 190 nm (amide transition π-π*, perpendicular coupling), which are all typical features of a helical arrangement of the peptide chains.[16]
In particular, the transition from random coil to helix is identifiable by some characteristic spectral changes:

- increase in the absolute value of the mean residue ellipticity at 222 nm ($[\theta]_{222}$);
- increase in the ratio between $[\theta]_{222}$ and $[\theta]_{min}$ values ($[\theta]_{ratio}$), progressively closer to the unity;
- shift of the wavelength of $[\theta]_{min}$ ($\lambda_{min}$) towards 207 nm;
- shift of $\lambda_0$ towards higher values.

In Table 6-8, the main parameters of the far-UV CD spectra of $Fe^{III}$-Lys9Dab(*D*)-Mimochrome VI*a* isomer 1 are reported.

**pH 5.0**

| %TFE | $[\Theta]_{min}$ ·10$^{-3}$ (deg cm$^2$ dmol$^{-1}$ res$^{-1}$) | $[\Theta]_{222}$ ·10$^{-3}$ (deg cm$^2$ dmol$^{-1}$ res$^{-1}$) | $[\Theta]_{ratio}$ | $\lambda_0$ (nm) |
|---|---|---|---|---|
| 0 | -9.759 (202.8) | -4.159 | 0.43 | 193.8 |
| 5 | -11.71 (204.0) | -6.083 | 0.52 | 194.6 |
| 10 | -12.92 (205.8) | -8.793 | 0.68 | 197.8 |
| 20 | -16.57 (207.0) | -12.79 | 0.77 | 199.4 |
| 25 | -17.52 (207.2) | -13.81 | 0.79 | 199.6 |
| 30 | -18.18 (207.2) | -14.32 | 0.79 | 199.6 |
| 40 | -18.81 (207.2) | -14.80 | 0.79 | 199.8 |
| 50 | -19.13 (207.4) | -14.84 | 0.78 | 199.8 |

**Table 6** Parameters of the far-UV CD spectra of $Fe^{III}$-Lys9Dab(*D*)-Mimochrome VI*a* isomer 1 in phosphate buffer 20 mM at pH 5.0 at various TFE percentages (v/v).

**pH 9.0**

| %TFE | $[\Theta]_{min}$ ·10$^{-3}$ (deg cm$^2$ dmol$^{-1}$ res$^{-1}$) | $[\Theta]_{222}$ ·10$^{-3}$ (deg cm$^2$ dmol$^{-1}$ res$^{-1}$) | $[\Theta]_{ratio}$ | $\lambda_0$ (nm) |
|---|---|---|---|---|
| 0 | -11.47 (201.6) | -4.285 | 0.37 | 194.0 |
| 5 | -11.96 (204.2) | -6.299 | 0.53 | 194.8 |
| 10 | -13.83 (206.0) | -9.684 | 0.70 | 198.2 |
| 15 | -17.03 (207.0) | -13.24 | 0.78 | 199.4 |
| 20 | -18.80 (207.2) | -14.99 | 0.80 | 199.6 |
| 25 | -19.24 (207.2) | -15.32 | 0.80 | 199.4 |
| 40 | -19.35 (207.4) | -15.38 | 0.79 | 199.6 |
| 50 | -19.51 (207.0) | -15.49 | 0.79 | 199.4 |

**Table 7** Parameters of the far-UV CD spectra of $Fe^{III}$-Lys9Dab(*D*)-Mimochrome VI*a* isomer 1 in phosphate buffer 20 mM at pH 9.0 at various TFE percentages (v/v).

**pH 6.5**

| %TFE | $[\Theta]_{min}$ ·10$^{-3}$ (deg cm$^2$ dmol$^{-1}$ res$^{-1}$) | $[\Theta]_{222}$ ·10$^{-3}$ (deg cm$^2$ dmol$^{-1}$ res$^{-1}$) | $[\Theta]_{ratio}$ | $\lambda_0$ (nm) |
|---|---|---|---|---|
| 0 | -9.856 (203.2) | -4.339 | 0.44 | 194.0 |
| 10 | -11.42 (205.6) | -7.568 | 0.66 | 197.8 |
| 15 | -14.59 (206.6) | -10.79 | 0.74 | 198.8 |
| 20 | -16.89 (207.0) | -13.07 | 0.77 | 199.4 |
| 25 | -17.69 (207.0) | -13.83 | 0.78 | 199.6 |
| 30 | -18.11 (207.2) | -14.34 | 0.79 | 199.6 |
| 40 | -18.40 (207.2) | -14.57 | 0.79 | 199.6 |
| 50 | -18.36 (207.2) | -14.43 | 0.79 | 200.0 |

**Table 8** Parameters of the far-UV CD spectra of $Fe^{III}$-Lys9Dab(*D*)-Mimochrome VI*a* isomer 1 in phosphate buffer 20 mM at pH 6.5 at various TFE percentages (v/v).

The parameters of the far-UV CD spectra of $Fe^{III}$-Lys9Dab(*D*)-Mimochrome VI*a* isomer 1 are very similar at all the three explored pHs. Increasing the TFE content up to 50% (v/v), it is possible to observe that:

- $[\theta]_{222}$ increases in absolute value from 4200 to 15000 deg cm$^2$ dmol$^{-1}$ res$^{-1}$;
- $[\theta]_{min}$ increases in absolute value from ≈ 10000 to ≈ 19000 deg cm$^2$ dmol$^{-1}$ res$^{-1}$;
- $[\theta]_{ratio}$ increases from 0.4 to 0.8;
- $\lambda_{min}$ shifts from 202 nm to 207 nm;
- $\lambda_0$ shifts from 194 nm to 200 nm.

To further investigate the helix formation, the mean residue ellipticity at 222 nm was reported as a function of TFE content at the three explored pHs:

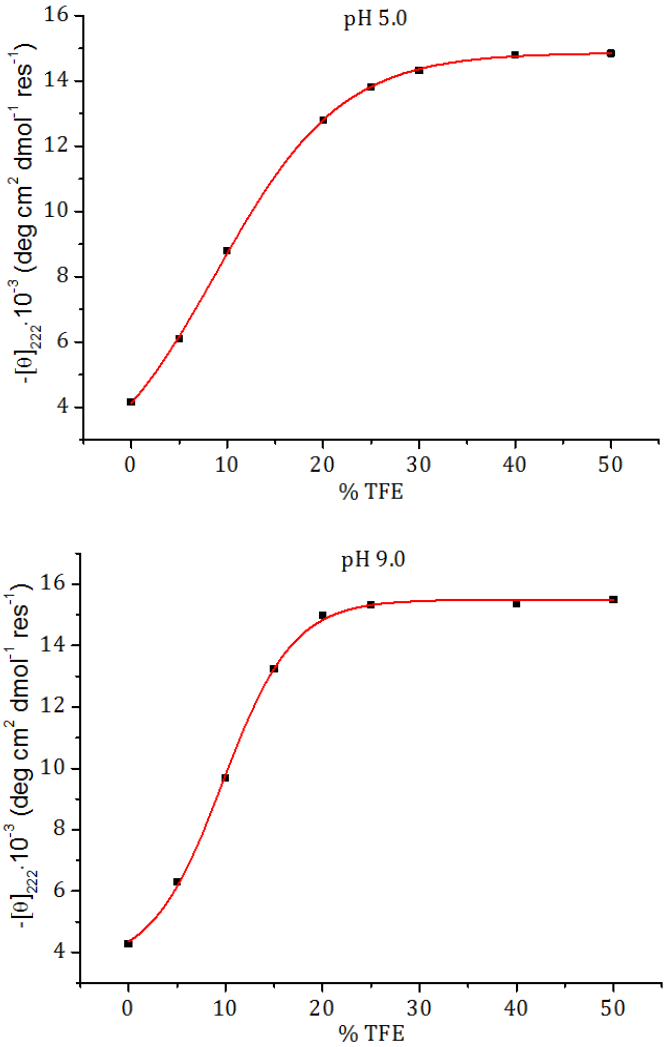


**Figure 40** Plot of $[\theta]_{222}$ as a function of TFE percentage (v/v) of $Fe^{III}$-Lys9Dab(*D*)-Mimochrome VI*a* isomer 1 in phosphate buffer 20 mM at pH 5.0 (top) and 9.0 (bottom).

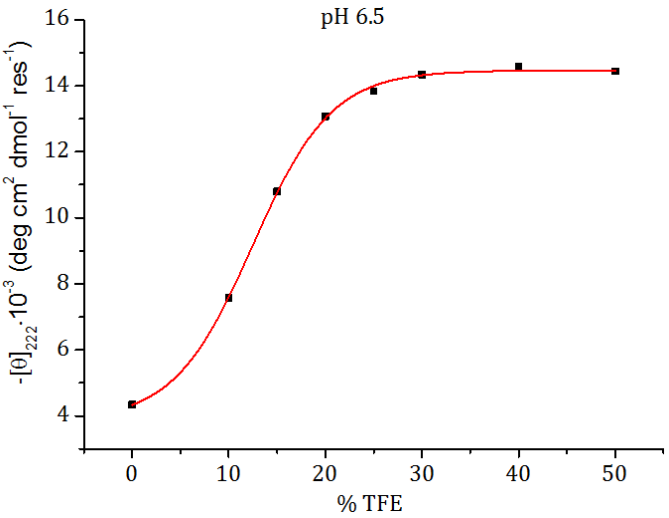


**Figure 41** Plot of $[\theta]_{222}$ as a function of TFE percentage (v/v) of $Fe^{III}$-Lys9Dab(*D*)-Mimochrome VI*a* isomer 1 in phosphate buffer 20 mM at pH 6.5.

There is a sigmoidal trend of the experimental data, which confirm a mainly α-helical conformation of the peptide chains.[15] The peptide chains, poorly structured in water, fold into a helix upon addition of 35%, 25% and 30% TFE (v/v) at pH 5.0, 9.0 and 6.5, respectively.

The same experiments have been performed on $Fe^{III}$-Lys9Dab(*D*)-Mimochrome VI*a* isomer 2 (Figure 42-43). In Table 9-11 the main parameters of the far-UV CD spectra are reported.

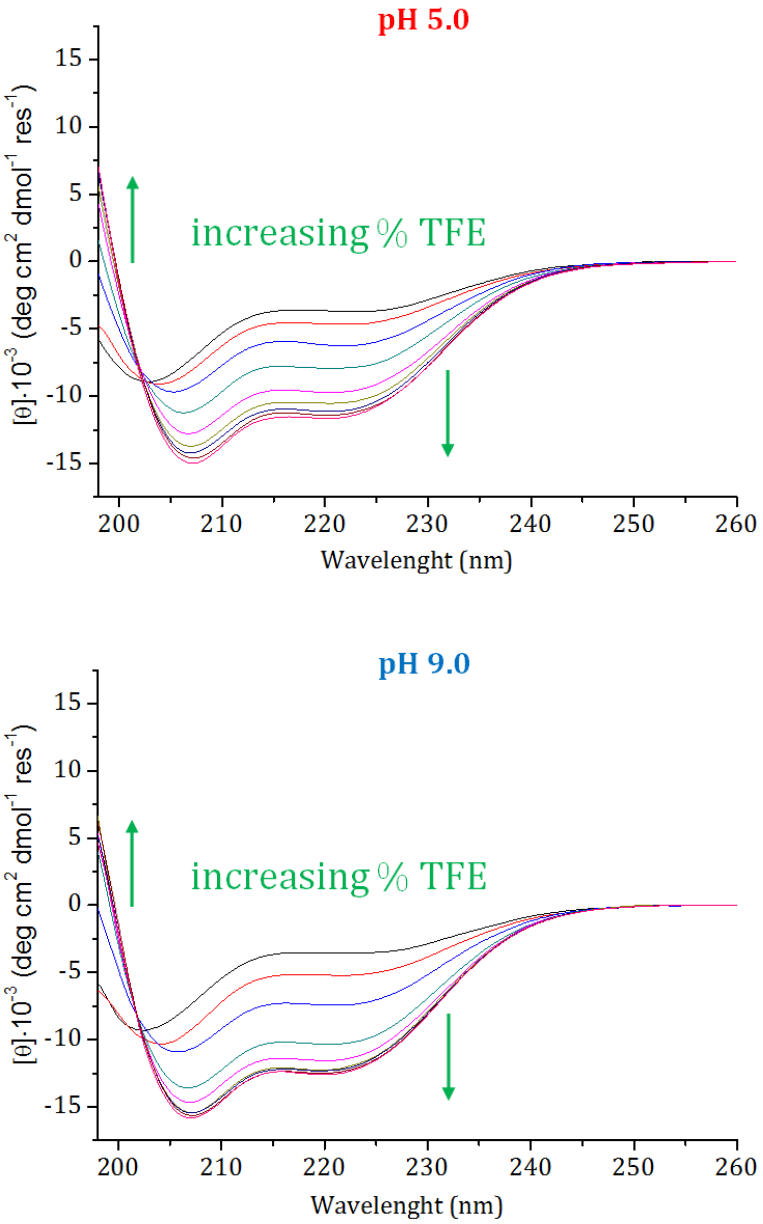


**Figure 42** Far-UV CD spectra of $Fe^{III}$-Lys9Dab(*D*)-Mimochrome VI*a* isomer 2 ($5.0 \cdot 10^{-6}$ M) in phosphate buffer 20 mM pH 5.0 (top) and 9.0 (bottom) at various TFE percentages (v/v), acquired in a 1.0 cm path length cuvette.

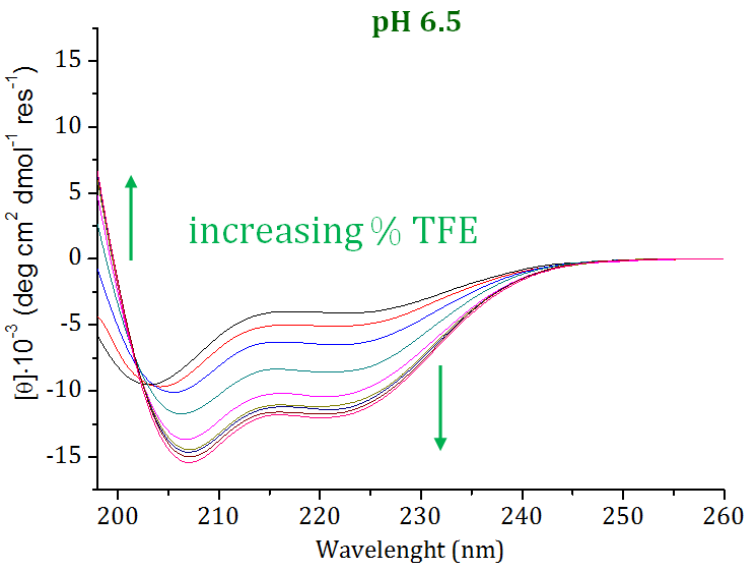


**Figure 43** Far-UV CD spectra of $Fe^{III}$-Lys9Dab(*D*)-Mimochrome VI*a* isomer 2 ($5.0 \cdot 10^{-6}$ M) in phosphate buffer 20 mM pH 6.5 at various TFE percentages (v/v), acquired in a 1.0 cm path length cuvette.

**pH 5.0**

| %TFE | $[\Theta]_{min} \cdot 10^{-3}$ (deg cm$^2$ dmol$^{-1}$ res$^{-1}$) | $[\Theta]_{222} \cdot 10^{-3}$ (deg cm$^2$ dmol$^{-1}$ res$^{-1}$) | $[\Theta]_{ratio}$ | $\lambda_0$ (nm) |
|---|---|---|---|---|
| 0 | -8.933 (202.8) | -3.700 | 0.41 | 193.4 |
| 5 | -9.104 (203.8) | -4.661 | 0.51 | 194.6 |
| 10 | -9.687 (205.2) | -6.262 | 0.65 | 197.6 |
| 15 | -11.23 (206.2) | -7.897 | 0.70 | 198.6 |
| 20 | -12.79 (206.8) | -9.680 | 0.76 | 199.2 |
| 25 | -13.73 (207.0) | -10.47 | 0.76 | 199.6 |
| 30 | -14.23 (207.0) | -11.07 | 0.78 | 199.6 |
| 40 | -14.60 (207.2) | -11.33 | 0.78 | 199.6 |
| 50 | -14.98 (207.2) | -11.55 | 0.77 | 199.6 |

**Table 9** Parameters of the far-UV CD spectra of $Fe^{III}$-Lys9Dab(*D*)-Mimochrome VI*a* isomer 2 in phosphate buffer 20 mM at pH 5.0 at various TFE percentages (v/v).

**pH 9.0**

| %TFE | $[\Theta]_{min} \cdot 10^{-3}$ (deg cm$^2$ dmol$^{-1}$ res$^{-1}$) | $[\Theta]_{222} \cdot 10^{-3}$ (deg cm$^2$ dmol$^{-1}$ res$^{-1}$) | $[\Theta]_{ratio}$ | $\lambda_0$ (nm) |
|---|---|---|---|---|
| 0 | -9.314 (202.4) | -3.566 | 0.38 | 193.8 |
| 5 | -10.32 (204.2) | -5.217 | 0.51 | 194.8 |
| 10 | -10.91 (205.8) | -7.421 | 0.68 | 197.8 |
| 15 | -13.60 (206.8) | -10.28 | 0.76 | 199.2 |
| 20 | -14.67 (207.0) | -11.45 | 0.78 | 199.4 |
| 25 | -15.43 (207.2) | -12.06 | 0.78 | 199.6 |
| 30 | -15.45 (207.2) | -12.16 | 0.79 | 199.6 |
| 40 | -15.83 (207.0) | -12.32 | 0.78 | 199.6 |
| 50 | -15.83 (207.0) | -12.53 | 0.79 | 199.4 |

**Table 10** Parameters of the far-UV CD spectra of $Fe^{III}$-Lys9Dab(*D*)-Mimochrome VI*a* isomer 2 in phosphate buffer 20 mM at pH 9.0 at various TFE percentages (v/v).

**pH 6.5**

| %TFE | $[\Theta]_{min} \cdot 10^{-3}$ (deg cm$^2$ dmol$^{-1}$ res$^{-1}$) | $[\Theta]_{222} \cdot 10^{-3}$ (deg cm$^2$ dmol$^{-1}$ res$^{-1}$) | $[\Theta]_{ratio}$ | $\lambda_0$ (nm) |
|---|---|---|---|---|
| 0 | -9.532 (203.0) | -4.086 | 0.43 | 193.8 |
| 5 | -9.683 (204.2) | -5.092 | 0.53 | 194.6 |
| 10 | -10.11 (205.4) | -6.506 | 0.64 | 197.6 |
| 15 | -11.75 (206.2) | -8.545 | 0.73 | 198.8 |
| 20 | -13.67 (206.6) | -10.36 | 0.76 | 199.2 |
| 25 | -14.45 (207.2) | -11.06 | 0.77 | 199.4 |
| 30 | -14.65 (207.0) | -11.37 | 0.78 | 199.6 |
| 40 | -15.00 (207.2) | -11.66 | 0.78 | 199.6 |
| 50 | -15.43 (207.0) | -11.92 | 0.77 | 199.6 |

**Table 11** Parameters of the far-UV CD spectra of $Fe^{III}$-Lys9Dab(*D*)-Mimochrome VI*a* isomer 2 in phosphate buffer 20 mM at pH 6.5 at various TFE percentages (v/v).

For $Fe^{III}$-Lys9Dab(*D*)-Mimochrome VI*a* isomer 2 also, the parameters of the far-UV CD spectra are very similar at all the explored pHs. Increasing the TFE content up to 50% (v/v), the main changes detectable in the spectra are that:

- $[\theta]_{222}$ increases in absolute value from 3600 to 12000 deg $cm^2$ $dmol^{-1}$ $res^{-1}$;
- $[\theta]_{min}$ increases in absolute value from ≈ 9000 to ≈ 16000 deg $cm^2$ $dmol^{-1}$ $res^{-1}$;
- $[\theta]_{ratio}$ increases from 0.4 to 0.8;
- $\lambda_{min}$ shifts from 202 nm to 207 nm;
- $\lambda_0$ shifts from 194 nm to 200 nm.

Therefore: the shifts of $\lambda_{min}$ and $\lambda_0$ are the same for both isomers; at all the TFE percentages, $[\theta]_{222}$ and $[\theta]_{min}$ of the isomer 2 are lower in absolute value than those of the isomer 1, but their variation is such that the increase in $[\theta]_{ratio}$ upon TFE addition is identical for the two isomers.

In Figure 44-46, the plots of the mean residue ellipticity at 222 nm as a function of the TFE content at all the three investigated pHs are reported.

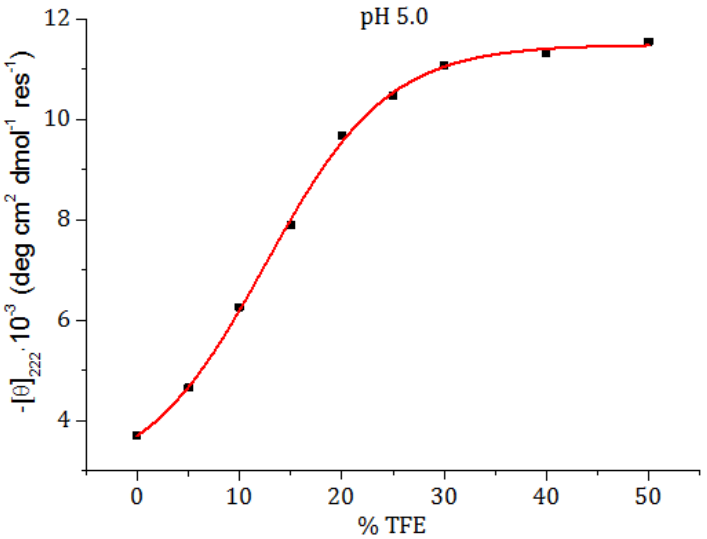


**Figure 44** Plot of $[\theta]_{222}$ as a function of TFE percentage (v/v) of $Fe^{III}$-Lys9Dab(*D*)-Mimochrome VI*a* isomer 2 in phosphate buffer 20 mM at pH 5.0.

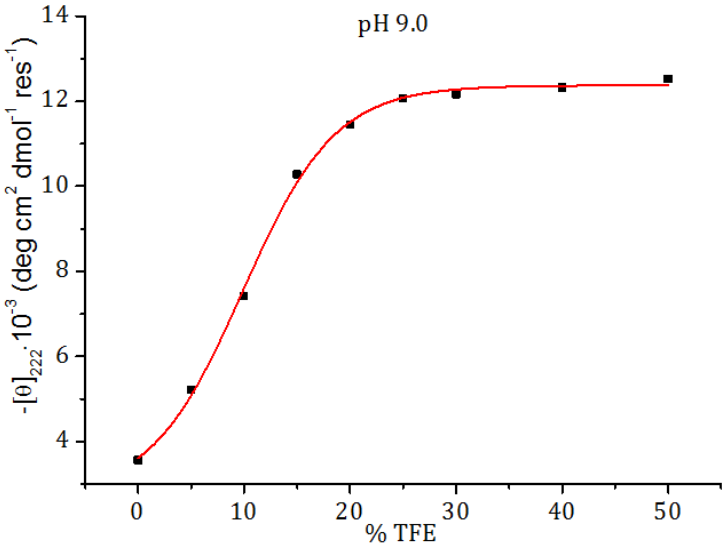


**Figure 45** Plot $[\theta]_{222}$ as a function of TFE percentage (v/v) of $Fe^{III}$-Lys9Dab(*D*)-Mimochrome VI*a* isomer 2 in phosphate buffer 20 mM at pH 9.0.

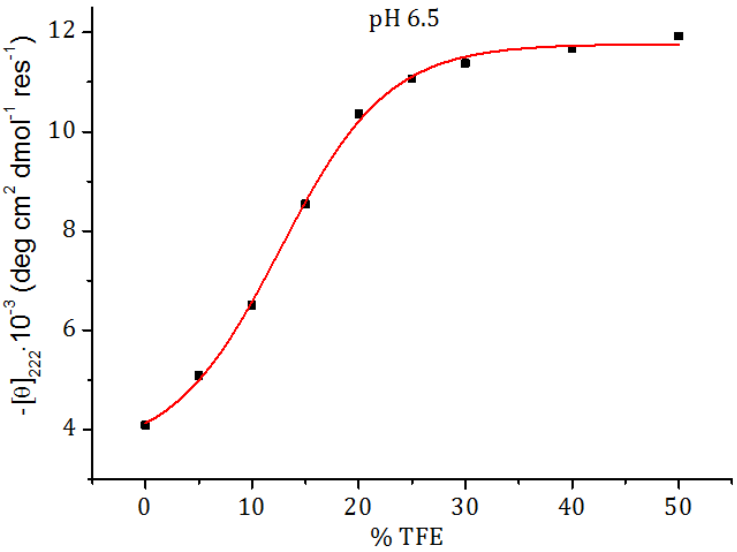


**Figure 46** Plot of $[\theta]_{222}$ as a function of TFE percentage (v/v) of $Fe^{III}$-Lys9Dab(*D*)-Mimochrome VI*a* isomer 2 in phosphate buffer 20 mM at pH 6.5.

For this isomer, there is also a sigmoidal trend of the mean residue ellipticity at 222 nm as a function of TFE percentage. The *plateau*, for each pH value concerned, is reached by adding the same percentages of TFE for the two isomers (35%, 25% and 30% TFE (v/v) at pH 5.0, 9.0, and 6.5, respectively).

### 2.3.3 From secondary to tertiary structure: CD spectroscopy in the Soret region

In order to elucidate the peptide-heme interactions in the sandwiched structure, the CD spectra of the two new developed enzymes were acquired also in the Soret region (300-460 nm) at pH 5.0, 6.5 and 9.0. For each investigated pH, the dependence of the CD spectra on the TFE content was explored.

The CD spectra of $Fe^{III}$-Lys9Dab(*D*)-Mimochrome VI*a* isomer 1 in 10 mM phosphate buffer pH 5.0 and 6.5, at different TFE percentages (v/v) are reported in Figure 47 and 48, respectively.

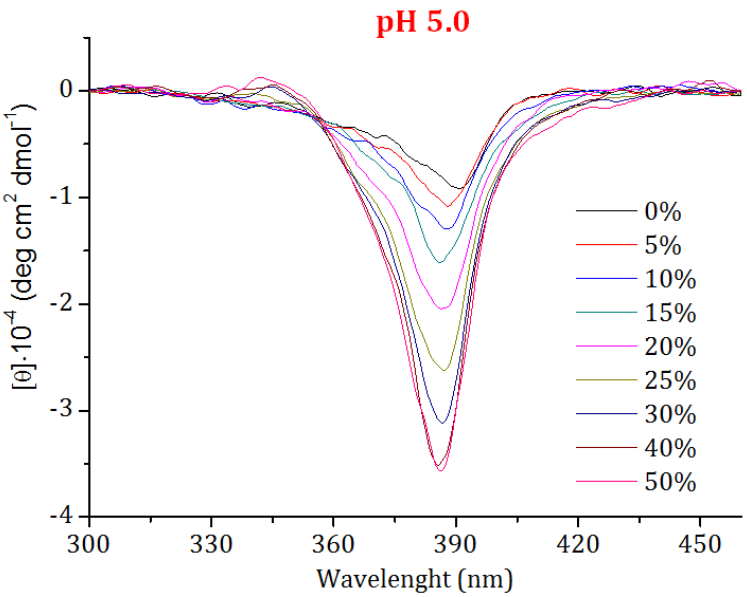


**Figure 47** CD spectra in the Soret region (300-460 nm) of $Fe^{III}$-Lys9Dab(*D*)-Mimochrome VI*a* isomer 1 ($1.5 \cdot 10^{-5}$ M) in phosphate buffer 10 mM pH 5.0 at various TFE percentages (v/v), acquired in a 1.0 cm path length cuvette.

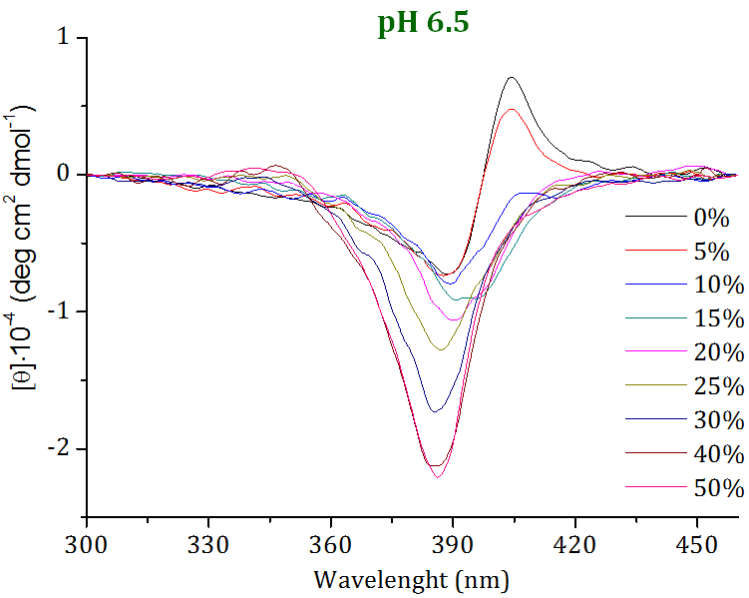


**Figure 48** CD spectra in the Soret region (300-460 nm) of $Fe^{III}$-Lys9Dab(*D*)-Mimochrome VI*a* isomer 1 ($2.1 \cdot 10^{-5}$ M) in phosphate buffer 10 mM pH 6.5 at various TFE percentages (v/v), acquired in a 1.0 cm path length cuvette.

As shown in Figure 47-48, the shape and the intensity of the induced Cotton effect in the Soret region is related to the solvent composition. At pH 5.0, the spectrum displays a negative induced Cotton effect, centered at 386.4 nm, whose intensity increases by increasing the TFE concentration. At pH 6.5 and without TFE, the spectrum is *S*-shaped with a $\lambda_0$ at 398 nm; by adding TFE, the positive induced Cotton effect decreases in intensity, so that at TFE content higher than 15%, only the negative induced Cotton effect (centered at 386.4 nm) is detected. The dependence on TFE content of $[\theta]_{386.4}$ and $[\theta]_{404.2}$, at each investigated pH, is reported in Figure 49, 50 and 51.

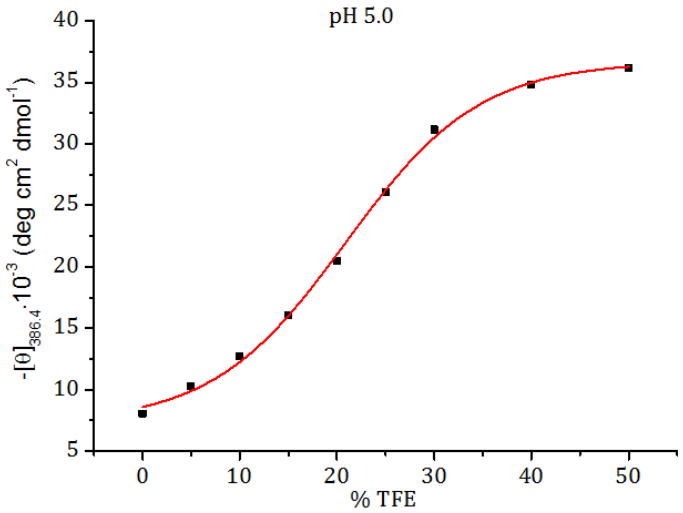


**Figure 49** Plot of $[\theta]_{386.4}$ as a function of TFE percentage (v/v) of $Fe^{III}$-Lys9Dab(*D*)-Mimochrome VI*a* isomer 1 in phosphate buffer 10 mM at pH 5.0.

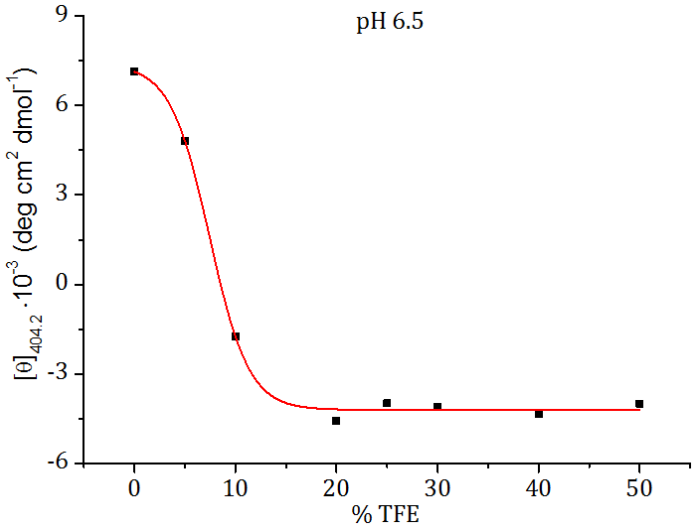


**Figure 50** Plot of $[\theta]_{404.2}$ as a function of TFE percentage (v/v) of $Fe^{III}$-Lys9Dab(*D*)-Mimochrome VI*a* isomer 1 in phosphate buffer 10 mM at pH 6.5.

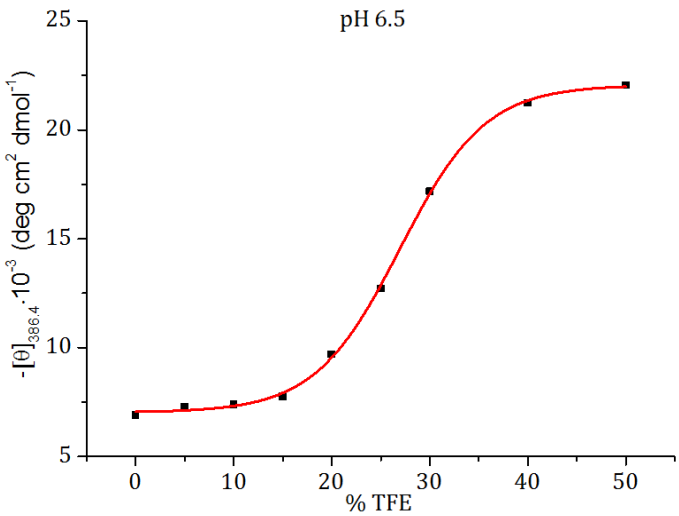


**Figure 51** Plot of $[\theta]_{386.4}$ as a function of TFE percentage (v/v) of $Fe^{III}$-Lys9Dab(*D*)-Mimochrome VI*a* isomer 1 in phosphate buffer 10 mM at pH 6.5.

The increase in absolute value of the induced Cotton effect intensity at pH 5.0 follows a sigmoidal trend, reaching a *plateau* at 40% TFE (Figure 49).

The positive Cotton effect at pH 6.5 decreases upon TFE addition (0-15%); on the contrary, the negative induced Cotton effect intensity increases in absolute value by increasing the TFE content from 15 up to 40% (Figure 50-51).

At pH 9.0, a weak *S*-shaped Cotton effect is found, centered at 398.0 nm, whose intensity decreases up to zero upon TFE addition. At 50% TFE, a weak negative induced Cotton effect is found (data not shown).

The same experiments were performed on $Fe^{III}$-Lys9Dab(*D*)-Mimochrome VI*a* isomer 2. For this isomer, a similar behaviour to this found for the isomer 1 was

observed in the Soret region as a function of pH and TFE. At pH 5.0 a negative induced Cotton effect was observed, centered at 386.0 nm, whose intensity increases by increasing the TFE concentration (Figure 52). At pH 6.5 and without TFE, the observed spectrum is *S*-shaped, with a $\lambda_0$ at 399.4 nm; by adding TFE, only one negative induced Cotton effect, centered at 386.8 nm, is detected (Figure 53).

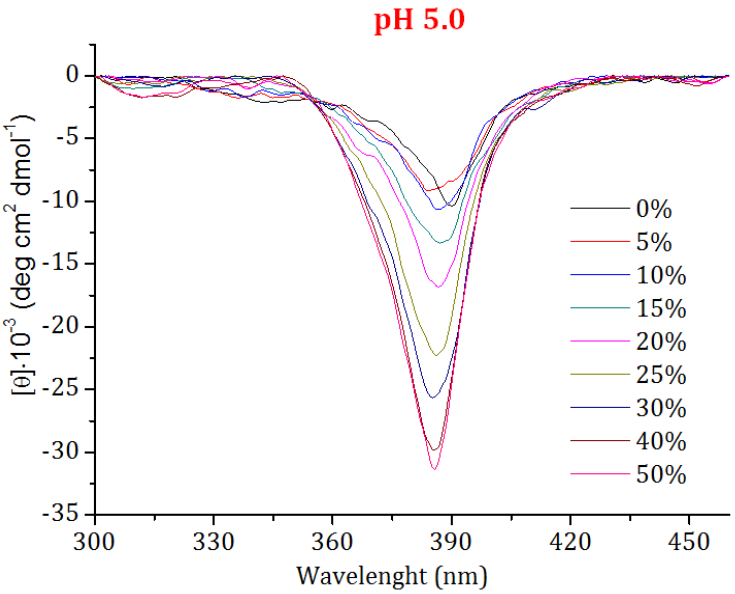


**Figure 52** CD spectra in the Soret region (300-460 nm) of $Fe^{III}$-Lys9Dab(*D*)-Mimochrome VI*a* isomer 2 ($1.8 \cdot 10^{-5}$ M) in phosphate buffer 10 mM pH 5.0 at various TFE percentages (v/v), acquired in a 1.0 cm path length cuvette.

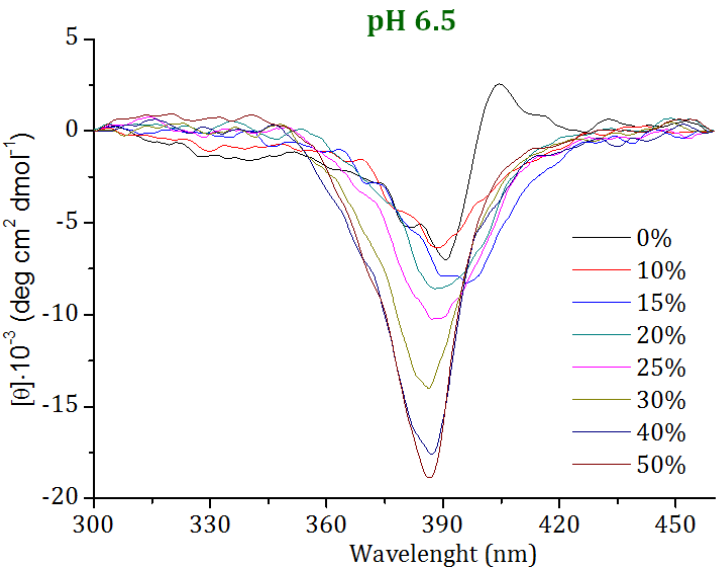


**Figure 53** CD spectra in the Soret region (300-460 nm) of $Fe^{III}$-Lys9Dab(*D*)-Mimochrome VI*a* isomer 2 ($1.8 \cdot 10^{-5}$ M) in phosphate buffer 10 mM pH 6.5 at various TFE percentages (v/v), acquired in a 1.0 cm path length cuvette.

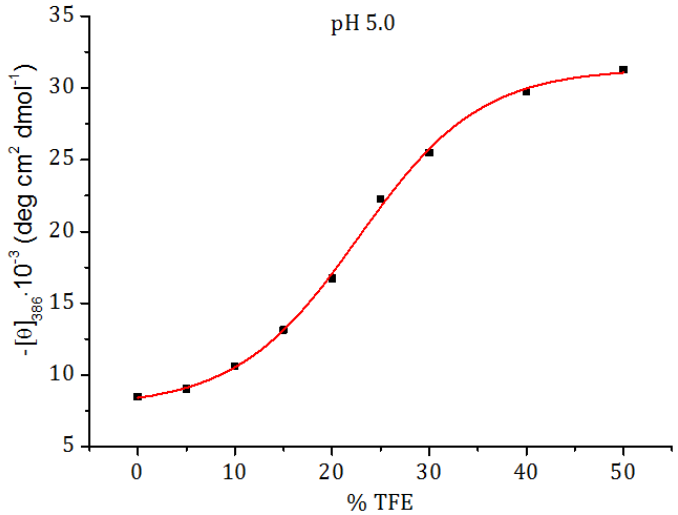


**Figure 54** Plot of $[\theta]_{386}$ as a function of TFE percentage (v/v) of $Fe^{III}$-Lys9Dab(*D*)-Mimochrome VI*a* isomer 2 in phosphate buffer 10 mM at pH 5.0.

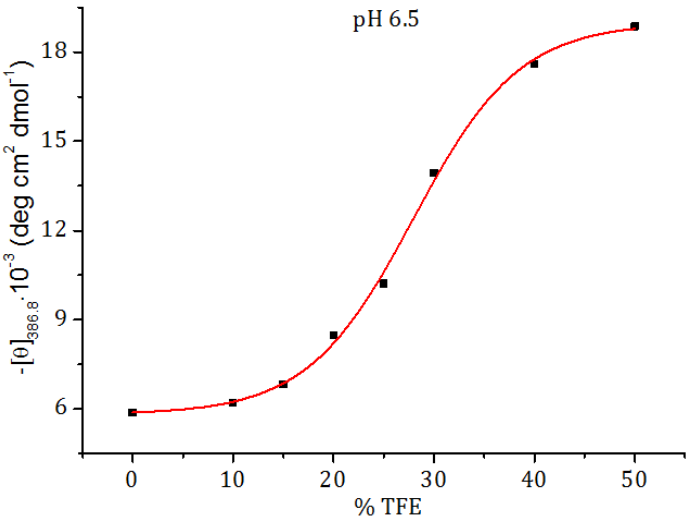


**Figure 55** Plot of $[\theta]_{386.8}$ as a function of TFE percentage (v/v) of $Fe^{III}$-Lys9Dab(*D*)-Mimochrome VI*a* isomer 2 in phosphate buffer 10 mM at pH 6.5.

The increase in absolute value of the induced Cotton effect intensity at pH 5.0 and 6.5 follows a sigmoidal trend, reaching a *plateau* at 40% and 45% TFE, respectively (Figure 54 and 55).

At pH 9.0, without TFE, no Cotton effect is detected. By adding TFE up to 50%, a weak negative Cotton effect is found (data not shown).

The main parameters of the CD spectra in the Soret region of $Fe^{III}$-Lys9Dab(*D*)-Mimochrome VI*a* isomer 1 and 2 in phosphate buffer 10 mM pH 5.0, 6.5 and 9.0 with different TFE content, are summarized in Table 12.

| | pH | %TFE (v/v) | $[\Theta]_{386.4} \cdot 10^{-3}$ (deg cm$^2$ dmol$^{-1}$) | $[\Theta]_{404.2} \cdot 10^{-3}$ (deg cm$^2$ dmol$^{-1}$) |
|---|---|---|---|---|
| ISOMER 1 | 5.0 | 0 | -8.0 | |
| | | 50 | -36 | |
| | 6.5 | 0 | -6.9 | +7.1 |
| | | 15 | -7.8 | |
| | | 50 | -22 | |
| | 9.0 | 0 | -3.2 | +2.2 (405.0) |
| | | 15 | -- | -- |
| | | 50 | -2.8 (387.8) | -- |

| | pH | %TFE (v/v) | $[\Theta]_{386.0} \cdot 10^{-3}$ (deg cm$^2$ dmol$^{-1}$) | $[\Theta]_{404.4} \cdot 10^{-3}$ (deg cm$^2$ dmol$^{-1}$) |
|---|---|---|---|---|
| ISOMER 2 | 5.0 | 0 | -8.5 | |
| | | 50 | -31 | |
| | 6.5 | 0 | -5.9 (386.8) | +2.5 |
| | | 50 | -19 (386.8) | |
| | 9.0 | 0 | -- | -- |
| | | | -4.1 (387.2) | -- |

**Table 12** Main parameters of the CD spectra in the Soret region (360-400 nm) of $Fe^{III}$-Lys9Dab(*D*)-Mimochrome VI*a* isomer 1 and 2. The missing values (--) are lower than $1.5 \cdot 10^3$ deg cm$^2$ dmol$^{-1}$ in absolute value. $\lambda_{max}$ values are reported in parenthesis.

### 2.3.4 Spin state: Mössbauer spectroscopy

The characterization of the most active complexes by Mössbauer spectroscopy was performed in collaboration with Prof. Franc Meyer Group at the Institute of Inorganic Chemistry, Georg-August University in Göttingen (Germany).

Mössbauer spectra have been collected on $Fe^{III}$-Lys9Dab(*D*)-Mimochrome VI*a* isomer 1 and 2 in solid state (lyophilized from acid conditions), at T= 6K.

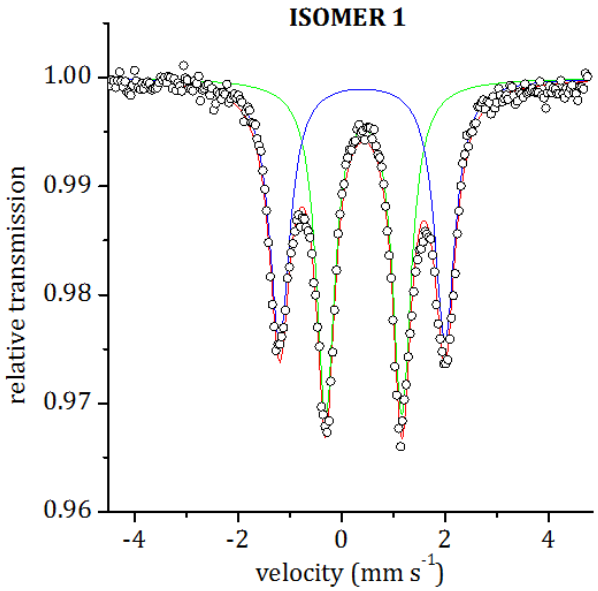


**Figure 56** Mössbauer spectrum of $Fe^{III}$-Lys9Dab(*D*)-Mimochrome VI*a* isomer 1 in solid state at T = 6K. Circles are the experimental data, which have been fitted with a two-states model (red line, sum of green and blue lines).

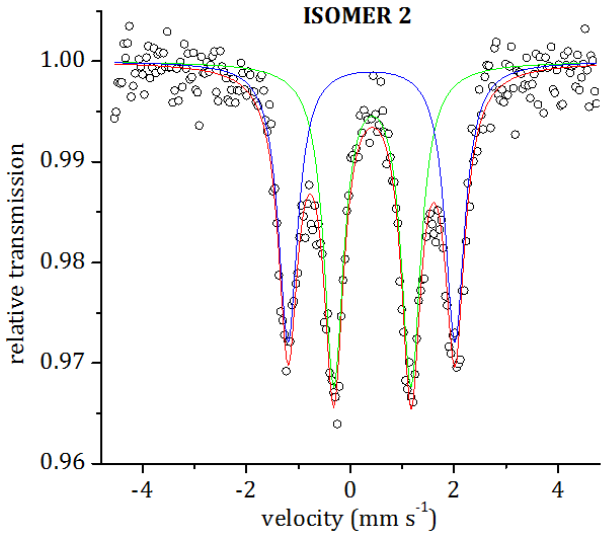


**Figure 57** Mössbauer spectrum of $Fe^{III}$-Lys9Dab(*D*)-Mimochrome VI*a* isomer 2 in solid state at T = 6K. Circles are the experimental data, which have been fitted with a two-states model (red line, sum of green and blue lines).

The Mössbauer spectra of both isomers show the presence of two species, and therefore have been fitted with a two-states model (red line, Figure 56-57), whose deconvolution returns two one-species spectra (green and blue lines, Figure 56-57).

Mössbauer spectra of both isomers have been also acquired at 80 and 200 K (Figure 58-59). The main parameters characterizing the Mössbauer spectra of these two species of $Fe^{III}$-Lys9Dab(*D*)-Mimochrome VI*a* isomer 1 and 2 at the three explored temperatures are reported in Table 13.

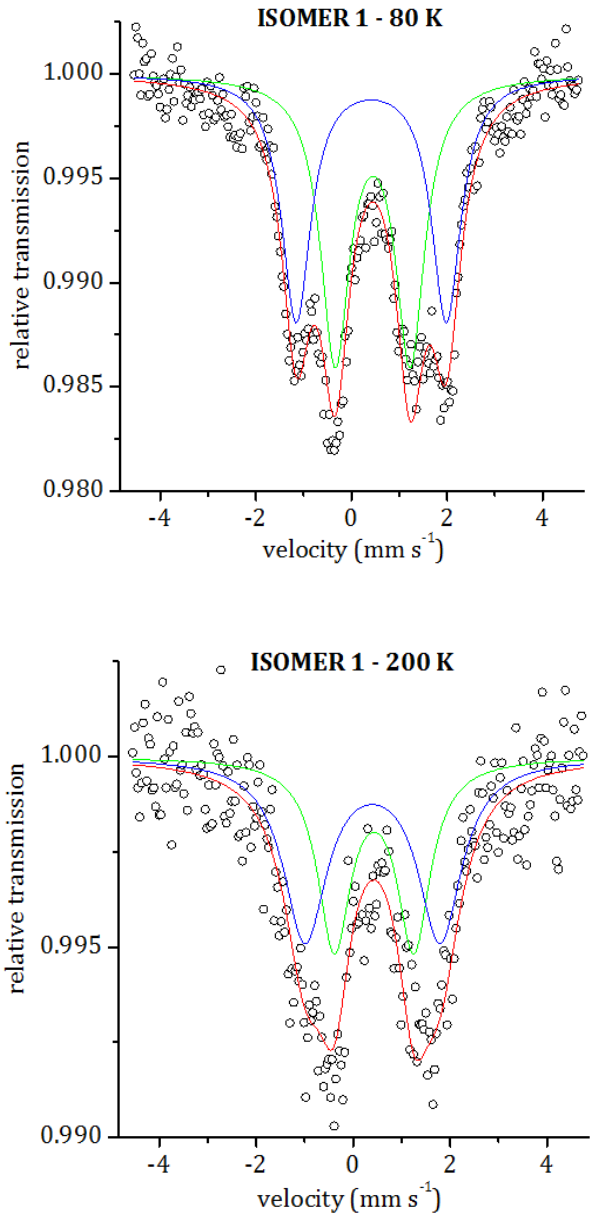


**Figure 58** Mössbauer spectra of $Fe^{III}$-Lys9Dab(*D*)-Mimochrome VI*a* isomer 1 in solid state at T = 80K (top) and 200K (bottom).

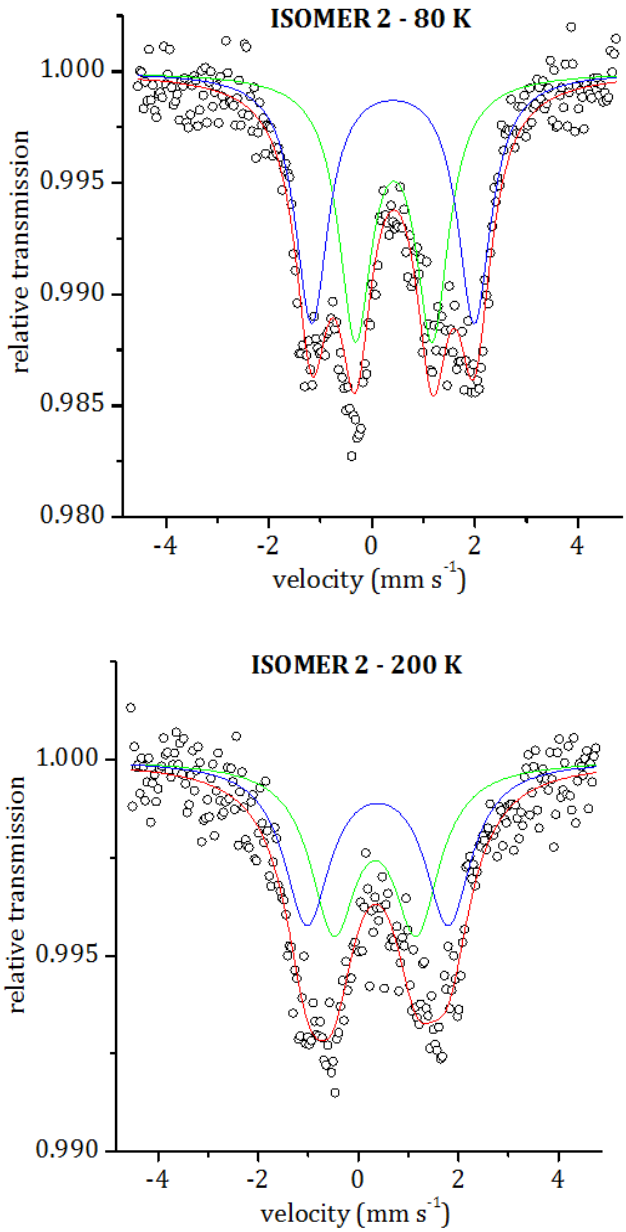


**Figure 59** Mössbauer spectra of $Fe^{III}$-Lys9Dab(*D*)-Mimochrome VI*a* isomer 2 in solid state at T = 80K (top) and 200K (bottom).

| | Enzyme | δ (mm s$^{-1}$) | $\Delta E_Q$ (mm s$^{-1}$) | FWHM (mm s$^{-1}$) | Relative inten. (%) |
|---|---|---|---|---|---|
| T = 6 K | ISOMER 1 | 0.42<br>0.40 | 1.47<br>3.20 | 0.43<br>0.48 | 53<br>47 |
| | ISOMER 2 | 0.43<br>0.41 | 1.49<br>3.21 | 0.46<br>0.45 | 53<br>47 |
| T = 80 K | ISOMER 1 | 0.44<br>0.41 | 1.57<br>3.14 | 0.74<br>0.74 | 53<br>47 |
| | ISOMER 2 | 0.42<br>0.41 | 1.49<br>3.16 | 0.78<br>0.78 | 51<br>49 |
| T = 200 K | ISOMER 1 | 0.43<br>0.40 | 1.64<br>2.78 | 0.83<br>1.09 | 45<br>55 |
| | ISOMER 2 | 0.33<br>0.38 | 1.65<br>2.82 | 1.12<br>1.12 | 50<br>50 |

**Table 13** Isomer shift (δ), quadrupole splitting ($\Delta E_Q$), full width half maximum (FWHM) and relative intensity of the two observed species in the Mössbauer spectra of $Fe^{III}$-Lys9Dab(*D*)-Mimochrome VI*a* isomer 1 and 2 at the indicated temperatures.

From the analysis of the parameters reported in Table 12, at T = 6K we can deduce that both isomers in solid state are a mixture of two spin states in about 1:1 (precisely 53:47) ratio. In particular, these species are the same for the two isomers. The first state has δ and $\Delta E_Q$ values typical of high spin (HS) $Fe^{III}$ state (S=5/2), whereas the second one has δ and $\Delta E_Q$ values in the range of the quantum mechanical admixed spin (QS) state (S=3/2, 5/2).[17]

A coordination complex having a quantum mechanical mixture of spin states corresponds to a single magnetic

species with magnetic properties distinct from pure spin species. This is different from a thermal mixtures of spin states in which molecules can be monitored in two magnetically distinguishable pure spin states. This mixing of spin states, although allowed by the selection rules, will only occur if the energy separation between unperturbed pure spin states is comparable or less than the spin-orbit coupling constant (about 300 $cm^{-1}$ in ferric heme complexes).[18]

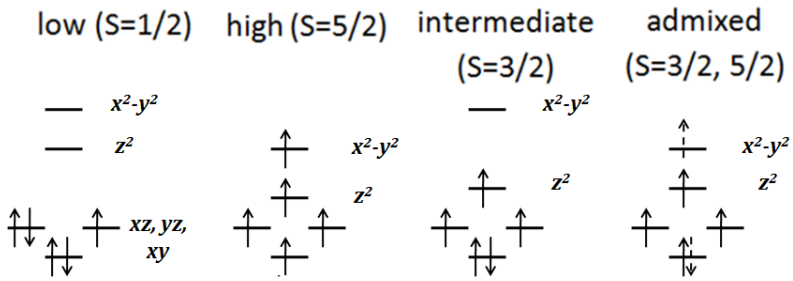


**Figure 60** Iron (III) spin states.

Increasing the temperature from 6 to 80K, and even up to 200K, there is an unexpected broadening of the signals (Figure 56-59, Table 13) for both isomers. Such broadening has been reported in literature as evidence of a temperature-dependent dynamic reorientation of ligands.[19] Further experiments are needed, to determine which kind of dynamic behavior we are observing.

Mössbauer spectra have been also collected in phosphate buffer 50 mM pH 6.5, 50% TFE (v/v), at T = 6K (Figure 61-62, Table 14).

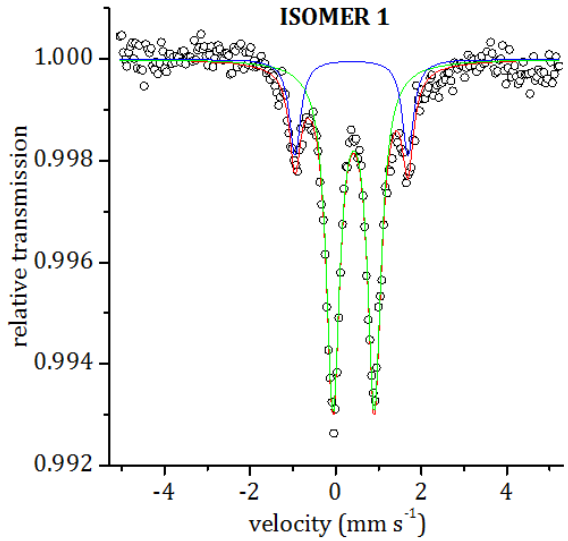


**Figure 61** Mössbauer spectrum of $Fe^{III}$-Lys9Dab(*D*)-Mimochrome VI*a* isomer 1 ($3.6 \cdot 10^{-3}$ M) in phosphate buffer 50 mM pH 6.5, 50% TFE (v/v).

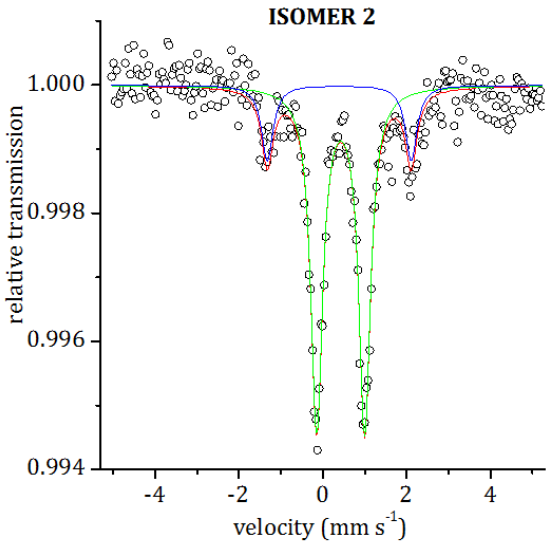


**Figure 62** Mössbauer spectrum of $Fe^{III}$-Lys9Dab(*D*)-Mimochrome VI*a* isomer 2 ($4.7 \cdot 10^{-3}$ M) in phosphate buffer 50 mM pH 6.5, 50% TFE (v/v).

| | Enzyme | δ (mm $s^{-1}$) | $\Delta E_Q$ (mm $s^{-1}$) | FWHM (mm $s^{-1}$) | Relative inten. (%) |
|---|---|---|---|---|---|
| T = 6 K | ISOMER 1 | 0.42<br>0.37 | 0.97<br>2.64 | 0.38<br>0.32 | 81<br>19 |
| | ISOMER 2 | 0.42<br>0.39 | 1.14<br>3.43 | 0.34<br>0.33 | 82<br>18 |

**Table 14** Isomer shift (δ), quadrupole splitting ($\Delta E_Q$), full width half maximum (FWHM) and relative intensity of the two observed species in the Mössbauer spectra of $Fe^{III}$-Lys9Dab(*D*)-Mimochrome VI*a* isomer 1 and 2 in phosphate buffer 50 mM pH 6.5, 50% TFE (v/v) at T= 6K.

The spectra show two species in about 80:20 ratio for both isomers. These species have been identified, respectively, as HS and QS configurations. Therefore, we find the same spin states in solid state and in solution, but in a different ratio. With a more precise analysis, we notice that the $\Delta E_Q$ values of the QS configurations for both isomers are quite different in solution and in solid state. For the isomer 1 such parameter is 2.64 mm $s^{-1}$, whereas larger quadrupole splitting values ($\Delta E_Q$ =2.8-3.5 mm $s^{-1}$) are expected for the QS state. This could mean a higher 5/2 than 3/2 spin state character in the QS configuration.

## 2.3.5 Spin state: EPR spectroscopy

The characterization of the most active complexes by EPR spectroscopy was performed in collaboration with Prof. Marina Bennati Group at the Max Planck Institute for Biophysical Chemistry in Göttingen (Germany).

To make a comparison with Mössbauer results, first of all EPR spectra have been collected on both isomers in solid state (lyophilized from acid conditions), at T = 4K (Figure 63). Other temperatures (20K, 70K) have been explored, but the spectra show the same signals, but lower in intensity (data not shown).

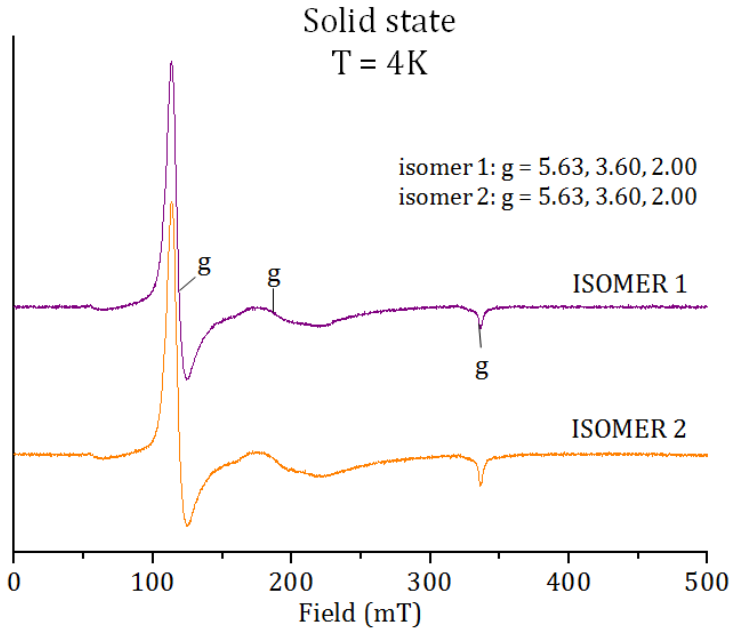


**Figure 63** EPR spectra of $Fe^{III}$-Lys9Dab(*D*)-Mimochrome VI*a* isomer 1 (purple) and 2 (orange) in solid state at T = 4K: frequency, 9.41 GHz; power, 0.1002 mW; sweep width, 5000 G; center field, 2500 G; attenuation, 33 dB; 2564 pt; 3 scans.

The EPR spectra of the two enzymes in solid states at T = 4K are almost identical, and show three signals with g = 5.63, 3.60, 2.00 (mean $g_{\perp} \approx 4.61$). Generally, for a ferric HS state a pattern of EPR signals with $g_{\perp} \approx 6$, $g_{//} \approx 2$ is expected, whereas for the ferric QS state a pattern with $4 < g_{\perp} < 6$, $g_{//} \approx 2$ is mostly reported. However, there are in literature some examples of HS and QS states with $g_{\perp}$-value lower than 6 and 4, respectively.[20–22]

By double integrating the EPR spectra, it is possible to compare the intensities of the EPR signals. The ratio of g = 5.63 to g = 2.00 signals is almost half than that expected for a HS species; this suggests that the g = 2.00 signal origins from two signals. Moreover, the intensities of the g = 5.63 and g = 3.60 signals are almost identical, and therefore, taking account of Mössbauer experiments also, the EPR spectra have to be interpreted as a superposition of HS and QS states. Finally, barley peroxidase displays a pattern of EPR signals (g = 5.36, 3.75, 1.93; mean $g_{\perp} \approx 4.56$) with g-values very similar to those of $Fe^{III}$-Lys9Dab(*D*)-Mimochrome VI*a* isomer 1 and 2, that was related to the presence of HS and QS states,[20] strengthening our assignment.

The spin states pH dependence has been explored by acquiring EPR spectra on both isomers in phosphate buffer 50 mM, 50% TFE (v/v) at different pH.

In Figure 64, the EPR spectra of $Fe^{III}$-Lys9Dab(*D*)-Mimochrome VI*a* isomer 1 and 2 at different pH at T = 4K are reported. EPR spectra of the two isomers at higher temperatures (T= 20K, 70K) have been acquired: they

display the same signals, but lower in intensity than at T= 4K (data not shown).

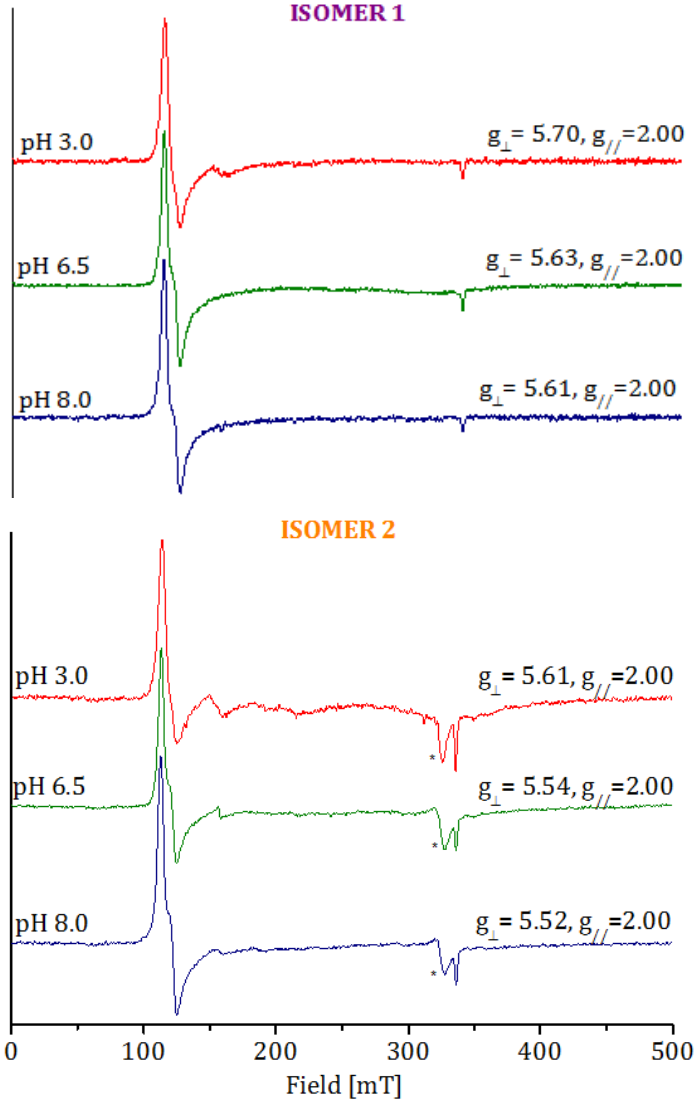


**Figure 64** EPR spectra (T= 4K) of $Fe^{III}$-Lys9Dab(*D*)-Mimochrome VI*a* isomer 1 ($7.6 \cdot 10^{-5}$ M) and 2 ($9.2 \cdot 10^{-5}$ M) in phosphate buffer 50 mM, 50% TFE (v/v), at different pH: frequency, 9.41 GHz; power, 0.1002 mW; sweep width, 5000 G; center field, 2500 G; attenuation, 33 dB;

2564 pt; 3 scans. The spectra of the isomer 1 have been blank subtracted. *cavity signal

For both isomers, the line with g = 3.60 (Figure 63) almost disappears in solution at all investigated pHs. The patterns of EPR signals shown in Figure 64 are very similar, and should be attributed to a superposition of HS and QS configurations; the $g_{\perp}$-values are higher than 5.5, indicating an higher content of HS than QS state at all investigated pHs, confirming the Mössbauer results in solution.

## 2.4 Preliminary structural analysis: NMR and CD spectroscopies on Co(III) derivatives

With the aim of structurally characterize the new compounds, the diamagnetic $Co^{III}$ ion was inserted into Lys9Dab(*D*)-Mimochrome VI*a* isomer 1 and 2 apo forms, by using $Co^{II}$-acetate, according to the literature method.[23]

The RP-HPLC profile (Figure 65) of the reaction mixture for the isomer 2 revealed the presence of two equally abundant species. A similar behavior was observed for the isomer 1. These species were separated by preparative RP-HPLC. The ESI-MS analysis reveals that they have the same molecular weight (Figure 66-67); the UV-Vis spectra are almost identical (Figure 68) and are characteristic of a $Co^{III}$-porphyrin complex with a mono-His axial coordination.

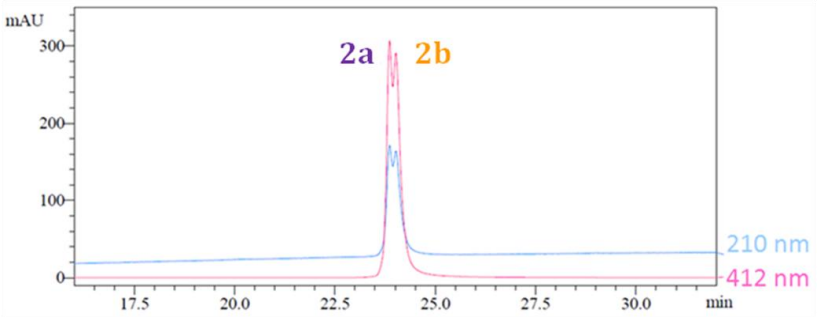


**Figure 65** RP-HPLC profile of $Co^{III}$-Lys9Dab(*D*)-Mimochrome VI*a* isomer 2.

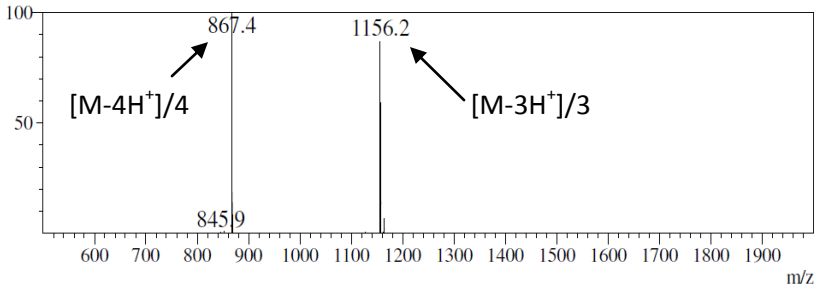


**Figure 66** ESI-MS spectrum of pure $Co^{III}$-2Aib1Dab-MimoVI isomer 2, 2a species. The mass spectrum was in agreement with the expected mass (calculated mass: 3466.46 Da; experimental mass: 3465.6 ± 0.7 Da).

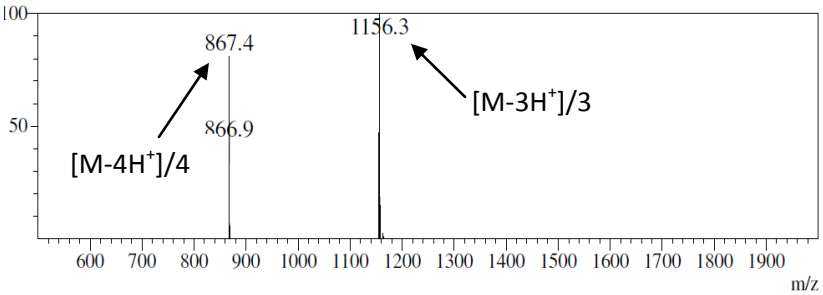


**Figure 67** ESI-MS spectrum of pure $Co^{III}$-2Aib1Dab-MimoVI isomer 2, 2b species. The mass spectrum was in agreement with the expected mass (calculated mass: 3466.46 Da; experimental mass: 3465.7 ± 0.8 Da).

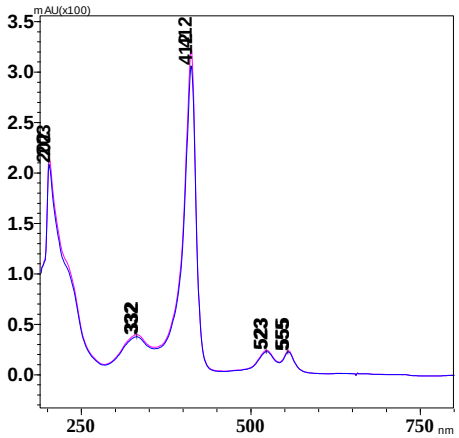


**Figure 68** Overlap of the UV-Vis spectra of the two species.

As a preliminary characterization, the species derived from the isomer 2, named 2a and 2b, were individually analyzed by Nuclear Magnetic Resonance (NMR) and CD spectroscopies, in $H_2O$/TFE 60/40 (v/v).

$^1H$ NMR spectra in the low and high field regions are reported in Figure 69; the spectrum of $Co^{III}$-Mimochrome VI is also shown for comparison.

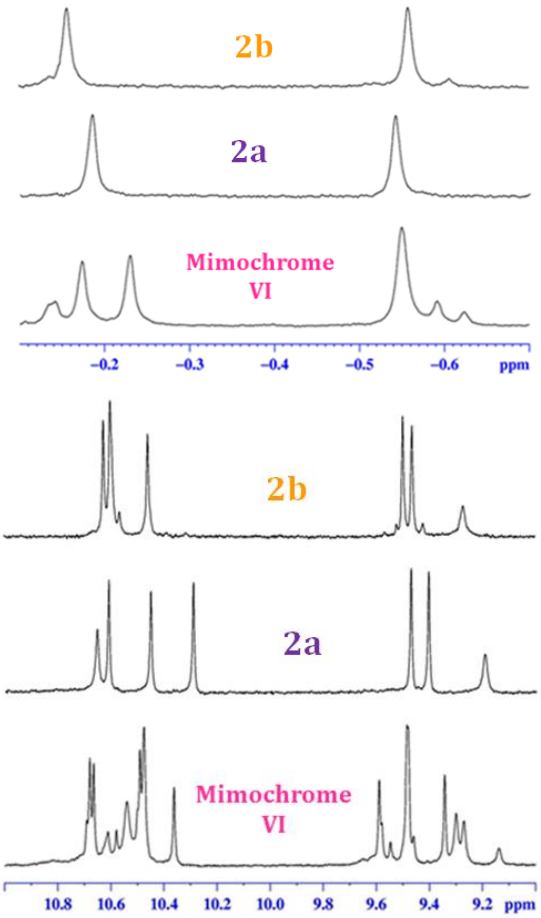


**Figure 69** $^1H$ NMR spectra of $Co^{III}$-Lys9Dab(*D*)-Mimochrome VI*a* 2a and 2b in the high field (top) and low field (bottom) regions compared to that of $Co^{III}$-Mimochrome VI.

The signals showed in Figure 69 (top) were unequivocally assigned to the δ- and ε-CH imidazole protons of the coordinating histidine, that experience an extremely large ring current effect and therefore appear in the high field region of the spectrum.
The signals in the low field region (Figure 69, bottom) were identified as the four *meso* CH protons (5H, 10H, 15H, 20H), the two pyrrolic NH protons (8H, 13H) and the imidazole δ-NH proton of the coordinating histidine.
Only one set of resonances for the deuteroporphyrin protons was observed, in contrast to the $^{1}H$ NMR spectrum of the prototype, $Co^{III}$-Mimochrome VI, which displays a more complex spectrum indicative of the presence of multiple species in solution.

The CD spectra in the Soret region of $Co^{III}$-Lys9Dab(*D*)-Mimochrome VI*a* 2a and 2b in the same conditions of the NMR experiment ($H_2O$/TFE 60/40, v/v), are reported in Figure 70.
The 2a species displays a strong negative induced Cotton effect, centred at 408 nm, whereas the 2b species displays a strong positive induced Cotton effect, centred at 409 nm.

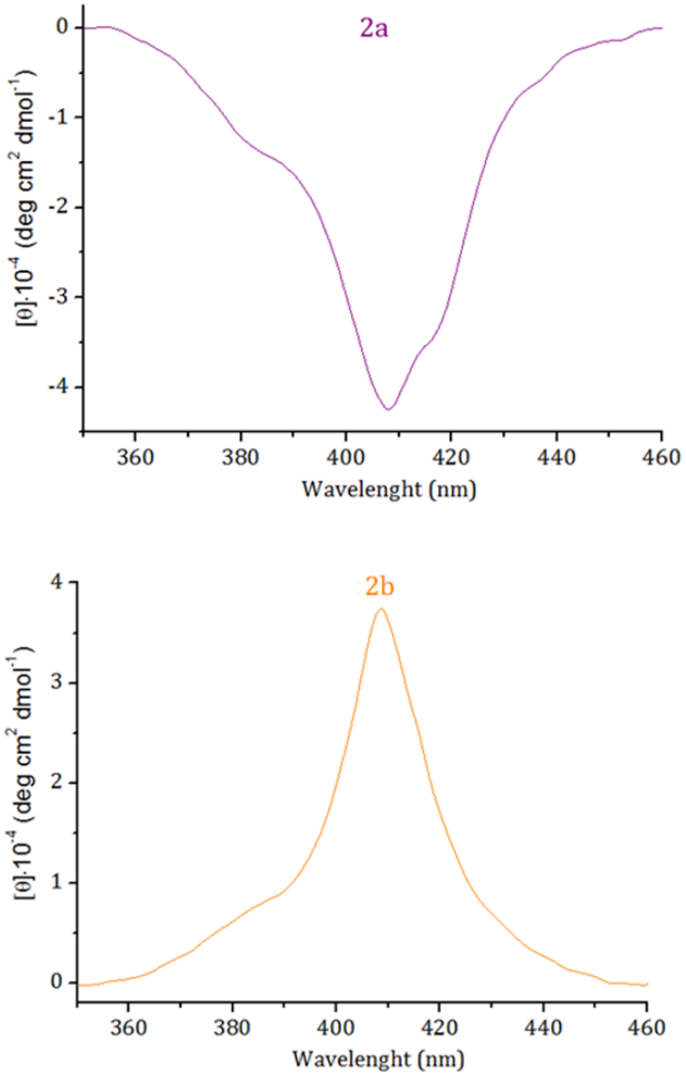


**Figure 70** CD spectra in the Soret region of $Co^{III}$-Lys9Dab(*D*)-Mimochrome VI*a* 2a ($1.4 \cdot 10^{-5}$ M) and 2b ($2.4 \cdot 10^{-5}$ M) in $H_2O$/TFE 60/40 (v/v).

## 2.5 Discussion

The new developed Mimochrome VI*a* generation has been designed with the aim of stabilizing the three-dimensional sandwich structure, typical of Mimochromes, while preserving or enhancing functionality. The introduction of Aib residues on the decapeptide chain allowed the identification and separation of two regioisomers for each new analogue, demonstrating the role of Aib residues as structural constraints.

The functional characterization proved that all the new analogues posses increased peroxidase-like activity and stability toward bleaching, with respect to the prototype, $Fe^{III}$-Mimochrome VI, and $Fe^{III}$-Mimochrome VI first generation of analogues (Figure 71).
Among the new Mimochromes, the highest T.O.N. ($10 \cdot 10^3$) was found for Mimochrome VI*a* and Lys9Dab(*D*)-Mimochrome VI*a* isomers 2, whose deuteroporphyrin-decapeptide linker contain, respectively, four and two methylenic groups; a lower T.O.N. ($8.3 \cdot 10^3$) was found for Lys9Orn(*D*)-Mimochrome VI*a* isomers 1 and 2 (three methylenic groups in the deuteroporphyrin-decapeptide linker), suggesting the presence of an even-odd effect. Moreover, Mimochrome VI*a* and Lys9Dab(*D*)-Mimochrome VI*a* isomers 2 display a slightly higher T.O.N. ($10 \cdot 10^3$) with respect to the isomers 1 ($9.1 \cdot 10^3$), suggesting that the methyl positions on the deuteroporphyrin respect to the peptide chain influence the stability.

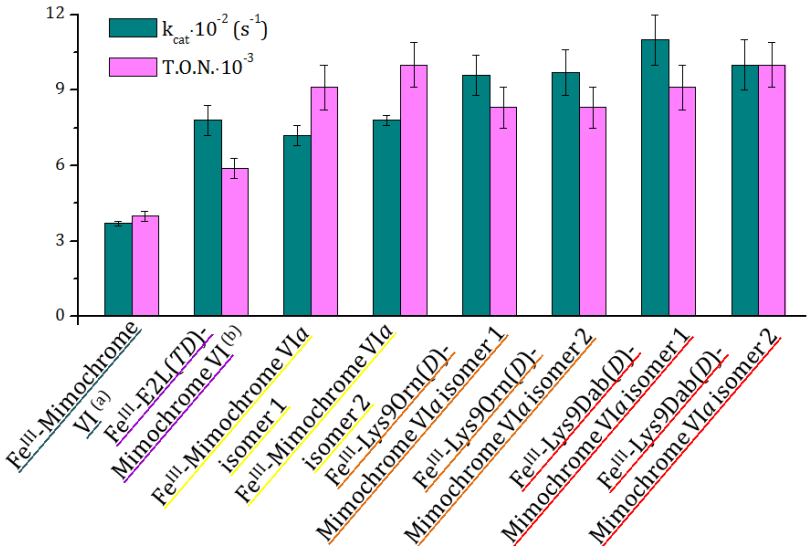


**Figure 71** Catalytic constants and T.O.N.s of: Fe$^{III}$-Mimochrome VI, Fe$^{III}$-E2L(*TD*)-Mimochrome VI (the best catalyst of the first generation of Mimochrome VI analogues), and all the new developed Mimochromes. Error bars are reported. (a) Data from reference 6. (b) Data from reference 1.

The decrease in the deuteroporphyrin-decapeptide linker length is accompanied by an increase in the apparent catalytic constant (Figure 71). This result confirmed the correctness of the asymmetric Mimochrome design for catalytic purposes and highlight that this simple scaffold is well-suited for point amino acid substitutions. The catalytic constant of Fe$^{III}$-Lys9Dab(*D*)-Mimochrome VI*a* isomers 1 and 2 are 3-fold higher than that of Fe$^{III}$-Mimochrome VI, and only 6-fold lower than that of HRP, the natural model of reference, under the experimental conditions for maximal activity of each enzyme.

The pH-dependence reactivity of Fe$^{III}$-Lys9Dab(*D*)-Mimochrome VI*a* isomers 1 and 2 (Figure 35) is similar to

that found for $Fe^{III}$-Mimochrome VI and its first generation of analogues.[1,6] In all cases, data fitting of $v_0$ *vs.* pH, according to model equation described elsewhere,[6] gave $pKa_1 \approx 5$ and $pKa_2 \approx 8$, with the maximum activity at pH ≈ 6.5. This indicates that at least two ionizable groups are involved in the modulation of the reactivity. In a previous publication,[1] we proposed that the first transition is due to the deprotonation of the Glu2 on the decapeptide chain, which then could ion-pair with the Arg10 on the tetradecapeptide chain, stabilizing the sandwich structure and positively influence the catalytic properties. The decreasing activity to increasing pHs from 6.5 to 8.0, can be attributed to an higher molar fraction of the enzyme complex in the His/$OH^-$ iron axial coordination form. In fact, the optical transition observed in the UV/Vis pH titration with midpoint at pH ≈ 7 for both isomers, has been attributed to a ligand exchange from water to the harder hydroxide ion (Figure 36-37). This ligand exchange, occurring at the distal site above pH 6.5, interferes with the $H_2O_2$ binding and catalysis triggering, causing a decrease in efficiency.

UV-Vis pH titration data of $Fe^{III}$-Lys9Dab(*D*)-Mimochrome VI*a* isomer 2 were used to describe the three pH-dependent species (Figure 72). At pH 3.0, the mainly HS $H_2O$/$H_2O$ iron axial coordination species is predominant. A second species is also present at about 12%, reaching the maximum concentration at pH 5.4. It corresponds to a predominantly HS His-$H_2O$ iron axial coordination form. Increasing the pH, another species appears, in which the harder hydroxide ligand, in place of the water molecule, binds the ferric ion.

At pH 6.5, the molar fraction of the active form (His/$H_2O$) is 68%, whereas the contribution of the $H_2O/H_2O$ form is negligible (<0.2%).

Although the first transition of $Fe^{III}$-Lys9Dab(*D*)-Mimochrome VI*a* isomer 1 cannot be determined, we presume that it most likely happens at pH lower than 4 (Figure 36). Thus, we can deduce that the contribution of the possible $H_2O/H_2O$ form is, also in this case, negligible. Therefore, the molar fraction of the active form (His/$H_2O$) at pH 6.5 for the isomer is 72%; this higher value could explain the slight difference in the apparent catalytic constants values between the two isomers.

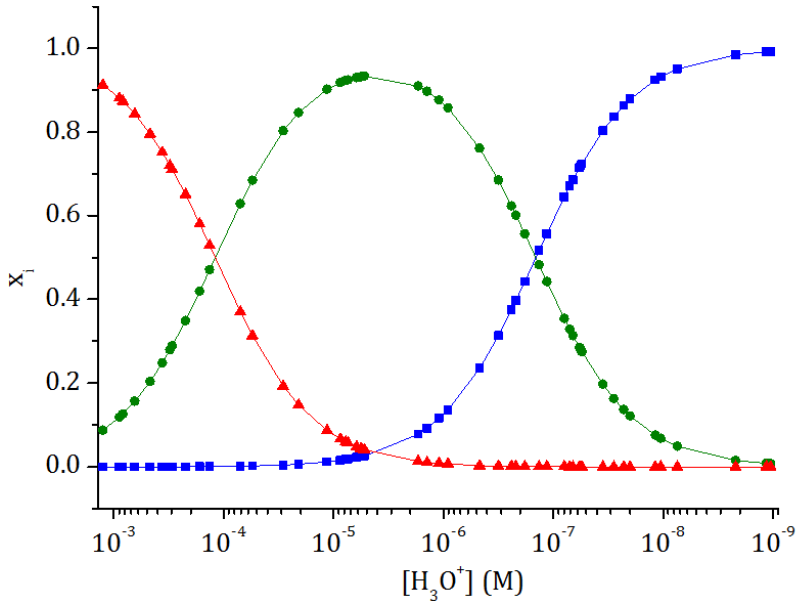


**Figure 72** Speciation curves as a function of pH of $Fe^{III}$-Lys9Dab(*D*)-Mimochrome VI*a* isomer 2 (data from UV-Vis pH titration in Figure 37).

All Mimochromes showed their peptide secondary structure strictly related to the presence of the co-solvent TFE.[6,24–27] In particular, the TFE-dependent peptides

structure of $Fe^{III}$-Mimochrome VI was nicely correlated to its catalytic performances, thus demonstrating that the correct folding of both chains is essential for reactivity.[6] The α-helix content of $Fe^{III}$-Lys9Dab(*D*)-Mimochrome VI*a* isomers 1 and 2 increases in the presence of TFE, as shown by far-UV CD data (Figure 38-46). The α-helix conformation is reached upon addition of ≈ 30% TFE (v/v) at all investigated pHs.

In the Soret region, at pH 5.0 a negative induced Cotton effect was found in the CD spectra (Figure 47, 52) for both isomers. At pH 6.5 and without the co-solvent TFE, an overall *S*-shaped CD spectrum was observed for both isomers (Figure 48, 53). At pH 9.0 a very weak Cotton effect was found for both isomers.

Molecules characterized by enantiomeric orientations of the peptide chains with respect to the deuteroporphyrin ring may induce opposite-sign Cotton effects into the Soret region.

It has been widely reported that the protein folding around the heme chromophore is the main factor inducing optical activity in the Soret transition for heme-protein.[28] Because of the mutual orientation of the heme and the protein, an induced Cotton effect may result from a coupling of π-π* heme transition with π-π* and n-π* transitions localized in the polypeptide backbone or π- π* transitions of aromatic sidechains.

Theoretical studies have shown that the shape of the heme π-π* Cotton effects depends upon the direction of polarization of the Soret components in the heme plane. However, the shape and the complexity of the Soret-Cotton

effect cannot be easily related to the protein conformation and structural organization.[24]

The splitting into two opposite bands of the CD Soret band (S-shaped) that appears for both isomers at pH 6.5 and 9.0 can be related to the presence of two isomers. Different positions of the maxima, different shapes, and different intensities in the Soret-region Cotton effect of the diastereomeric forms may give an overall S-shaped spectrum. Further, the S-shaped spectrum can also be characteristic of exciton splitting resulting from heme-heme interaction.[28]

CD in the far-UV region proved that the α-helix content in both isomers increases in the presence of TFE; CD in the Soret region proved that the induced Cotton effect also increases at increasing TFE content (Figure 47-55), suggesting that the stabilization of the secondary structure facilitates *inter*-chains and peptide-heme interactions. This mutual correlation between the secondary and the tertiary structure has been investigated (Figure 73).

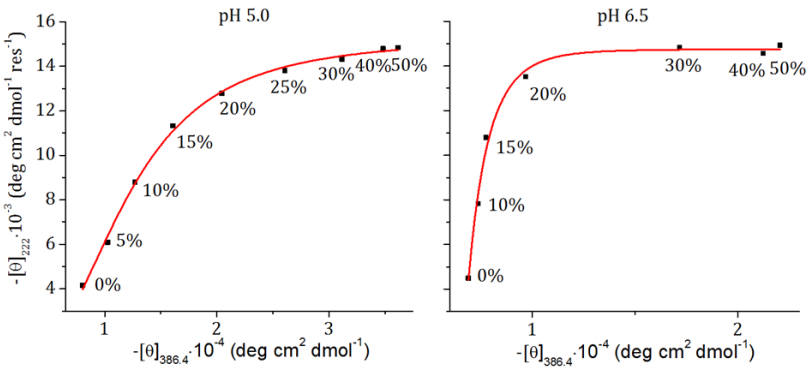


**Figure 73** Plot of $[\theta]_{222}$ as function of $[\theta]_{386.4}$ at different TFE concentrations (%, v/v) at pH 5.0 and 6.5 for $Fe^{III}$-Lys9Dab(*D*)-Mimochrome VI*a* isomer 1. $[\theta]_{386.4}$ is reported as molar ellipticity,

whereas $[\theta]_{222}$ as mean residue ellipticity. Tags refer to the TFE concentration (%, v/v).

Two different slopes in the range 0-20% and 20-50% TFE (v/v) were observed at pH 5.0 and pH 6.5 for both isomers (data of isomer 1 in Figure 73, as an example), indicating the occurrence of two different phenomena. With the assumption that the induced Cotton effect may result from a coupling of π-π* heme transition with n-π* and π-π* transitions of the polypeptide backbone, it is reasonable to hypothesize that the increase in intensity of the Soret-induced Cotton effect at TFE concentration up to 20% is related to the increase in helical content (Figure 73). At TFE concentrations higher than 20%, the helical content slightly increases, whereas the intensity of the induced Cotton effect largely increases. This confirmed the effectiveness of the *inter*-helical interactions in reinforcing the sandwich structure and in driving the peptide chains to fold into a unique topology around the heme.

Mössbauer and EPR results in solid state (Figure 56-57 and 63, Table 13) and in solution (Figure 61-62 and 64, Table 14) show that $Fe^{III}$-Lys9Dab(*D*)-Mimochrome VI*a* isomer 1 and 2 a mixture of two spin states: high spin (S=5/2) and quantum-mechanical admixed spin (S=3/2, 5/2). These two spin state are in 1:1 ratio in solid state, whereas a predominant HS state was found in solution.
The QS state is very rare in nature, and is a distinctive characteristic of the class III heme peroxidases of the plant peroxidase superfamily.[29] Among them, it has been only observed, mixed with other spin state species, in Horseradish Peroxidase A1, A2, C,[30] in Soybean

Peroxidase[31] and in Barely Peroxidase.[32] HRP C samples, at physiological pH, are mixtures of QS and HS states, with relative populations dependent upon the particular purification procedure used; *in situ*, HRP C has roughly equal proportions of QS and HS configurations.[18] Therefore, UV-Vis, and Mössbauer and EPR results proved that the iron (III) coordination environment of $Fe^{III}$-Lys9Dab(*D*)-Mimochrome VI*a* isomer 1 and 2 is similar to that of the Horseradish Peroxidase, our natural model of reference, confirming the correctness of the design.

The proton NMR spectra of $Co^{III}$-Lys9Dab(*D*)-Mimochrome VI*a* 2a and 2b reveal the presence of one deuteroporphyrin species, in contrast to what observed in the proton NMR spectrum of the prototype, $Co^{III}$-Mimochrome VI (Figure 69). This result lays the basis for the complete structural determination by NMR. Moreover, CD spectra of $Co^{III}$-Lys9Dab(*D*)-Mimochrome VI*a* 2a and 2b display, respectively, strong negative and positive induced Cotton effects, both centred at ≈ 409 nm (Figure 70). In $Co^{III}$-Mimochrome I, the negative Cotton effect was attributed to the Δ isomer, whereas the positive Cotton effect to the Λ isomer;[25] this suggests that $Co^{III}$-Lys9Dab(*D*)-Mimochrome VI*a* 2a and 2b could also correspond, respectively, to the Δ and Λ isomers. If the structural determination confirmed our hypothesis, this would be the first isolation of the Δ and Λ isomers in a *penta*-coordinated complex.

## References


(1) Vitale, R.; Lista, L.; Cerrone, C.; Caserta, G.; Chino, M.; Maglio, O.; Nastri, F.; Pavone, V.; Lombardi, A. *Org Biomol Chem* **2015**. DOI:10.1039/c5ob00257e

(2) Schweitzer-Stenner, R.; Gonzales, W.; Bourne, G. T.; Feng, J. A.; Marshall, G. R. *J. Am. Chem. Soc.* **2007**, *129* (43), 13095–13109.

(3) Improta, R.; Rega, N.; Aleman, C.; Barone, V. *Macromolecules* **2001**, *34* (21), 7550–7557.

(4) Karle, I. L.; Balaram, P. *Biochemistry (Mosc.)* **1990**, *29* (29), 6747–6756.

(5) Rohl, C. A.; Doig, A. J. *Protein Sci.* **1996**, *5* (8), 1687–1696.

(6) Nastri, F.; Lista, L.; Ringhieri, P.; Vitale, R.; Faiella, M.; Andreozzi, C.; Travascio, P.; Maglio, O.; Lombardi, A.; Pavone, V. *Chem. - Eur. J.* **2011**, *17* (16), 4444–4453.

(7) Childs, R. E.; Bardsley, W. G. *Biochem. J.* **1975**, *145* (1), 93–103.

(8) Rodriguez-Lopez, J. N.; Smith, A. T.; Thorneley, R. N. *J. Biol. Chem.* **1996**, *271* (8), 4023–4030.

(9) Munro, O. Q.; Marques, H. M. *Inorg. Chem.* **1996**, *35* (13), 3752–3767.

(10) Yonetani, T.; Anni, H. *J. Biol. Chem.* **1987**, *262* (20), 9547–9554.

(11) Feis, A.; Marzocchi, M. P.; Paoli, M.; Smulevich, G. *Biochemistry (Mosc.)* **1994**, *33* (15), 4577–4583.

(12) Urry, D. W.; Pettegrew, J. W. *J. Am. Chem. Soc.* **1967**, *89* (20), 5276–5283.

(13) Goodman, M.; Listowsky, I.; Masuda, Y.; Boardman, F. *Biopolymers* **1963**, *1* (1), 33–42.

(14) Nelson, J. W.; Kallenbach, N. R. *Proteins Struct. Funct. Bioinforma.* **1986**, *1* (3), 211–217.

(15) Jasanoff, A.; Fersht, A. R. *Biochemistry (Mosc.)* **1994**, *33* (8), 2129–2135.

(16) Greenfield, N. J.; Fasman, G. D. *Biochemistry (Mosc.)* **1969**, *8* (10), 4108–4116.

(17) Debrunner, P. G.; Lever, A. B. P.; Gray, H. B. *Phys. Bioinorg. Chem. Ser. VCH* **1989**.

(18) Maltempo, M. M.; Moss, T. H. *Q. Rev. Biophys.* **1976**, *9* (02), 181–215.

(19) Burger, B.; Demeshko, S.; Bill, E.; Dechert, S.; Meyer, F. *Angew. Chem. Int. Ed.* **2012**, *51* (40), 10045–10049.

(20) Howes, B. D.; Schiodt, C. B.; Welinder, K. G.; Marzocchi, M. P.; Ma, J. G.; Zhang, J.; Shelnutt, J. A.; Smulevich, G. *Biophys. J.* **1999**, *77* (1), 478–492.

(21) Chouchane, S.; Girotto, S.; Kapetanaki, S.; Schelvis, J. P.; Yu, S.; Magliozzo, R. S. *J. Biol. Chem.* **2003**, *278* (10), 8154–8162.
(22) Kintner, E. T.; Dawson, J. H. *Inorg. Chem.* **1991**, *30* (26), 4892–4897.
(23) Buchler, J.W.,. In *The Porphyrins, Volume 1*; David Dolphin, Series Ed.; NY, USA, 1979; Vol. I, pp 389–483.
(24) Nastri, F.; Lombardi, A.; Morelli, G.; Maglio, O.; D'Auria, G.; Pedone, C.; Pavone, V. *Chem. - Eur. J.* **1997**, *3* (3), 340–349.
(25) D'Auria, G.; Maglio, O.; Nastri, F.; Lombardi, A.; Mazzeo, M.; Morelli, G.; Paolillo, L.; Pedone, C.; Pavone, V. *Chem. - Eur. J.* **1997**, *3* (3), 350–362.
(26) Lombardi, A.; Nastri, F.; Sanseverino, M.; Maglio, O.; Pedone, C.; Pavone, V. *Inorganica Chim. Acta* **1998**, *275-276*, 301–313.
(27) Costanzo, L.; Geremia, S.; Randaccio, L.; Nastri, F.; Maglio, O.; Lombardi, A.; Pavone, V. *JBIC J. Biol. Inorg. Chem.* **2004**, *9* (8), 1017–1027.
(28) Myer, Y. P. *Methods Enzymol.* **1978**, *54*, 249–284.
(29) Indiani, C.; Feis, A.; Howes, B. D.; Marzocchi, M. P.; Smulevich, G. *J. Am. Chem. Soc.* **2000**, *122* (30), 7368–7376.
(30) Feis, A.; Howes, B. D.; Indiani, C.; Smulevich, G. *J. Raman Spectrosc.* **1998**, *29* (10-11), 933–938.
(31) Nissum, M.; Feis, A.; Smulevich, G. *Biospectroscopy* **1998**, *4* (6), 355–364.
(32) Indiani, C.; Feis, A.; Howes, B. D.; Marzocchi, M. P.; Smulevich, G. *J. Inorg. Biochem.* **2000**, *79* (1-4), 269–274.

# Chapter III
# Conclusions

# Conclusions

The research project here reported is focused on the rational design, synthesis, and characterization of a new class of mini-enzymes. These compounds belong to a family of covalent heme-peptide models developed by the Artificial Metallo-Enzyme Group of Naples: Mimochromes.[1–8] Over the years, several models have been developed, up to $Fe^{III}$-Mimochrome VI,[7] a *penta*-coordinated complex which catalyzes the oxidation of reducing substrates by activating the "clean" oxidant hydrogen peroxide. The molecular scaffold of $Fe^{III}$-Mimochrome VI was used to introduce point substitutions in the peptide sequences in order to stabilize a unique species with improved catalytic functionality.

These substitutions were introduced on the decapeptide chain, since it most likely experiences the higher conformational freedom, due to the lack of the coordinating histidine, that firmly anchors the tetradecapeptide chain on the heme. The Aib, a natural, non-coded amino acid, with a very high helical propensity,[9,10] was introduced in 3 and 7 positions of the decapeptide chain, obtaining a new molecule, named Mimochrome VI*a*. In the next stage of design, a systematic evaluation of the linker length between the porphyrin and the decapeptide chain was carried out. To further stabilize the sandwich structure, the linker length was progressively decreased: Lys at position 9 was substituted with Orn and with Dab, whose side chains contain, respectively, one and two methylenic group less than lysine side chain. Thus, two new molecules were

obtained, named, respectively, Lys9Orn(*D*)-Mimochrome VI*a* and Lys9Dab(*D*)-Mimochrome VI*a*.

The Aib introduction allowed to separate two regioisomers for each compound, due to the coupling of the decapeptide to the propionic group at 2 position and of the tetradecapeptide at 18 position of the deuteroporphyrin, and vice versa. These two regioisomers, named isomer 1 and 2, were isolated and the metal was individually inserted into these two species.

The functional screening of the new class of Mimochromes highlighted that:

- introducing Aib residues increases the stability toward bleaching, as shown by the higher turnover number;
- decreasing the decapeptide-porphyrin linker length increases the catalytic activity.

Therefore, $Fe^{III}$-Lys9Dab(*D*)-Mimochrome VI*a* isomer 1 and 2 have been selected as the best enzymes, in terms of catalytic activities and turnover number. While being more than tenfold smaller in terms of molecular weight, $Fe^{III}$-Lys9Dab(*D*)-Mimochrome VI*a* isomer 1 and 2 display improved enzyme-like properties, that in turn approach HRP, the natural parent enzyme.

The maximum activity of the new Aib-containing Mimochromes is at about neutral pH (6.5), and this represents an important outcome, since the maximum activity of HRP is at acidic pH (4.6). It should be outlined that pH 6.5 does not represent the optimal pH for the presence of the catalytically active His-$H_2O$ species (molar fraction 72% for the isomer 1 and 68% for the isomer 2 at

pH 6.5). Considering that the two isomers of $Fe^{III}$-Lys9Dab(*D*)-Mimochrome VI*a* lack a residue in the active site able to assist the hydrogen peroxide deprotonation similar to His42 in HRP,[11–13] pH 6.5 could represent a compromise, which simultaneously ensures the highest amount of His-$H_2O$ coordination state and hydrogen peroxide deprotonation.

UV-Vis, CD, EPR and Mössbauer spectroscopies were used in combination to gain insight into the molecular basis of the catalytic improvement, correlating the primary, secondary and tertiary structures of the new mini-enzymes with the spin state of the metal ion and the nature of the axial ligands. It was demonstrated that the iron(III) coordination environment is similar to that of the Horseradish Peroxidase, the natural parent enzyme.

NMR spectroscopy on the cobalt (III) complex of Lys9Dab(*D*)-Mimochrome VI*a* isomer 2 proved that the improvement in the catalytic properties is accompanied by an improvement in the structural properties, since its NMR spectrum displays a unique species, in contrast with the NMR spectrum of the prototype, $Co^{III}$-Mimochrome VI, which displays a more complex spectrum indicative of the presence of multiple species in solution. The complete structural determination by NMR of $Co^{III}$- Lys9Dab(*D*)-Mimochrome VI*a* isomer 2 is in progress.

Collectively, the results allow us to point out that Mimochromes scaffold holds essential elements to finely tune the reactivity. This represents a very important checkpoint for the rational design of new and improved bio-mimetic catalysts, tailored for specific applications.

Further design, based on the results herein reported, will be aimed to: (*i*) favour the His-$H_2O$ species over a wider pH range; (*ii*) introduce amino acid residues assisting the acid–base catalytic cleavage of the O–O bond, as His42 acts in HRP.[11–13]

Recently, an intriguing biotechnological application of the heme-protein model here described has been explored. On the basis of its high peroxidase-like catalytic activity and its small dimensions (3.5 kDa) compared to natural protein, $Fe^{III}$-Lys9Dab(*D*)-Mimochrome VI*a* has been proposed as reporter enzyme in Enzyme-linked immunosorbent assays (ELISA). The ELISA test relies on immunocomplex formation, between an antigen and a specific antibody. The detector system is an enzyme (HRP often)[12] covalently bound to the antibody; a colorimetric signal from the enzymatic reaction allows to quantify immunocomplexes. The ELISA test has the advantage of being very simple and cheap, but sometimes it is little sensitive, with a high number of false-positives. The replacement of the natural HRP with the mini heme-enzyme here described, has allowed to considerably increase the conjugation ratio enzyme/antibody. This should allow us to develop devices with a high sensitivity detection of analytes in samples of different nature, even at low concentrations, offering economic benefits and high performance.

This project was proposed in “InKidia” business idea and received one of the first two Tech Hub 2015 prizes, for the foundation of new Start Up Companies.

## References


(1) Nastri, F.; Lombardi, A.; Morelli, G.; Maglio, O.; D'Auria, G.; Pedone, C.; Pavone, V. *Chem. - Eur. J.* **1997**, *3* (3), 340–349.

(2) D'Auria, G.; Maglio, O.; Nastri, F.; Lombardi, A.; Mazzeo, M.; Morelli, G.; Paolillo, L.; Pedone, C.; Pavone, V. *Chem. - Eur. J.* **1997**, *3* (3), 350–362.

(3) Lombardi, A.; Nastri, F.; Pavone, V. *Chem. Rev.* **2001**, *101* (10), 3165–3189.

(4) Geremia, S.; Di Costanzo, L.; Randaccio, L.; Lombardi, A.; Pavone, V.; Campagnolo, M. *Acta Cryst* **2002**, *58*, C277.

(5) Costanzo, L.; Geremia, S.; Randaccio, L.; Nastri, F.; Maglio, O.; Lombardi, A.; Pavone, V. *JBIC J. Biol. Inorg. Chem.* **2004**, *9* (8), 1017–1027.

(6) Lombardi, A.; Nastri, F.; Marasco, D.; Maglio, O.; De Sanctis, G.; Sinibaldi, F.; Santucci, R.; Coletta, M.; Pavone, V. *Chem. - Eur. J.* **2003**, *9* (22), 5643–5654.

(7) Nastri, F.; Lista, L.; Ringhieri, P.; Vitale, R.; Faiella, M.; Andreozzi, C.; Travascio, P.; Maglio, O.; Lombardi, A.; Pavone, V. *Chem. - Eur. J.* **2011**, *17* (16), 4444–4453.

(8) Vitale, R.; Lista, L.; Cerrone, C.; Caserta, G.; Chino, M.; Maglio, O.; Nastri, F.; Pavone, V.; Lombardi, A. *Org Biomol Chem* **2015**. DOI:10.1039/c5ob00257e

(9) Schweitzer-Stenner, R.; Gonzales, W.; Bourne, G. T.; Feng, J. A.; Marshall, G. R. *J. Am. Chem. Soc.* **2007**, *129* (43), 13095–13109.

(10) Improta, R.; Rega, N.; Aleman, C.; Barone, V. *Macromolecules* **2001**, *34* (21), 7550–7557.

(11) Poulos, T. L.; Kraut, J. *J. Biol. Chem.* **1980**, *255* (17), 8199–8205.

(12) Azevedo, A. M.; Martins, V. C.; Prazeres, D. M. F.; Vojinović, V.; Cabral, J. M. S.; Fonseca, L. P. In *Biotechnology Annual Review*; Elsevier, 2003; Vol. 9, pp 199–247.

(13) Veitch, N. C. *Phytochemistry* **2004**, *65* (3), 249–259.

# Chapter IV
# Materials and Methods

## 4.1 Materials

Peptide synthesis was carried out using reagent grade anhydrous solvents. All the solvents adopted in the LC and LC-MS analysis, in the purifications, and in the solutions for the spectroscopic characterizations were HPLC or higher grade solvents, and were provided by Romil.

Scavengers (EDT, TIS, TES) and TFE were supplied by Sigma Aldrich; TFA and DIEA were from Applied Biosystem; acetic anhydride was from Fluka and piperidine was from Merck. DMF, DCM, NMP, HFIP, ethanol and methanol were supplied by Romil. All reagents were used without further purification.

The NovaSyn® TG Sieber resin (substitution level 0.61 mmol/g) and all the N-α-Fmoc amino acids were purchased from NovaBiochem; activating HOBt, HATU and PyBop were provided by LC Sciences, Anaspec and NovaBiochem, respectively.

Deuteroporphyrin IX was from Porphyrin Products. Cobalt (II) acetate and iron (II) acetate were purchased from Sigma Aldrich.

Precoated silica G-60 plates, F254, purchased from Merck, were used for thin-layer chromatography (TLC).

Phosphate salts (monobasic and dibasic) for buffers preparation were provided by Fluka.

Solvent mixtures are indicated in the respective sections.

## 4.2 Instrumentations

Protected peptides were obtained by the use of ABI 433 automatic peptide synthesizer.

HPLC and LC-MS analysis were performed with a Shimadzu LC-10ADvp equipped with an SPDM10Avp diode-array detector. ESI-MS spectra were recorded on a Shimadzu LC-MS-2010EV system with ESI interface, and Shimadzu LC-MS solution Workstation software for data processing. A Q-array-octapole-quadrupole mass analyzer was used as detector. The optimized MS parameters were selected as followed: curved desolvation line (CDL) temperature 250°C; block temperature 250°C; probe temperature 250°C; detector gain 1.6 kV; probe voltage +4.5 kV; CDL voltage -15 V. Nitrogen served as nebulizer gas (flow rate: 1.5 $L \cdot min^{-1}$).

Preparative Flash Chromatography purifications were performed using a Biotage ISOLERA flash purification system, ISO-1SW model, equipped with a diode-array detector.

Preparative HPLC purifications were performed with a Shimadzu LC-8A equipped with an SPD-10A detector.

UV-Vis and CD analysis were performed on Cary Varian 50 Probe UV Spectrophotometer and Jasco J-715 dichrograph, respectively.

Mössbauer spectra were recorded using an alternating constant acceleration WissEL Mössbauer spectrometer consisting of a MR 360 Drive Unit, a MVT-1000 velocity transducer and a LND 45431 proportional counter

mounted on a LINOS precision bench. The Mössbauer system is equipped with a with a $^{57}Co$ source in a Rh matrix with an initial activity of 1.85~GBq (kept at room temperature) and is operated in horizontal transmission geometry with source, absorber and detector in a linear arrangement. A Janis SHI 850 closed-cycle helium cryostat was used for low temperature measurements down to 6 K. Data acquisition was performed using a 512 channel analyzer. Isomer shifts are given relative to α-iron metal at ambient temperature. Simulation and evaluation of the experimental data was performed using the Mfit program (E. Bill, Max-Planck Institute for Bioinorganic Chemistry, Mülheim/Ruhr, Germany).

EPR spectroscopic measurements were carried out using a Bruker Elexsys E500 CW-EPR and a Super-X microwave bridge operating at 9.3–9.5 GHz. The spectrometer was equipped with a standard Bruker X-band ER4119-SHQE cavity and a liquid helium cryostat (Oxford Instruments).

NMR spectra were acquired at 298K on a Bruker Avance 600 Spectrometer, equipped with a triple resonance cryo-probe. Suppression of the water signal was accomplished by excitation sculpting sequence.

The molecular graphics pictures were generated with PyMOL software (DeLano Scientific ltd)[1] and VMD software (Visual Molecular Dynamics)[2].

Data analysis was made by using Origin Pro8 and Kaleidagraph softwares.

## 4.3 Solid-phase synthesis of peptides

All protected peptides were synthesized by using an automatic peptide synthesizer (see instrumentations), with Fmoc strategy, on a 0.25 mmol scale, using a super acid labile resin, the NovaSyn® TG Sieber (substitution level 0.61 mmol/g).
The following four peptides were synthesized:

- Tetradecapeptide (*TD*): Ac-Asp-Leu-Gln-Gln-Leu-His-Ser-Gln-Lys-Arg-Lys-Ile-Thr-Leu-$NH_2$;
- Decapeptide (*D*): Ac-Asp-Glu-Aib-Gln-Leu-Ser-Aib-Gln-Lys-Arg-$NH_2$;
- Lys9Orn(*D*): Ac-Asp-Glu-Aib-Gln-Leu-Ser-Aib-Gln-Orn-Arg-$NH_2$;
- Lys9Dab(*D*): Ac-Asp-Glu-Aib-Gln-Leu-Ser-Aib-Gln-Dab-Arg-$NH_2$.

For the synthesis of the peptides, the amino acids used are reported as follows: Fmoc-Asp(OtBu)-OH; Fmoc-Leu-OH; Fmoc-Gln(Trt)-OH; Fmoc-His(Trt)-OH; Fmoc-Ser(tBu)-OH; Fmoc-Lys(Mmt)-OH; Fmoc-Arg(Pbf)-OH; Fmoc-Lys(Boc)-OH; Fmoc-Ile-(OH); Fmoc-Thr(tBu)-OH; Fmoc-Glu(OtBu)-OH; Fmoc-Aib-OH; Fmoc-Orn(Mtt)-OH; Fmoc-Dab(Mtt)-OH.
Once removed the Fmoc group from the resin, deprotection, coupling and capping steps were cyclically repeated with each amino acid, until the chain assembly was completed.[3] At the end of the synthesis, the peptides, amidated at the C-termini, were finally acetylated at the N-

termini with $Ac_2O$/HOBt/DIEA solution in NMP.

The steps performed in the synthetic procedure can be summarized as follows:

1. Deprotection: Fmoc group was removed with a 20% piperidine solution in NMP. After Fmoc deprotection, a NMP washing step was performed.
2. Activation: the carboxyl group of each Fmoc-amino acid was activated by direct addition in the cartridge of 1 equivalent of PyBop. HATU was used for difficult couplings.
3. Coupling: the pre-activated Fmoc-amino acid reacted with the free amino-terminal group of the growing peptide chain on the resin in NMP.
4. Capping: this reaction was performed after each coupling step, using $Ac_2O$/HOBt/DIEA solution in NMP. Capping cycle was introduced to prevent deletion byproducts.

At completion of the synthesis, the resin was washed several times with DCM, NMP, isopropanol and methanol, and finally dried.

## 4.4 Mtt/Mmt deprotection and cleavage of the peptides

- Mmt deprotection

The N-ε Mmt protecting group of the Lys9 residue, in both tetradecapeptide and in one of the three decapeptide chains, was removed by repeated treatments (15 min, under gentle agitation) with a solution containing 10% acetic acid and 20% TFE (v/v) in DCM. This procedure was repeated until no yellow colour, indicative of the presence of the (4-methoxyphenyl)diphenylmethyl cation, was detected in the eluent. Subsequently, in order to release the protected peptide from the resin, the resin was treated with 4 resin volumes of a freshly prepared cleavage mixture (1% TFA in DCM, v/v). The acidic mixture was incubated for 2 minutes, under mixing, and the solution was filtered with a vacuum pump, into an ice-cooled flask containing 1/5 acidic mixture volume of a freshly prepared basic solution (10% pyridine in methanol, v/v). The peptides elution was controlled by TLC analysis, by using as eluent the mixture chloroform/methanol 90/10 (v/v); each step was repeated until no product was detected in the collected fractions. The fractions containing the desired product were pooled and then evaporated under reduced pressure up to 5% of the volume. Ice-cold water was added and the mixture was cooled on ice to aid precipitation of the protected peptide. The product was washed several times, with fresh cold water and centrifuged at each step (4 min at 4°C, at 3300 g). Then, it was dried under vacuum to

give the crude peptides.

- Mtt deprotection

In the two remaining decapeptide chains, Mtt protecting group of the Orn9 and Dab9 residues was removed by repeated treatments (1 hour, under gentle agitation) with a solution containing DCM:HFIP:TFE:TES 65:20:10:5 (v/v). Every hour few resin beads were removed from the reaction mixture, and 1-2 drops of TFA were added. The (4-methylphenyl)diphenylmethyl cation produces a yellow color in TFA. Thus, this procedure was followed in order to verify the complete removal of the Mtt protecting group. The resin was then filtered, washed twice with DCM, DMF, 10% DIEA in DMF (v/v), DMF. Subsequently, in order to release the protected decapeptide from the resin, 4 resin volumes of a freshly prepared cleavage mixture (1% TFA, 3% TIS in DCM, v/v) were added. The acidic mixture was incubated for 2 minutes, under mixing, and the solution was filtered with a vacuum pump, into a flask containing 1/5 acidic mixture volumes of a freshly prepared basic solution (10% pyridine in methanol, v/v). The peptides elution was controlled by TLC analysis, by using as eluent the mixture chloroform/methanol 90/10 (v/v); each step was repeated until no product was detected in the collected fractions. The fractions containing the product were pooled and then evaporated under reduced pressure up to 5% of the volume. The protected peptide was extracted in chloroform/water three times, then the organic phase was anhydrified and dried under vacuum. The removal of Mtt-

TIS adduct was obtained by washing the product with fresh diethyl ether and centrifuging at each step (4 min at 4°C, at 3300 g). Therefore, it was dried under vacuum to give the crude C-terminal peptide amides. Orthogonal side chain protecting groups were found to be stable in conditions of Mmt and Mtt deprotection reaction and peptide cleavage reaction.

The peptide homogeneity and identity were assessed by analytical RP-HPLC and by ESI mass spectrometry. A Vydac C18 column (4.6 mm·150 mm; 5 μm), was used in the LC-MS analysis, eluted with $H_2O$/0.1% TFA (v/v) (solvent A) and acetonitrile/0.1% TFA (v/v) (solvent B) linear gradient, from 50% to 90% B over 40 min, at 0.5 mL·min$^{-1}$ flow rate.

Decapeptides and tetradecapeptide chromatograms and the relative mass spectra are reported in Figure 74-77. This first step of the work-up allowed to obtain peptides with ≥ 90% purity level and with ≥ 80% yield.

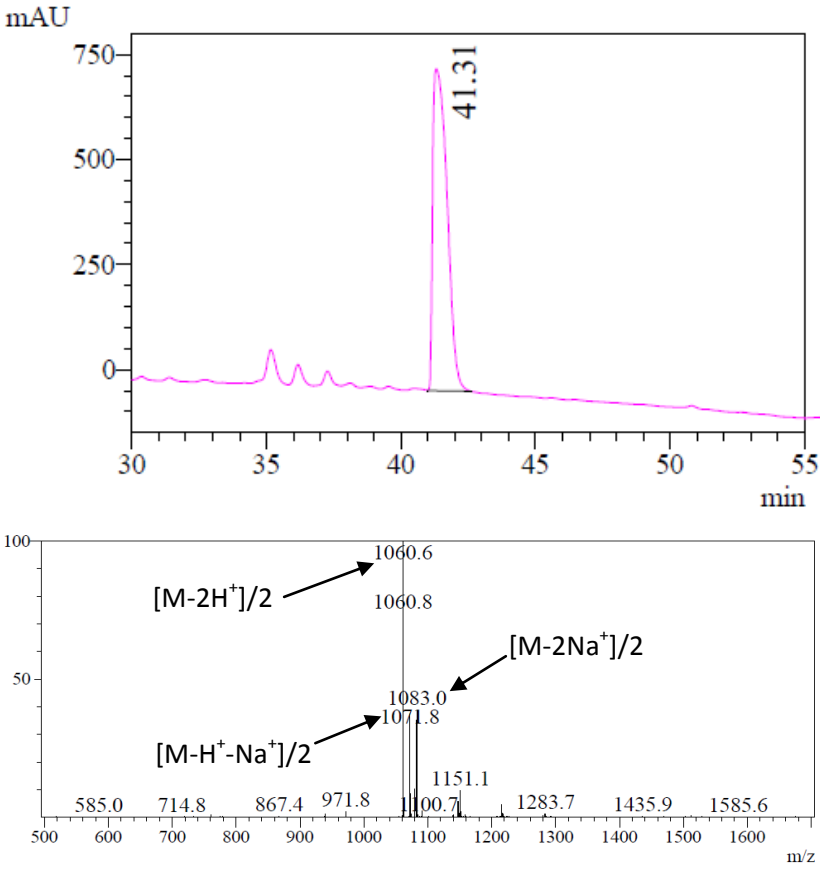


**Figure 74** RP-HPLC chromatogram of protected Mimochrome VI*a* decapeptide, Lys9 deprotected; ESI-MS spectrum of the peak at $R_t$= 41.31 min. One main chromatographic peak (λ = 210 nm) was detected and mass spectrum was in agreement with the expected mass (calculated mass: 2119.53 Da; experimental mass: 2119.4 ± 0.5 Da).

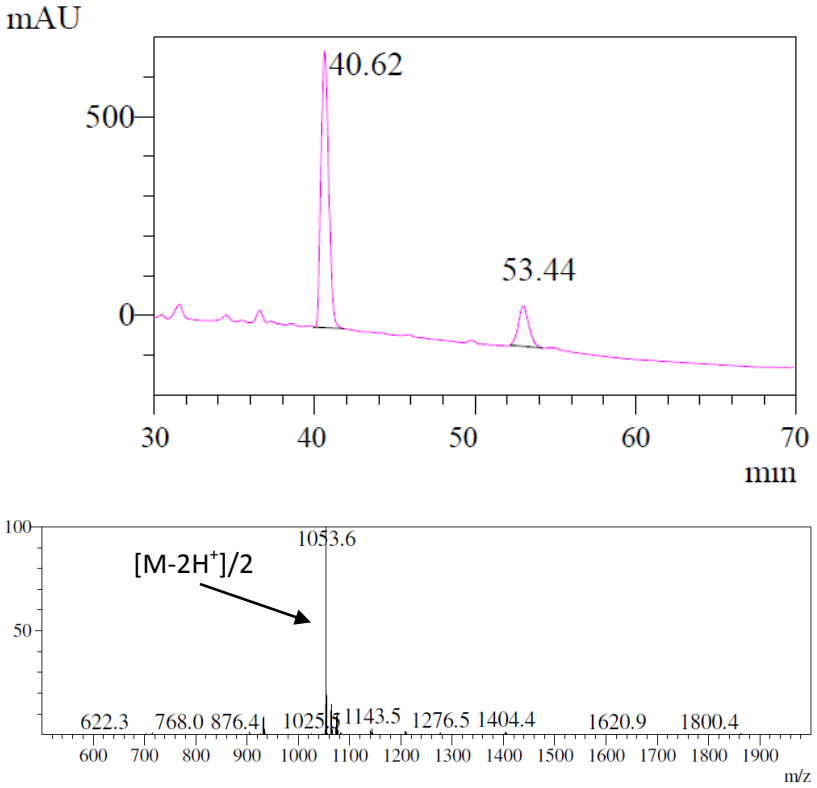


**Figure 75** RP-HPLC chromatogram of protected Mimochrome VI*a* Lys9Orn decapeptide, Orn9 deprotected; ESI-MS spectrum of the peak at $R_t$= 40.62 min. One main chromatographic peak (λ = 210 nm) was detected and mass spectrum was in agreement with expected mass (calculated mass: 2105.50 Da; experimental mass: 2105.2 ± 0.5 Da). MS analysis allowed to identify the minor peak ($R_t$= 53.44 min), as the fully protected peptide.

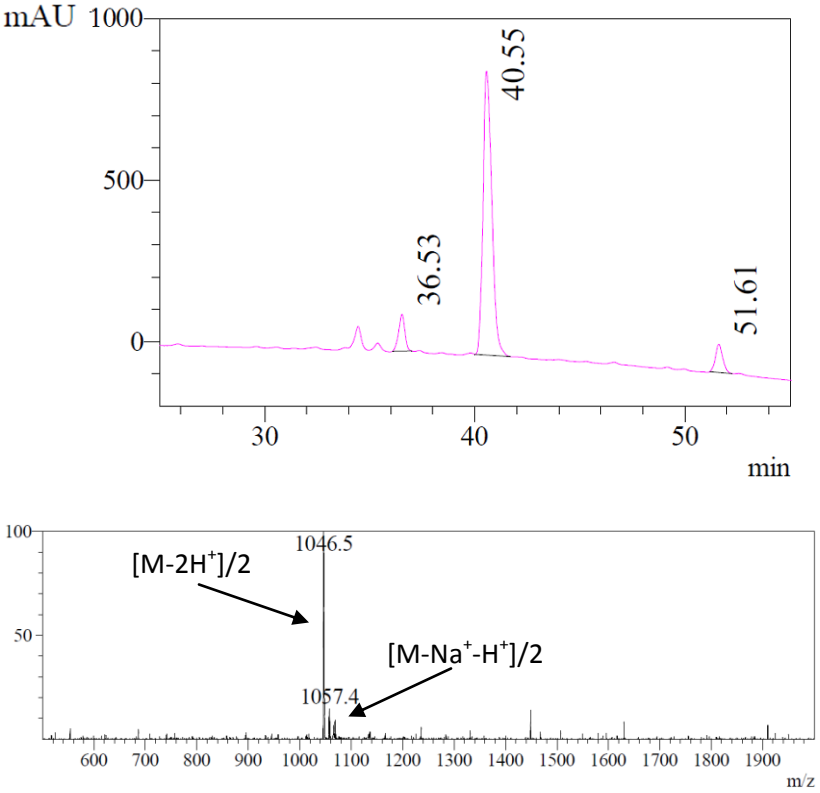


**Figure 76** RP-HPLC chromatogram of protected Mimochrome VI*a* Lys9Dab decapeptide, Dab9 deprotected; ESI-MS spectrum of the peak at $R_t$= 40.55 min. One main chromatographic peak (λ = 210 nm) was detected and mass spectrum was in agreement with the expected mass (calculated mass: 2091.48 Da; experimental mass: 2091.0 ± 0.5 Da). MS analysis allowed also to identify the minor peaks. At $R_t$= 36.53 min elutes the protected peptide, deprotected of Mtt group and lacking a Trt protecting group, maybe lost in the acidic elution conditions; the peak at $R_t$= 51.61 min corresponds to the fully protected peptide.

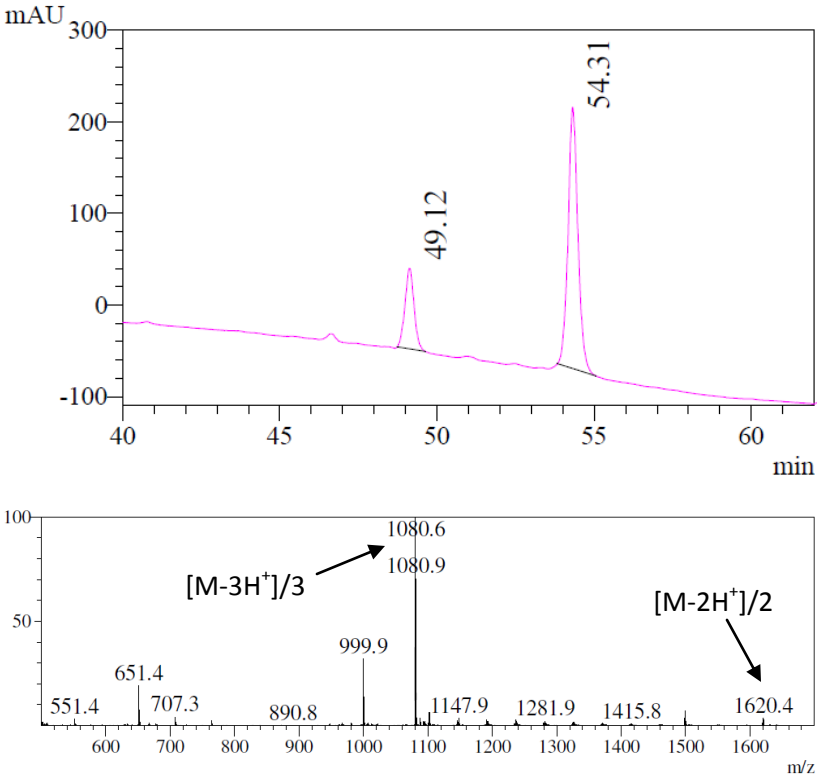


**Figure 77** RP-HPLC chromatogram of Mimochrome VI*a* protected tetradecapeptide, Lys9 deprotected; ESI-MS spectrum of the peak at $R_t$= 54.31 min. One main chromatographic peak (λ = 210 nm) was detected and mass spectrum was in agreement with the expected mass (calculated mass: 3239.12 Da; experimental mass: 3238.8 ± 0.5 Da). MS analysis allowed also to identify the minor peak. At $R_t$= 49.12 min elutes the protected peptide, deprotected of Mmt group, and lacking a Trt protecting group maybe lost in the acidic elution conditions.

## 4.5 Coupling of the decapeptide chains to the deuteroporphyrin

After Mmt/Mtt deprotection, the decapeptide chains (*D*) were coupled to the deuteroporphyrin IX (DPIX). This reaction was performed in DMF, in presence of DIEA (7 eq.), HATU (1 eq.) and deuteroporphyrin IX*2HCl (1.5 eq.) at peptide final concentration of 0.01 M. In order to avoid the formation of the undesired bi-substituted porphyrin (*D*-DPIX-*D*), this reaction was conducted by adding drop wise the peptide to the deuteroporphyrin (30 adds every 2 minutes). The reaction mixture was stirred for 2 h at room temperature, and the pH was assayed every 20 min, and adjusted with DIEA (pH ≈ 8.0), if necessary. The reaction was monitored by analytical HPLC and by TLC (eluent: chloroform/methanol 90:10, $R_f$ = 0.49). A Vydac C8 column (4.6 mm·150 mm; 5 μm), was used in the HPLC analysis, eluted with $H_2O$/0.1% TFA (v/v) (solvent A) and acetonitrile/0.1% TFA (v/v) (solvent B) linear gradient, from 50% to 90% B over 20 min, at 1.0 mL·min$^{-1}$ flow rate.
Two equally abundant peaks (1:1 ratio) were detected. Both peaks show the molecular mass expected for the desired mono-substituted Mimochrome VI*a* (*D*-DPIX). The analytical chromatograms reported in Figure 78-80, were recorded at λ = 210 nm (in magenta) and at λ = 400 nm (in blue). The peak eluted around 30 min corresponds to the undesired bi-substituted porphyrin (*D*-DPIX-*D*). The yield of this reaction, evaluated on the basis of the chromatographic peaks areas, was ≈ 80 %.

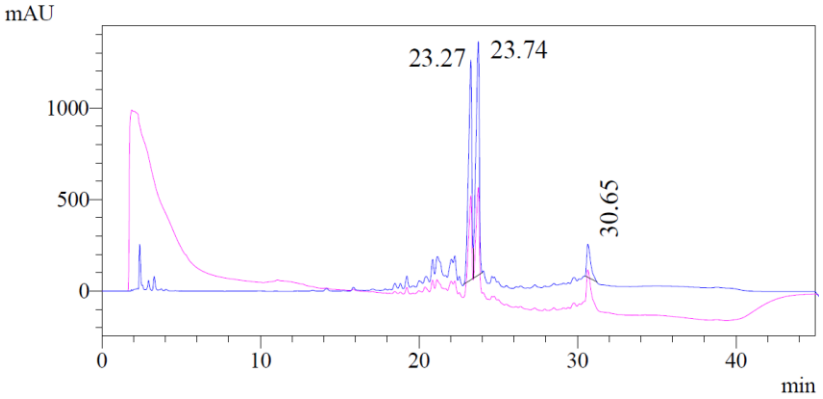


**Figure 78** RP-HPLC chromatogram at the end of the coupling reaction of **Mimochrome VI*a* mono-substituted derivative**. The main chromatographic peaks (λ = 400 nm) correspond to the desired products (*D*-DPIX, two constitutional isomers). The minor peak ($R_t$= 30.65 min) corresponds to the undesired bi-substituted porphyrin (*D*-DPIX-*D*), whereas the excess of DPIX is eluted in the void volume.

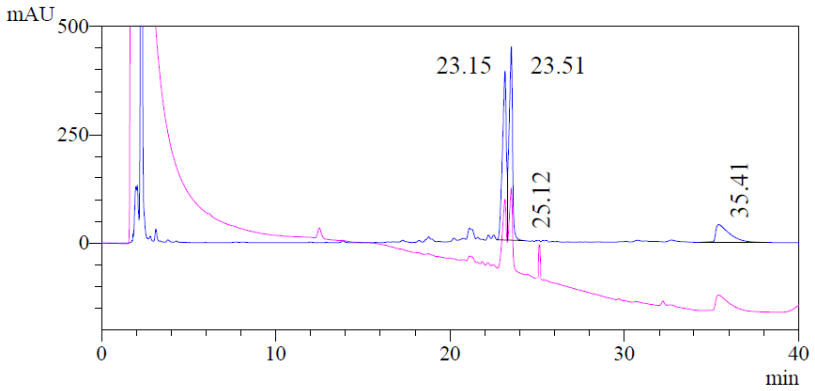


**Figure 79** RP-HPLC chromatogram at the end of the coupling reaction of **Lys9Orn(*D*)-Mimochrome VI*a* mono-substituted derivative**. The main chromatographic peaks (λ = 400 nm) correspond to the desired products (Lys9Orn(*D*)-DPIX, two constitutional isomers). The minor peaks correspond to: the undesired bi-substituted porphyrin (Lys9Orn(*D*)-DPIX-Lys9Orn(*D*)), at $R_t$= 35.41 min, and the fully protected Lys9Orn decapeptide, at $R_t$= 25.12 min. The excess of DPIX is eluted in the void volume.

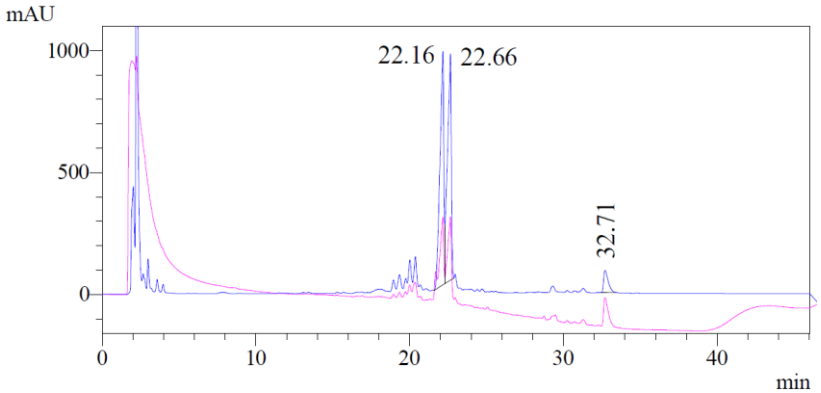


**Figure 80** RP-HPLC chromatogram at the end of the coupling reaction of **Lys9Dab(*D*)-Mimochrome VI*a* mono-substituted derivative**. The main chromatographic peaks (λ = 400 nm) correspond to the desired products (Lys9Dab(*D*)-DPIX, two constitutional isomers). The minor peak, at $R_t$= 32.71 min, corresponds to the undesired bi-substituted porphyrin (Lys9Dab(*D*)-DPIX-Lys9Dab(*D*)), whereas the excess of DPIX is eluted in the void volume.

The reaction mixture was evaporated under reduced pressure and dried. The crude products were purified by Flash Chromatography, on a SNAP HP 100 g silica column, using a chloroform/methanol gradient from 7 to 12% methanol over 6 column volumes, at 50 mL·min$^{-1}$ flow rate. The products were eluted at 9% methanol, and obtained in a 83% yield. This purification allowed to remove all the excess of deuteroporphyrin IX, the undesired bi-substituted porphyrin (*D*-DPIX-*D*), and, if present, the fully protected decapeptide.

## 4.6 Synthesis of Mimochrome VI*a* and its analogues apo forms

The purified monopeptide *D*-DPIX derivative were used for the synthesis of the bi-substituted molecules. Each coupling reaction was conducted on the monopeptide derivative (1 eq.), in the presence of DIEA (6 eq.), HATU (1.2 eq.), and tetradecapeptide (1.1 eq.). The reaction mixture ($8.5 \cdot 10^{-3}$ M in DMF) was incubated at room temperature for 2 h. The pH was checked during the reaction time and adjusted to ≈ 8, if necessary. The reaction progress was followed by TLC (eluent: chloroform/methanol 90:10, $R_f$ = 0.65). At the end, the reaction mixture was evaporated under reduced pressure. The protected bi-substituted compounds were dissolved in chloroform and extracted with water three times. The organic phase was anhydrified with $Na_2SO_4$, evaporated under reduced pressure and dried.

Finally, fully deprotected molecule was obtained by addition of the cleavage mixture (94% TFA, 2.5% EDT, 1% TIS, 2.5% $H_2O$, v/v). The reaction was conducted under stirring, at 0°C for 1h and at room temperature for the second hour. The reaction mixture was concentrated on a rotary evaporator, the crude product precipitated by adding cold diethyl ether. The mixture was centrifuged (room temperature, at 3300 g), the supernatant was removed and the precipitate was washed twice with three volumes of cold diethyl ether. The crude product was dried, and then re-dissolved in water/0.1% TFA (v/v) and

analyzed by LC-MS. A Vydac C18 column (4.6 mm·150 mm; 5 µm), was used in the LC-MS analyses, eluted with $H_2O$/0.1% TFA (v/v) (solvent A) and acetonitrile/0.1% TFA (v/v) (solvent B) linear gradient, from 10% to 50% B over 60 min, at 0.5 mL·min$^{-1}$ flow rate.

As already observed for the mono-substituted Mimochrome VI*a* derivatives, two peaks are present. They show the same mass spectra, corresponding to the desired Mimochrome VI*a* analogue. The analytical chromatogram and the mass spectrum of Lys9Dab(*D*)-Mimochrome VI*a* are reported in Figure 81-83, as an example.

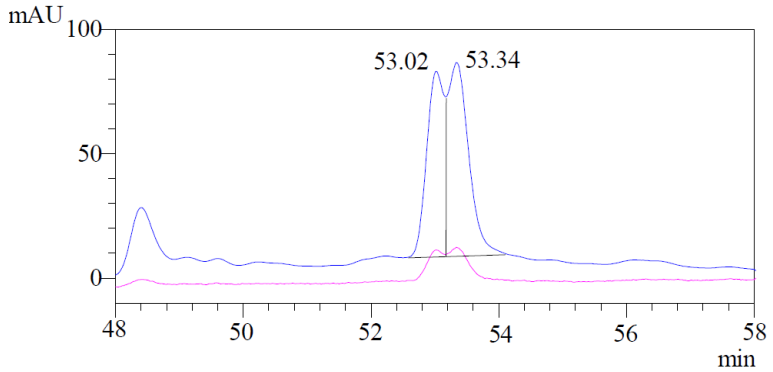


**Figure 81** RP-HPLC chromatogram of Lys9Dab(*D*)-Mimochrome VI*a* apo form.

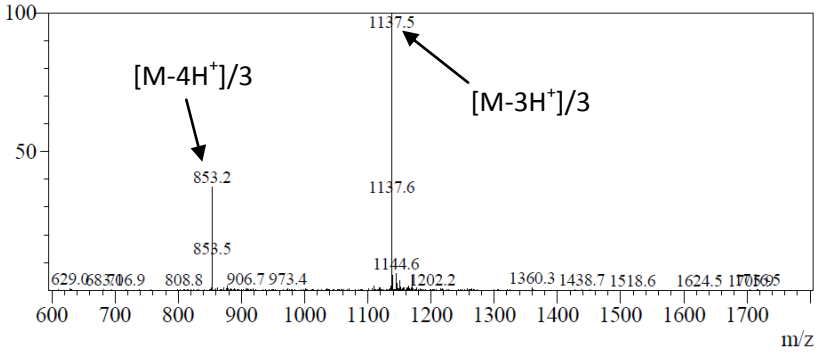


**Figure 82** ESI-MS spectrum of the peak at $R_t$= 53.02 min (calculated mass: 3409.78 Da; experimental mass: 3409.1 ± 0.8 Da).

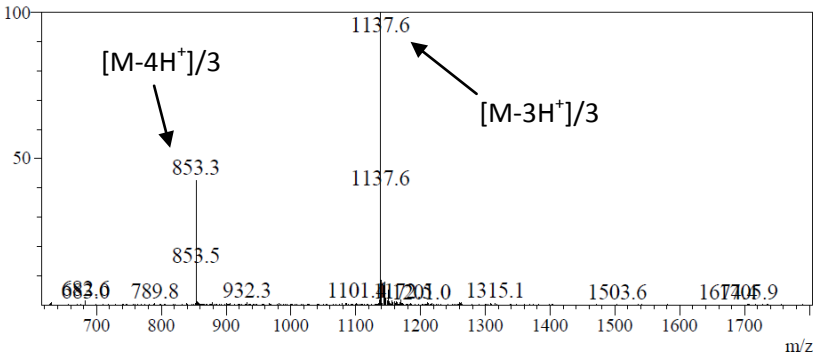


**Figure 83** ESI-MS spectrum of the peak at $R_t$= 53.34 min (calculated mass: 3409.78 Da; experimental mass: 3409.5 ± 0.4 Da).

The crude material was then purified by preparative RP-HPLC. A Vydac C18 column (50 mm·250 mm; 10 µm) was used, eluted with $H_2O$/0.1% TFA (v/v) (solvent A) and acetonitrile/0.1% TFA (v/v) (solvent B) linear gradient, from 10% to 50% B over 50.1 min, at 100.0 mL·min$^{-1}$ flow rate. This purification allowed to separate the two compounds for each apo form.

The pooled fractions containing the desired products were lyophilized.

## 4.7 Iron insertion

Iron ion was inserted, according to the acetate method procedure, slightly modified by us.[4,5] Iron (II) acetate (10 eq.) was added to a solution of pure Mimochrome VI analogue apo form ($2.0 \cdot 10^{-4}$ M), in 2/3 TFE/AcOH (v/v), and the reaction mixture was kept at 50 °C for 2 h, refluxing under nitrogen. The reaction was monitored by analytical HPLC, using a Vydac C18 column, eluted with $H_2O$/0.1% TFA (v/v) (solvent A) and acetonitrile/0.1% TFA (v/v) (solvent B) linear gradient, from 10% to 50% B over 30 min, at 1.0 $mL \cdot min^{-1}$ flow rate. Once the reaction was completed, the solvent was removed under vacuum, and the products were purified, in order to remove the excess of iron acetate, by Reverse Phase-Flash Chromatography, on a SNAP KP-C18-HS 30 g column, using a gradient of acetonitrile in 0.1% aqueous TFA, 5% to 95% over 2 column volumes, at 25 $mL \cdot min^{-1}$ flow rate. After lyophilisation, pure products were obtained as TFA salts. LC-MS analysis of all the synthesized compounds, confirmed their high purity (>95%) and the expected molecular weight (Figure 84-89). The analytical chromatograms were recorded at $\lambda$ = 210 nm (in magenta) and at $\lambda$ = 387 nm (in brown). A Vydac C18 column was used in the LC-MS analysis, eluted with $H_2O$/0.1% TFA (v/v) (solvent A) and acetonitrile/ 0.1% TFA (v/v) (solvent B) linear gradient, from 10% to 50% B over 60 min, at 0.5 $mL \cdot min^{-1}$ flow rate.

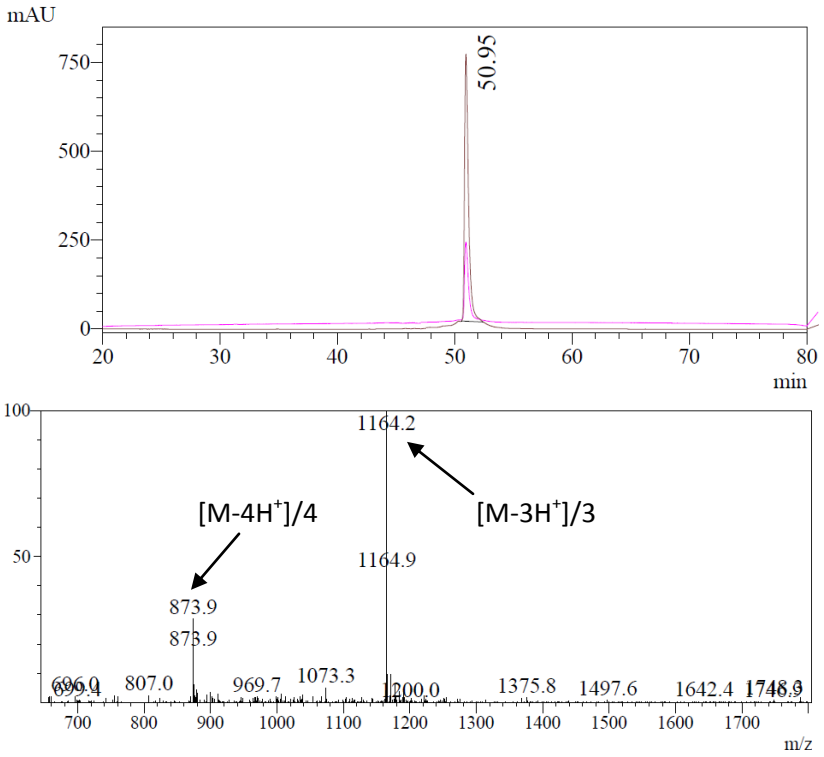


**Figure 84** RP-HPLC chromatogram and ESI-MS spectrum of pure $Fe^{III}$-2Aib1Lys-MimoVI isomer 1. One chromatographic peak was detected and mass spectrum was in agreement with the expected mass (calculated mass: 3491.66 Da; experimental mass: 3490.6 ± 1.2 Da).

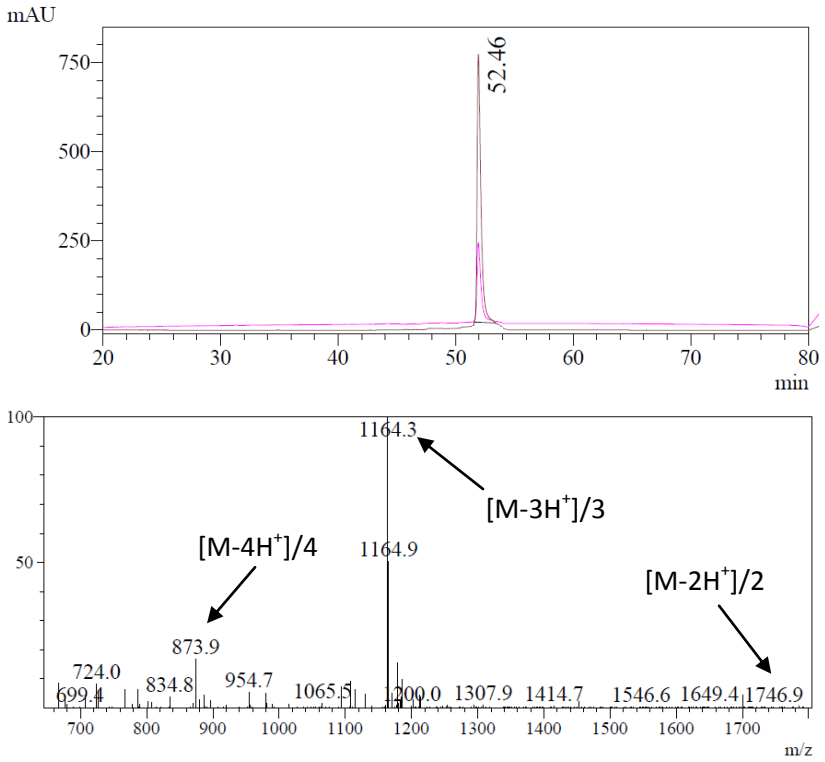


**Figure 85** RP-HPLC chromatogram and ESI-MS spectrum of pure $Fe^{III}$-2Aib1Lys-MimoVI isomer 2. One chromatographic peak was detected and mass spectrum was in agreement with the expected mass (calculated mass: 3491.66 Da; experimental mass: 3491.1 ± 1.0 Da).

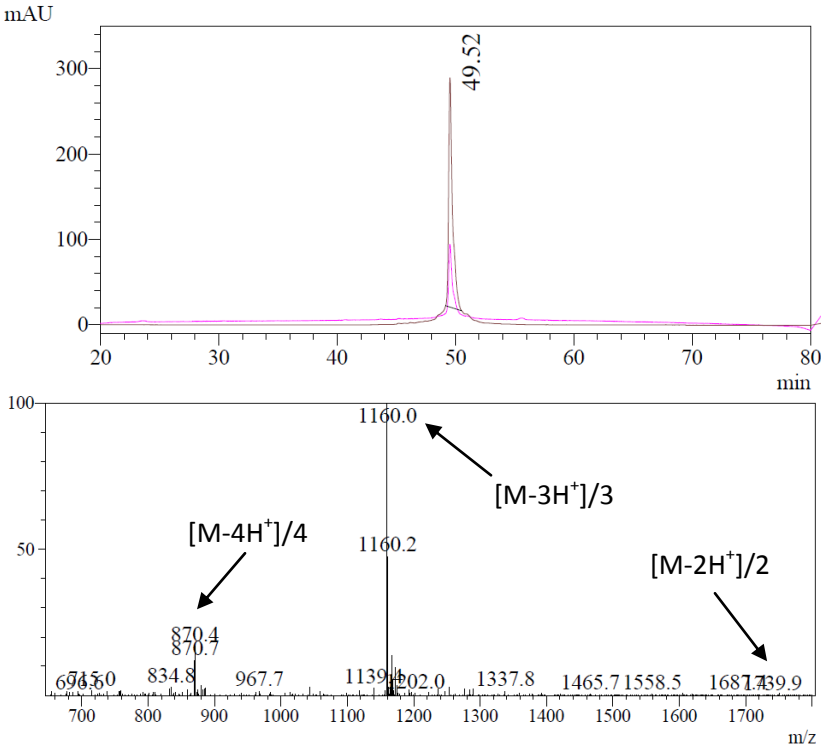


**Figure 86** RP-HPLC chromatogram and ESI-MS spectrum of pure $Fe^{III}$-2Aib1Orn-MimoVI isomer 1. One chromatographic peak was detected and mass spectrum was in agreement with the expected mass (calculated mass: 3477.63 Da; experimental mass: 3477.4 ± 0.4 Da).

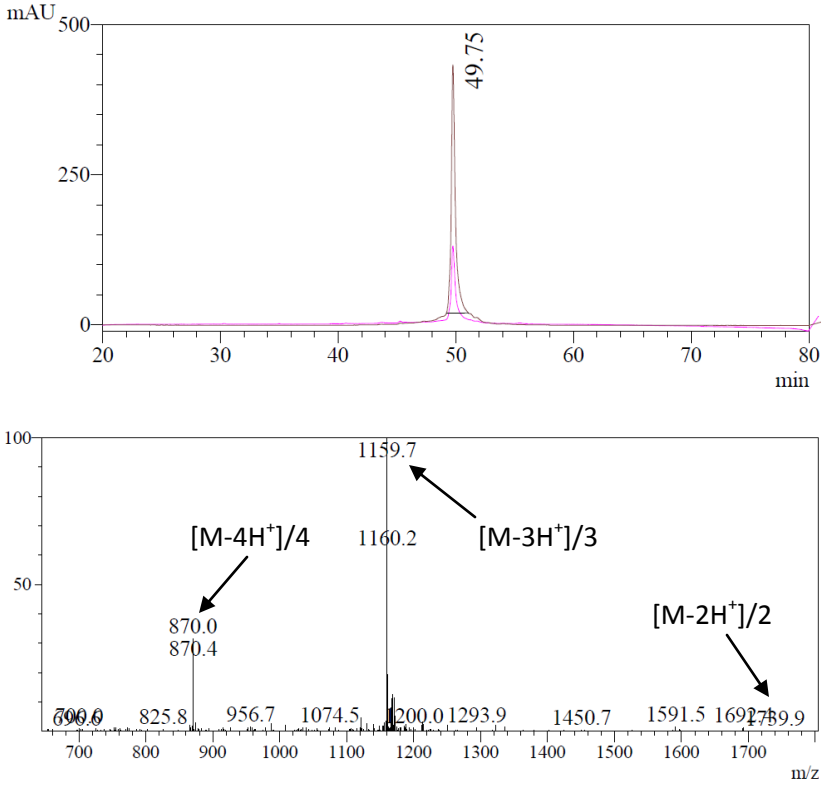


**Figure 87** RP-HPLC chromatogram and ESI-MS spectrum of pure $Fe^{III}$-2Aib1Orn-MimoVI isomer 2. One chromatographic peak was detected and mass spectrum was in agreement with the expected mass (calculated mass: 3477.63 Da; experimental mass: 3477.0 ± 0.8 Da).

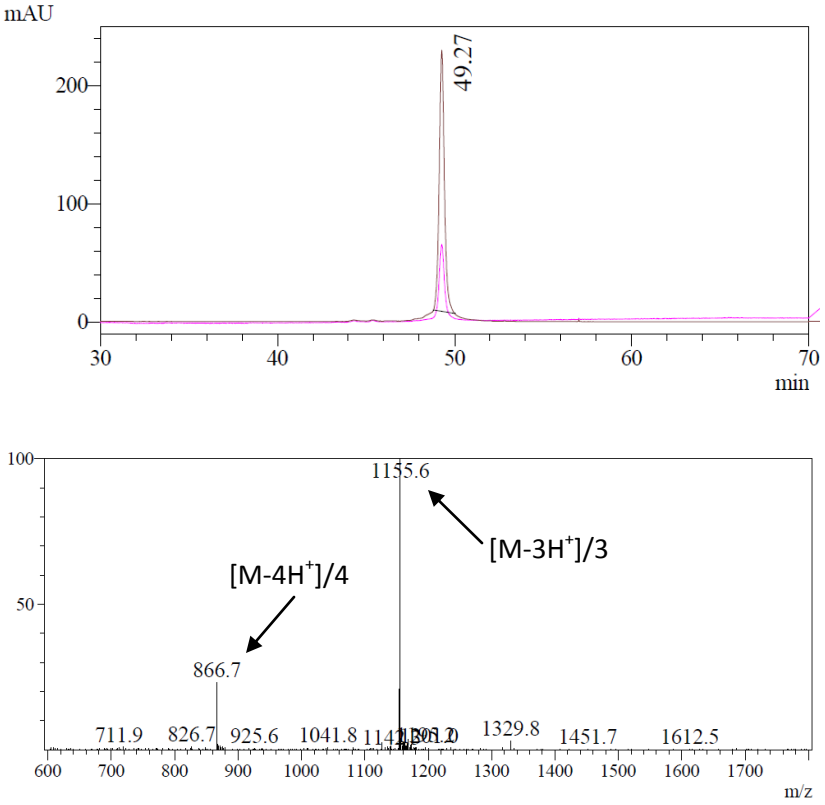


**Figure 88** RP-HPLC chromatogram and ESI-MS spectrum of pure $Fe^{III}$-2Aib1Dab-MimoVI isomer 1. One chromatographic peak was detected and mass spectrum was in agreement with the expected mass (calculated mass: 3463.61 Da; experimental mass: 3463.3 ± 0.7 Da).

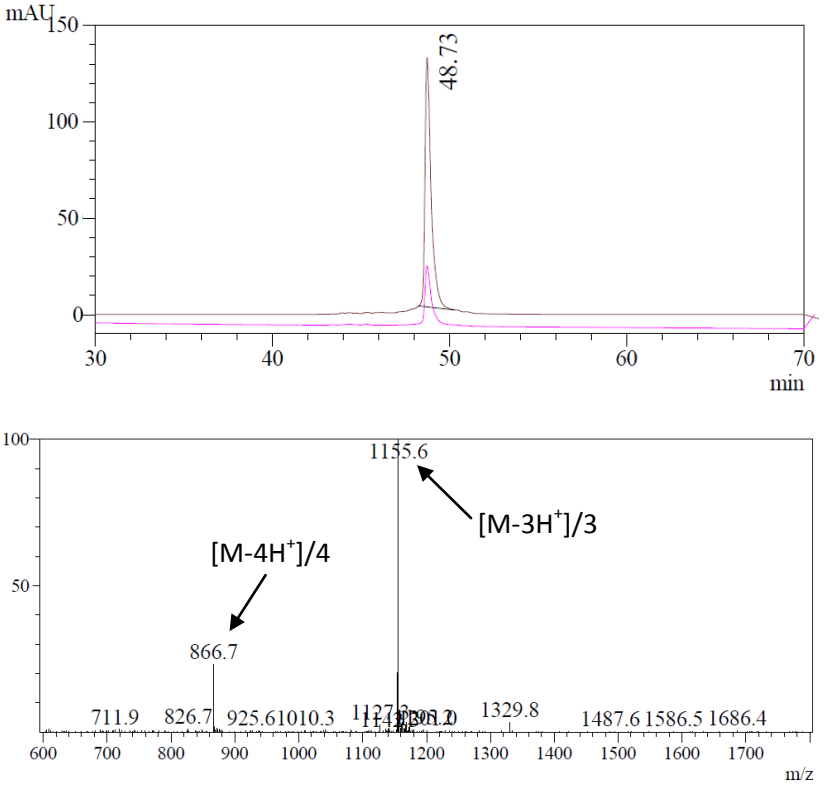


**Figure 89** RP-HPLC chromatogram and ESI-MS spectrum of pure $Fe^{III}$-2Aib1Dab-MimoVI isomer 2. One chromatographic peak was detected and mass spectrum was in agreement with the expected mass (calculated mass: 3463.61 Da; experimental mass: 3463.3 ± 0.7 Da).

## 4.8 Cobalt insertion

Cobalt ion (II) was inserted into 2Aib1Dab-MimoVI isomer 2 apo form, according to literature procedure.[4] Co(II) acetate (10 eq.) was added to a solution of pure apo form ($2.0 \cdot 10^{-4}$ M), in 2/3 TFE/AcOH (v/v), and the reaction mixture was kept at 50 °C for 2 h, under reflux. The reaction was monitored by analytical HPLC. A Vydac C18 column (4.6 mm·150 mm; 5 μm), was used, eluted with $H_2O$/0.1% TFA (v/v) (solvent A) and acetonitrile/0.1% TFA (v/v) (solvent B) linear gradient, from 10% to 50% B over 30 min, at 1.0 $mL \cdot min^{-1}$ flow rate. Two species were found in about the same ratio, named 2a and 2b (see Figure 65, Chapter II: Results and discussion). Once the reaction was completed, the solvent was removed under vacuum, and the products were purified, in order to remove the excess of cobalt (II) acetate, by Reverse Phase-Flash Chromatography, on a SNAP KP-C18-HS 30 g column, eluted with $H_2O$/0.1% TFA (v/v) (solvent A) and acetonitrile/0.1% TFA (v/v) (solvent B) linear gradient, from 5% to 95% B over 2 column volumes, at 25 $mL \cdot min^{-1}$ flow rate. The solvent was then removed under vacuum, and the two species were purified to homogeneity by preparative RP-HPLC. A Vydac C18 column (22 mm·250 mm; 10 μm) was used, eluted with $H_2O$/0.1% TFA (v/v) (solvent A) and acetonitrile/0.1% TFA (v/v) (solvent B) linear gradient, from 10% to 80% B over 58.5 min, at 21 $mL \cdot min^{-1}$ flow rate. Pure products were obtained as the TFA salt. Reverse phase analytical HPLC coupled with ESI-

MS confirmed the expected molecular weight (see Figure 66 and 67, Chapter II: Results and discussion).

References

(1) Schrödinger, L. L. C. The PyMOL Molecular Graphics System, Version 1.3r1, 2010.
(2) Humphrey, W.; Dalke, A.; Schulten, K. *J. Mol. Graph.* **1996**, *14* (1), 33–38, 27–28.
(3) Faiella, M.; Maglio, O.; Nastri, F.; Lombardi, A.; Lista, L.; Hagen, W. R.; Pavone, V. *Chem.- Eur. J.* **2012**, *18* (50), 15960–15971.
(4) Buchler, J.W.,. In *The Porphyrins, Volume 1*; David Dolphin, Series Ed.; NY, USA, 1979; Vol. I, pp 389–483.
(5) Nastri, F.; Lombardi, A.; Morelli, G.; Maglio, O.; D'Auria, G.; Pedone, C.; Pavone, V. *Chem. - Eur. J.* **1997**, *3* (3), 340–349.

## List of acronyms and abbreviations

ABTS: 2,2'-azino-bis(3-ethylbenzthiazoline-6-sulphonic acid)
Abs: Absorbance
Ac: Acetyl
Aib: 2-amino-2-methylpropanoic acid
Arg: Arginine
Asn: Asparagine
Asp: Aspartic acid
Boc: t-Butoxycarbonyl
CD: Circular dichroism
Cys: Cysteine
Dab: 2,4-Diaminobutyric acid
DCM: Dichloromethane
DIEA: Ethyldiisopropylamine
DMF: *N,N*-Dimethylformamide
DPIX: Deuteroporphyrin IX
EDT: 1,2-Ethanedithiol
EPR: Electron paramagnetic resonance
Eq.: equivalent
ESI-MS: Electrospray ionization mass spectrometry
Fmoc: 9-Fluorenylmethoxycarbonyl
Gln: Glutamine
Glu: Glutamic acid
HATU: *N*-[(Dimethylamino)-1*H*-1,2,3-triazolo-[4,5-*b*] pyridin- 1-ylmethylene]-*N*-methylmethanaminium hexafluorophosphate *N*-oxide
HFIP: 1,1,1,3,3,3-Hexafluoro-2-propanol
His: Histidine

HOBt: N-hydroxybenzotriazole
HRP: Horseradish peroxidase
HS: High spin
Ile: Isoleucine
IUPAC: International Union of Pure and Applied Chemistry
Leu: Leucine
Lys: Lysine
MCD: Magnetic circular dichroism
Met: Methionine
Mmt: (4-methoxyphenyl)diphenylmethyl
Mtt: (4-methylphenyl)diphenylmethyl
NMP: N-Methyl-2-pyrrolidone
NMR: Nuclear magnetic resonance
Orn: 2,5-Diaminopentanoic acid
Pbf: 2,2,4,6,7-Pentamethyldihydrobenzofuran-5-sulfonyl
PDB: Protein Data Bank
Pro: Proline
PyBop: (Benzotriazol-1-yloxy)tripyrrolidinophosphonium hexafluorophosphate
QS: Quantum-mechanical admixed spin
$R_f$: Retention factor
$R_t$: Retention time
RMD: Restrained molecular dynamics
RP-HPLC: Reverse Phase - High Performance Liquid Chromatography
Ser: Serine
T.O.N.: Turnover number
tBu: tert-butyl
TES: Triethylsilane
TFA: Trifluoroacetic acid

TFE: 2,2,2-trifluoroethanol
Thr: Threonine
TIS: Triisopropylsilane
TLC: Thin Layer Chromatography
Trt: Trityl
Tyr: Tyrosine

## List of publications, communications and awards

Vitale, R.; Lista, L.; **Cerrone, C.;** Caserta, G.; Chino, M.; Maglio, O.; Nastri, F.; Pavone, V.; Lombardi, A..

*Organic & Biomolecular Chemistry* (2015).
DOI:10.1039/c5ob00257e

**Title.** *An artificial heme-enzyme with enhanced catalytic activity: evolution, functional screening and structural characterization.*

**Abstract.** Synthetic proteins represent useful tools for reproducing metalloprotein functions in minimal, well-defined scaffolds. Herein, we describe the rational refinement of function into heme-protein models from the Mimochrome family. Originally designed to mimic the bis-His cytochrome b, the Mimochrome structure was modified to introduce a peroxidase-like activity, by creating a distal cavity on the heme. The success with the first asymmetric system, Mimochrome VI (MC6), gave the opportunity to explore further modifications in order to improve the catalytic activity. Starting from ferric MC6, single amino acid substitutions were introduced in the peptide chains to obtain four compounds, which were screened for peroxidase activity. The detailed structural and functional analysis of the best analogue, $Fe^{III}$-$E^2$L(TD)-MC6, indicates that an arginine residue in proximity to the heme-distal site could assist with catalysis by favoring the formation of the intermediate "compound I", thus mimicking $R^{38}$ in HRP. This result highlights the potential of using small scaffolds for exploring the main factors that tune the heme-protein activity, and for programming new desired functions.

***

The functionalization to antibodies of the compounds herein described, in order to develop diagnostic devices was proposed in "InKidia" business idea and received one of the first two Tech Hub 2015 prizes, for the foundation of new Start Up Companies.

***

Caserta, G.; **Cerrone, C.**; Vicari, C.; Lista, L.; Maglio, O.; Nastri, F.; Pavone, V.; Lombardi, A..

XLI Congresso Nazionale della Divisione di Chimica Inorganica della Società Chimica Italiana. Parma, 3-6 September 2013, p. P16 (Poster Presentation)

**Title.** *A new Cobalt-Porphyrin mimetic: $Co^{III}$-Mimochrome VI-2U1L.*

**Abstract.** Metal ions enclosed in a rigid macrocycle ring and axially coordinated by a single nitrogen donor ligand are widespread in biological systems as protein cofactors. Numerous models were developed to unravel the delicate interplay between structure and function in metalloproteins and to construct new synthetic functional molecules.[1] Although there are a number of Co-containing enzymes, the biological chemistry of cobalt is dominated by the chemistry of cobalamins. Several examples of water-soluble peptide-based cobalt-porphyrin have been reported; they are often characterized by a bis-His coordination but only few NMR structures were reported.[2]
The *Artificial Metallo-Enzyme Group* developed a class of synthetic heme-protein models: Mimochromes. They are porphyrin-peptide conjugates, made up by two peptides, covalently linked to the deuteroporphyrin IX. The two peptides are in α-helical conformation and cover both planes of the heme, resulting in a helix-heme-helix sandwich.[3]

The first pentacoordinated model among the Mimochrome family, Mimochrome VI, exhibits peroxidase-like activity in its iron form.[4] Despite the catalytic performance, this molecule showed conformational flexibility, which limited a complete structural characterization.
With the aim of enhancing the structural and functional properties, new analogues were designed, in which Aib residues were inserted at different positions of the peptide chains.
Mimochrome VI-*2U1L* is the result of a refinement procedure, which involved several cycles of molecular design, characterization and redesign. This molecule exhibits a better peroxidase catalytic performance in its ferric form than the parent molecule. In order to better understand the structure-function relationship we developed the fully diamagnetic compound, $Co^{III}$-Mimochrome VI-*2U1L*.
The UV-Vis and CD characterization together with the analysis of the NMR structure will be presented.


(1) Reedy, C. J.; Gibney, B. R. *Chem. Rev.* **2004**, *104* (2), 617–650.
(2) Yonetani, T.; Yamamoto, H.; Woodrow, G. V. *J. Biol. Chem.* **1974**, *249* (3), 682–690.
(3) Lombardi, A.; Nastri, F.; Pavone, V. *Chem. Rev.* **2001**, *101* (10), 3165–3189.
(4) Nastri, F.; Lista, L.; Ringhieri, P.; Vitale, R.; Faiella, M.; Andreozzi, C.; Travascio, P.; Maglio, O.; Lombardi, A.; Pavone, V. *Chem. - Eur. J.* **2011**, *17* (16), 4444–4453.


***


**Cerrone, C.**; Caserta, G.; Vitale, R.; Nastri, F.; Maglio, O.; Pavone, V.; Lombardi, A..

XLI Congresso Nazionale della Divisione di Chimica Inorganica della Società Chimica Italiana. Parma, 3-6 September 2013, p. OC41 (Oral Presentation)


**Title.** *Developing New Artificial Heme-Enzymes for Catalytic Applications.*

**Abstract.** The Horseradish Peroxidase (HRP) is the most representative peroxidase. It is a glycosylated hemeprotein able to catalyze the oxidation of a wide range of organic compounds using $H_2O_2$ as oxidant.[1]
In order to mimic HRP, new synthetic models were developed: Mimochromes.
The main features of Mimochromes are the covalent structure and a well-defined helical conformation of the peptide chains linked to the deuteroporphyrin ring, even in the absence of metal ion coordination; the two peptide chains cover both planes of the heme, resulting in a helix-heme-helix sandwich. A minimalist approach was used to design short peptide sequences which could serve partly the same functions of the protein chain in the natural heme-proteins.[2]
$Fe^{III}$-Mimochrome VI is a pentacoordinated model that catalyzes the oxidation of several substrates by the activation of $H_2O_2$.[3] The structure of $Fe^{III}$-Mimochrome VI was not resolved because of its conformational flexibility. Therefore, new analogues containing amino acidic substitutions in key positions of the sequences, were designed, with the aim of stabilizing one conformation and henceforth improving the catalytic properties.
In particular, these substitutions were intended to: a) increase the helical content of the decapeptide chain (introduction of Aib residues), b) decrease the flexibility of the linker between the decapeptide chain and the porphyrin (substitution of $Lys^9$ with Orn) and c) allow an Arg residue to freely participate in the catalytic cycle, mimicking $Arg^{38}$ in HRP (substitution of $Glu^2$ with Leu on the tetradecapeptide, preventing $Arg^{10}$ on the decapeptide from forming ionic interaction).
The resulting molecules were synthesized and characterized by UV-Vis spectroscopy and circular dichroism; furthermore, their peroxidase-like activity was

evaluated toward a reducing substrate, ABTS (2,2'-azino-bis(3-ethylbenzthiazoline-6-sulphonic acid)).

(1) Azevedo, A. M.; Martins, V. C.; Prazeres, D. M. F.; Vojinović, V.; Cabral, J. M. S.; Fonseca, L. P. In *Biotechnology Annual Review*; Elsevier, 2003; Vol. 9, pp 199–247.
(2) Lombardi, A.; Nastri, F.; Pavone, V. *Chem. Rev.* **2001**, *101* (10), 3165–3189.
(3) Nastri, F.; Lista, L.; Ringhieri, P.; Vitale, R.; Faiella, M.; Andreozzi, C.; Travascio, P.; Maglio, O.; Lombardi, A.; Pavone, V. *Chem. - Eur. J.* **2011**, *17* (16), 4444–4453.

***

Lombardi, A.; Vitale, R.; Lista, L.; **Cerrone, C.**; Caserta, G.; Vicari, C.; Maglio, O.; Nastri, F.; Pavone, V..

The Italian Meeting on Porphyrin and Phthalocyanines-1. Roma, 1-3 July 2013 (Oral Presentation)

**Title.** *Heme-protein mimics by design: strategies and applications.*

**Abstract.** Heme-proteins take part in a variety of life-sustaining processes and catalyze difficult reactions with efficiency and selectivity that few other natural or artificial molecules can achieve.[1] For this reason, structural and functional studies on heme-proteins have been the focus of many years of research.
The architecture and composition of the protein matrix for heme have been selected by Nature in order to allow a single prosthetic group to serve numerous and diverse chemical functions, such as dioxygen storage and transport, electron transfer, hydroxylation and oxidation of organic substrates, and hydrogen peroxide disproportion. Variation in shape, volume, and chemical composition of the binding site, in the mode of heme-binding and in the number and nature of hemeprotein interactions, are the main factors which contribute to the functional specificity of the heme.[2]

Understanding at a molecular level the mechanism by which the protein matrix finely tunes the environment of the heme is of fundamental importance in both basic and applied science.

Over the years, a large number of low molecular weight chemical catalysts has been developed as heme-protein mimics.[2] They have been basic in elucidating structure and function of heme-proteins and heme-enzymes; however, they often fail in reproducing several features of biocatalysts, such as high turn-over number under mild conditions and high selectivity.

Combining the advantages of chemical and biological catalysts would represent a daunting goal for chemists. Many efforts have been devoted to the design of peptide-based heme-protein models.[2,3] The design strategy for the development of such systems is very challenging, because it requires two sets of factors to be taken into account simultaneously: *(i)* the construction of an artificial protein that adopts the unique desired folding, and *(ii)* the engineering into the interior of the designed protein of a proper cavity able to accommodate the large hydrophobic heme.

Using a structure-based strategy, we have developed a class of peptide-porphyrin conjugates, named Mimochromes, to investigate the effects of peptide chains composition and folding in modulating the properties of the metal ion into the porphyrin ring.[4,5] The main features of these molecules are the covalent structure and the sandwich motif, with two helical peptides surrounding the heme on both faces. Our recent results on their structural and functional characterization will be presented. Their usefulness in biomedical and environmental applications, as well in biosensor construction, will be particularly highlighted.

(1) Lu, Y. *Angew. Chem. Int. Ed Engl.* **2006**, *45* (34), 5588–5601.
(2) Lombardi, A.; Nastri, F.; Pavone, V. *Chem. Rev.* **2001**, *101* (10), 3165–3189.

(3) Reedy, C. J.; Gibney, B. R. *Chem. Rev.* **2004**, *104* (2), 617–650.
(4) Nastri, F.; Lista, L.; Ringhieri, P.; Vitale, R.; Faiella, M.; Andreozzi, C.; Travascio, P.; Maglio, O.; Lombardi, A.; Pavone, V. *Chem. - Eur. J.* **2011**, *17* (16), 4444–4453.
(5) Faiella, M.; Maglio, O.; Nastri, F.; Lombardi, A.; Lista, L.; Hagen, W. R.; Pavone, V. *Chem.- Eur. J.* **2012**, *18* (50), 15960–15971.

***